KERNFORSCHUNGSANLAGE JÜLICH GmbH
Institut für Festkörperforschung

# Temperature Dependence of the Anisotropy of the Threshold Energy for Defect Production in Platinum

by

N. Afify

Jül - Spez - 38
Mai 1979
ISSN 0343-7639

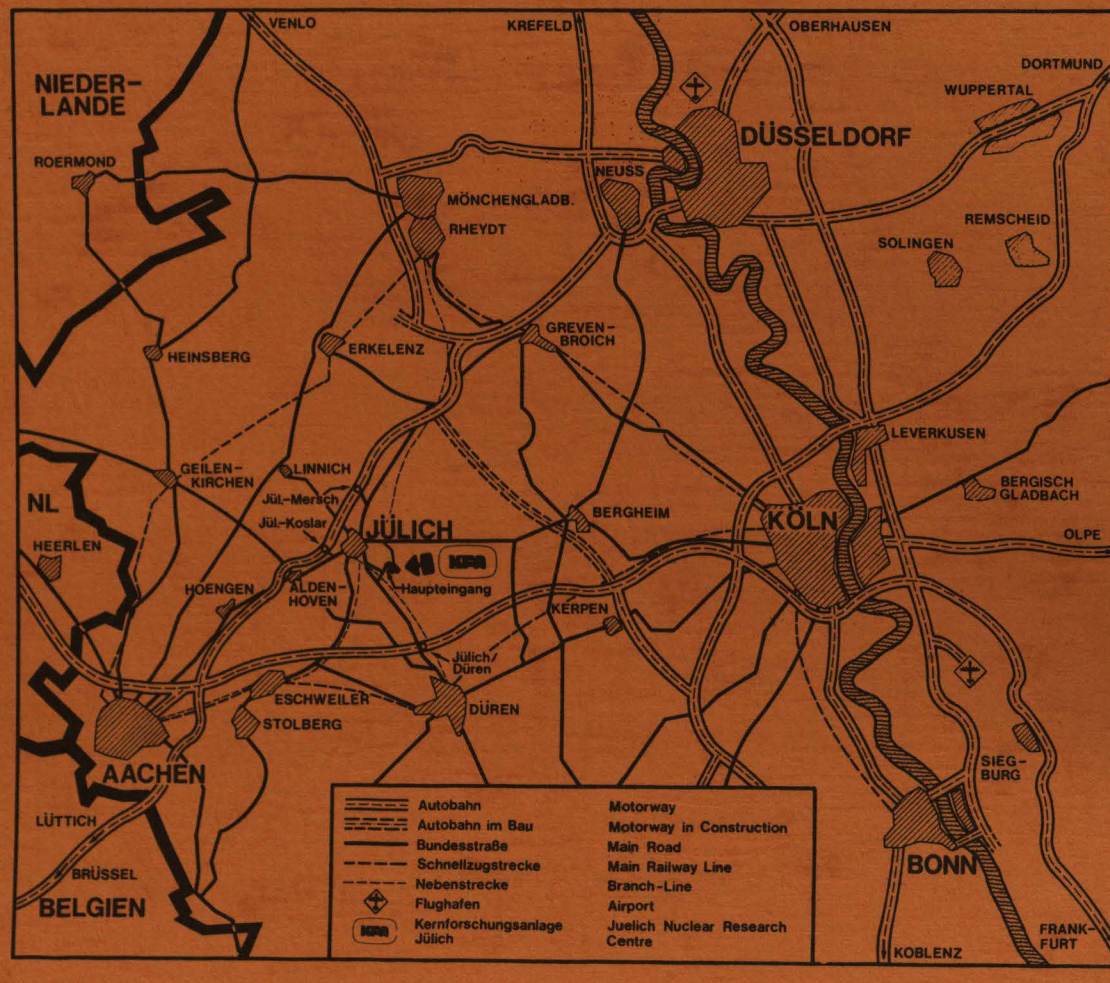


Als Manuskript gedruckt

**Spezielle Berichte der Kernforschungsanlage Jülich – Nr. 38**

Institut für Festkörperforschung Jül - Spez - 38

Zu beziehen durch: ZENTRALBIBLIOTHEK der Kernforschungsanlage Jülich GmbH,
Jülich, Bundesrepublik Deutschland

# Temperature Dependence of the Anisotropy of the Threshold Energy for Defect Production in Platinum

by

N. Afify

ACKNOWLEDGEMENT

The candidate wishes to express his deep appreciation to Prof. Dr. W. Schilling, director on the institute of solid state research "Institut für Festkörperforschung 9 der KFA Jülich", W. Germany, for sponsoring this work.

The candidate is indebted to Dr. P. Jung "Institut für Festkörperforschung der KFA Jülich" who supervised this work all the way through.

Dr. J. Hemmerich and Mr. E. Küssel have been very helpful with the construction of the irradiation cryostat.

The candidate acknowledges the cooperation of the team of the Van de Graaff, the team of the workshop and the staff of the crystal Lab. of the "Institut für Festkörperforschung der KFA Jülich".

CONTENTS

# ABSTRACT

## ABSTRACT

Platinum single crystals were irradiated with fast electrons along various crystallographic directions to determine the anisotropy of the damage rate by resistivity measurements. The temperature dependence of the anisotropy was obtained by varying the irradiation temperature from 4.5 K to 40 K and 400 K.

The results were interpreted in terms of an anisotropy of the threshold energy for atomic displacement. The evaluation was done by a computer program which fitted a threshold energy profile to the measured damage rates.

The effect of details of the threshold energy profile and the effect of electron beam spreading on the anisotropy of the damage rate was studied. Two models, which may explain qualitatively the effect of temperature on the defect production process, are discussed.

The important results of this work are:

1.) The anisotropy of the damage rate in platinum increases with increasing temperature.

2.) Fitting of the damage rate data by a threshold energy profile gives:

   a) Zones of minimum threshold energy are around the <110> and <100> direction, while the maximum threshold energy is found around the direction <111>.

b) with increasing temperature the area of the zones with small threshold energy around the close-packed directions <110> and <100> decrease.

3.) The increasing anisotropy of the threshold energy with temperature is explained by two mechanisms:

a) The change in the defect pattern between 4.5 K and 40 K due to the instability of close pairs.

b) The defocusing of replacement sequences by thermal lattice vibration.

4.) No safe statements about the temperature dependence of the minimum and the average displacement energy are possible.

# CHAPTER I

## I. Introduction

Fast electrons penetrating in a metal crystal, transfer energy to the lattice atoms. If this energy exceeds the so-called threshold energy for atomic displacement, the atom is permanently displaced from its lattice site. A vacancy is formed at the original site of the atom and an interstitial at a certain distance. The interstitial atom together with its vacancy is called Frenkel pair.

The production of point defects is usually traced by electrical resistivity measurements. Other methods are lattice parameter measurements, diffuse X-ray scattering or field-ion microscopy. At low temperatures the isolated Frenkel pairs influence many physical properties. At elevated temperature they become mobile and eventually react with each other or with other lattice defects. The most important of these reactions are mutual annihilation of the Frenkel pair, agglomeration of individual defects to form extended defects, and interaction with dislocations.

From the lattice structure of a metal it must be expected that the threshold energy depends on the lattice direction along which the atom has been knocked by the electron. As defect production is closely related to the mutual interaction of the lattice atoms, investigation of details of the displacement process can give valuable information on interatomic forces in

the lattice. Furthermore from the directional dependence of the threshold energy the average displacement energy is readily derived. This quantity is of importance for estimating defect production rates at high impact energies. The anisotropy of the threshold energy of platinum has been determined in a previous work /1/ from defect production measurements at 4 K. As the most important technical consequences of radiation damage on material properties occur at elevated temperatures, more information on the displacement processes at these temperatures is needed. It is the aim of the present work to investigate the influence of temperature on the directional dependence of defect production and to derive the anisotropy of threshold energy at elevated temperatures.

Fundamental processes of electrons penetrating matter will be given in chapter II. Previous experimental and theoretical work on the anisotropy of atomic displacement and on the stability of Frenkel pairs will be reviewed in chapter III. The apparatus and the experimental technique will be described in chapter IV. In chapter V the results will be given; an interpretation in terms of anisotropy of threshold energy follows in chapter VI. Finally the results are discussed in chapter VII.

# CHAPTER II

## II. Fundamental processes of electrons passing through matter

An energetic electron passing through matter interacts with the atoms of the lattice by two main processes.

a) Momentum is transferred by the electrons essentially to the nuclei of the lattice atoms. This transfer of momentum (elastic scattering) deflects the electrons from their initial direction causing spreading of the electron beam.

With respect to the lattice atoms these elastic processes excite vibrations or, at large scattering angles, permanent displacement of the knocked-on atoms.

b) energy is transferred by the electrons in inelastic excitation processes. These inelastic processes cause most of the energy degradation of the electron beam. In a metal lattice these processes finally cause heating.

### II.1 Energy loss

The main energy loss mechanism of the irradiating electrons comes from the excitation or ionization of the target electrons or, at higher energies, from bremsstrahlung. The electrons incident on the target assembly posses an energy distribution centered at the accelerator energy. This distribution is shifted towards lower energies and slightly broadened as the beam traverses the window-foil, the cooling medium and the specimen.

Sherman /2/ has calculated the electron energy distribution for a beam of electrons in iron.

The energy loss of electrons has a smooth minimum in the energy range from 1 MeV to 3 MeV. According to calculations given by Nelms /3/, the electron beam suffers the following energy losses within the present experimental apparatus:

13.4 keV in the 12.5 µm stainless steel window.

42.5 keV in the 2 mm wide gap of liquid helium (this energy loss is negligible in the irradiations above helium temperature when gaseous helium is used). This value may be in error by up to a factor of about two, as the exact width of the helium gap between window and specimen may be changed by the play of the specimen holder in the specimen chamber and by bowing out of the window.

22.0 keV in the platinum specimen of, typically, 10 µm thickness.

This means that the average beam energy in the middle of the specimen is lower than the incident beam energy by 0.067 MeV for irradiations in liquid helium and .024 MeV for irradiations in gaseous helium.

Due to the above mentioned uncertainties, and for sake of simplicity, an energy loss of 0.05 MeV was assumed for all irradiation temperatures. This correction is included in the data given in chapters V and VI. A more precise treatment would have to include further refinements of these energy loss calculations.

The first of these involves modification due to the fact that the path length of the electrons passing through the specimen is actually larger than the specimen thickness. This is because of multiple scattering. This topic will be discussed in the next subsection. For the moment, suffice it to say that these corrections are small for thin samples.

The second modification comes into play when the beam energy approaches the threshold energy for defect production in the specimen. In this case, an appreciable degration of the damage rate will occur from the front to the backside of the specimen. In the case that the energy drops below threshold within the specimen, the backside will even remain undamaged. In this case, using the average electron energy in the specimen, will lead to an overestimation of the damage rate value at this energy.

## II.2 Multiple scattering of the electrons

The angular scattering of electrons passing through matter has been treated theoretically by Molière /4/ and Bethe /5/.

By describing the atoms by a Thomas-Fermi potential, Molière showed that the electron distribution for multiple scattering $dn/d\Omega$ in thin specimens is given to a good approximation by a Gaussian,

$$\frac{dn}{d\Omega}(E,\alpha) = (\pi \bar{\alpha}^2)^{-1} e^{-(\alpha/\bar{\alpha})^2} \qquad (2.2.1)$$

where E is the energy of the electron, $\alpha$ is the angular distance between the electron beam and the angular element $\Omega$, and $\bar{\alpha}$ is the Gaussian width of the distribution. $\bar{\alpha}$ is given by /6/.

$$\bar{\alpha}^2 = 4\pi \left(\frac{e^2}{mc^2}\right)^2 \frac{Z(Z+1)\, q\, d}{M} \frac{E'}{(E'-1)^2} (B-1.2) \qquad (2.2.2)$$

where $e^B/B$ gives the average number of collisions per electron and is calculated from the following equation:

$$\frac{e^B}{B} = 7800 \frac{(Z+1)\sqrt[3]{Z}\, q\, d}{A} \frac{1}{1+\frac{3.33\, Z^2}{(137)^2}\frac{1}{E'}} \qquad (2.2.3)$$

and $$E' = \left[(E/mc^2) + 1\right]^2 \qquad (2.2.4)$$

M is the mass of the target atoms and Z and A are their atomic number and atomic weight, respectively. q and d are density ($g/cm^3$)

and thickness (cm) of the target, respectively. The correction term to B in equation (2.2.2) is usually included to fit experimental scattering data in the 1 to 15.7 MeV range in Pt and other metals /7/.

The distributions given by equations (2.2.1) and (2.2.2) are in reasonable agreement with those derived from a theory given by Williams /8/.

A direct consequence of multiple scattering is the increased path length of the electrons that pass through the sample. This in turn increases the probability for a displacement collision. For an initially collimated electron beam at normal incidence to a specimen of thickness d, Oen /9/ (by using the Rose /10/ approximation for the average path length) and Yang /11/ (by using the Rossi and Greisen /12/ results for multiple scattering) gave the same expression for the average increase $\Delta s$ in the path length

$$\frac{\Delta s}{d} = \frac{\bar{\alpha}^2}{4} \qquad (2.2.5)$$

The implication of beam spreading and increased path length in the present experiment will be treated in chapter VI.

## II.3 Electron - Nucleus Collision

For large scattering angles, screening of the nucleus by the electrons becomes negligible. The electron - nucleus interaction is then described by a pure Coulomb interaction.
The maximum transferred energy from the electron to the atom /6/ is

$$T_m = 2\ (m/M)\ mc^2\ (E'-1) \qquad (2.3.1)$$

For a recoil atom whose recoil angle is W with respect to the direction of the incoming electron (see Fig. 1) the transferred energy is

$$T = T_m \cos^2 W \qquad (2.3.2)$$

with

$$0 \leq W \leq 90$$

The differential cross section $\frac{d\sigma}{d\Omega}(E,W)$ describes the probability that a lattice atom is scattered by an electron at an angle W with respect to the direction of the incoming electron. The nonrelativistic expression for the differential cross section was given by Rutherford /13/. The relativistic expression for the scattering of classical electrons was given by Darwin /14/, while N.F. Mott /15/ gave the quantum mechanical expression.

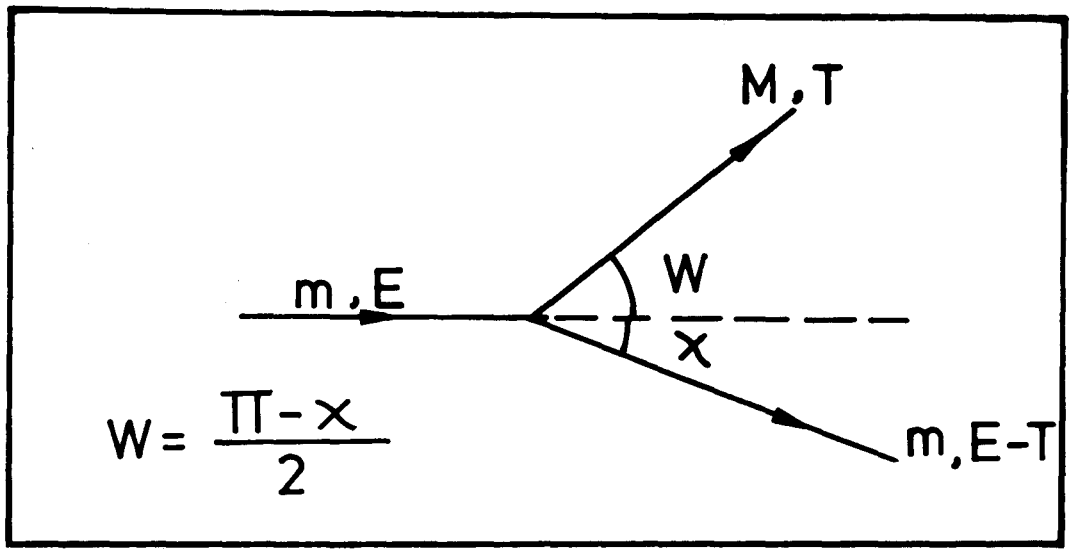


Fig. 1: Schematic representation of an electron - nucleus collision.

For light elements ($Z \leq 32$) the Mott expression is approximated by a formula derived by McKinley and Feshbach /16/:

$$d\sigma_{MKF} = \left(\frac{e^2}{mc^2}\right)^2 \cdot \frac{E'}{(E'-1)^2} \cdot \frac{Z^2}{\cos^3 W} \left[1 - \left(1-\frac{1}{E'}\right) \cos^2 W + \frac{\pi Z}{137} \cdot \sqrt{1 - \frac{1}{E'}} \cdot \cos W \cdot (1-\cos W)\right] d\Omega \qquad (2.3.3)$$

with the solid angle element $d\Omega = 2\pi \sin W \, dW$. For elements with higher atomic number O.S. Oen /17/ gave correction factors $K_o(E,\chi,Z)$ to equation (2.3.3) to approximate the exact Mott values within 3%.

# CHAPTER III

## III. Previous work on atomic displacement processes

Information on the atomic displacement processes have been obtained from theoretical as well as experimental work.

### III.1 Computer experiments

The first modelling of atomic displacement on a computer was done in 1960 by Gibson et al. /18/ for copper. Later simulations were made for bcc-/19/ and for fcc-iron /20/.

In these so-called molecular dynamic calculations one atom is ejected from a normal lattice site with a given energy. All other atoms are initially at rest at their sites. The evolution of the lattice excitation induced by this perturbation are followed by solving the equations of motion until it is clear whether a stable Frenkel pair was produced or not. The directional dependence of the threshold energy for atomic displacement can thus be determined by varying the energy and the direction of the impact. One problem in this calculation is the selection of a suitable two-body potential to describe the mutual interaction of the lattice atoms. For copper the so-called Born-Mayer potential

$$V(r) = A \exp(-r/a) \qquad (3.1.1)$$

with parameter $A \sim 22.5$ keV and $a = 0.197$ nm was found to be appropriate.

These computer experiments showed that in copper (and probably also in other fcc metals) atomic displacements are achieved by so-called replacement collision sequences: The knocked-on atom ejects one of its nearest neighbours on a close-packed lattice direction and occupies its site. In turn this ejected atom replaces another atom on the same direction. This sequence of replacements continues until energy losses to surrounding atoms have lowered the energy to a point where no further replacements are possible. Then an interstitial is formed.

This picture is in qualitative agreement with simple geometrical symmetry considerations: Silsbee /21/ found preferential propagation of energy along dense lattice directions. This led to attributing the experimental threshold energies to displacements along such "easy" directions. The first attempt to derive threshold energies along different lattice directions analytically was undertaken by Sosin /22/, who extended Leibfried's work /23/ on focusing chains to include a calculation of the displacement cross section. He considered displacements in the three main crystallographic directions (100), (110) and (111) of the fcc lattice and applied the calculation to copper. The geometry of the displacement processes is illustrated in fig. 2: the atom K, after having received momentum from the incoming electron, is projected across different lenses formed by the ring atoms B towards the atoms L. The collision processes between atoms K

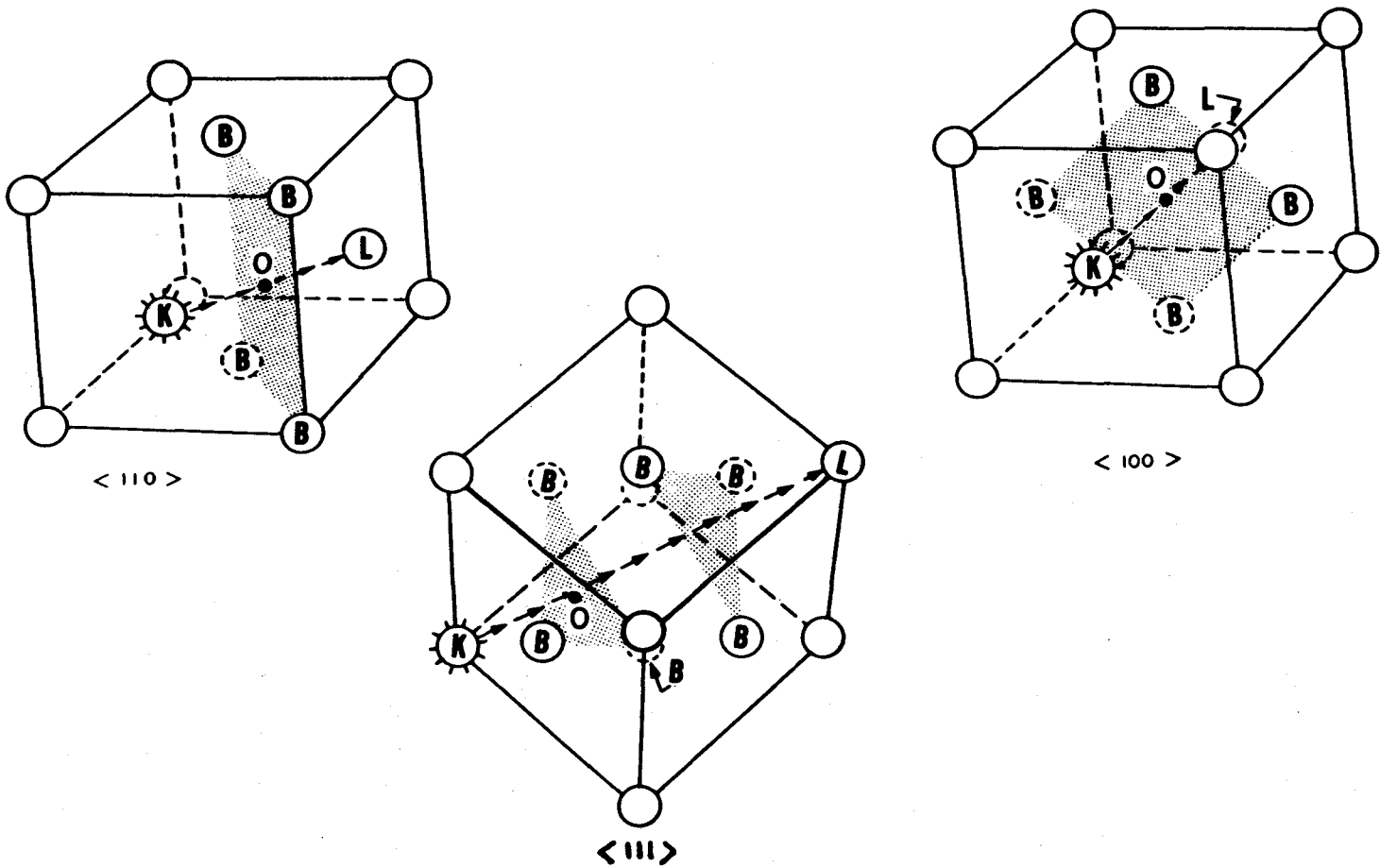


Fig. 2: Schematic diagram of the three fundamental ejection processes in an fcc lattice.

and B are treated in the impulse approximation using central forces between them given by the gradient of a Born-Mayer potential. A further extension of this approach was undertaken by Jan and Seeger /24/, who tried to obtain threshold energies in the full angular space of an fcc crystal by expressing the threshold energy by cubic harmonics. Their attempt is in contradiction with both the computer results of Gibson et al. /18/ and with single-crystal experiments on copper and platinum /1/.

## III.2 Previous experimental results on platinum

A review of experimental as well as theoretical work on the anisotropy of electron radiation damage in metal crystals has been given recently by Vajda /25/. Therefore only results on the anisotropy of the threshold energy in platinum will be treated here in some detail.

The experiments of electron radiation damage in platinum single crystals were done /1,26/ by measuring the variation of the residual electrical resistivity under electron irradiation. In these experiments specimens of about 10 μm thickness were used to reduce multiple scattering of the electrons. Irradiation was done at liquid helium temperature to avoid recovery due to thermal migration of defects.

The direction of the electron beam with respect to the single crystals was changed by rotating the crystals, as shown in fig. 3.

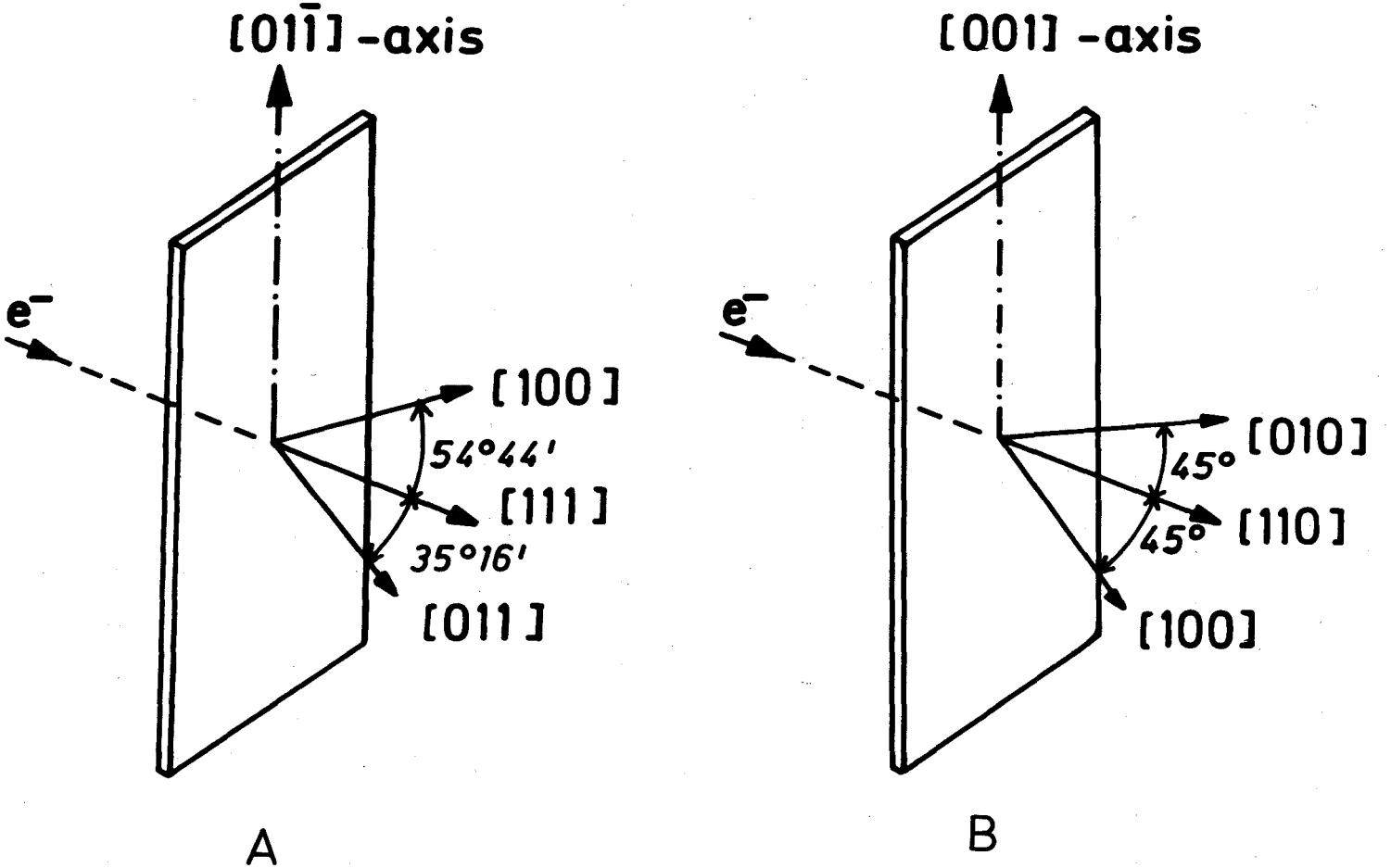


Fig. 3: Schematic diagram showing the change of the irradiation direction in single-crystal Foils as rotated around
A) [01$\bar{1}$]-axis B) [001]-axis

The measured orientation dependence of the resistivity change rate is shown in fig. 4.

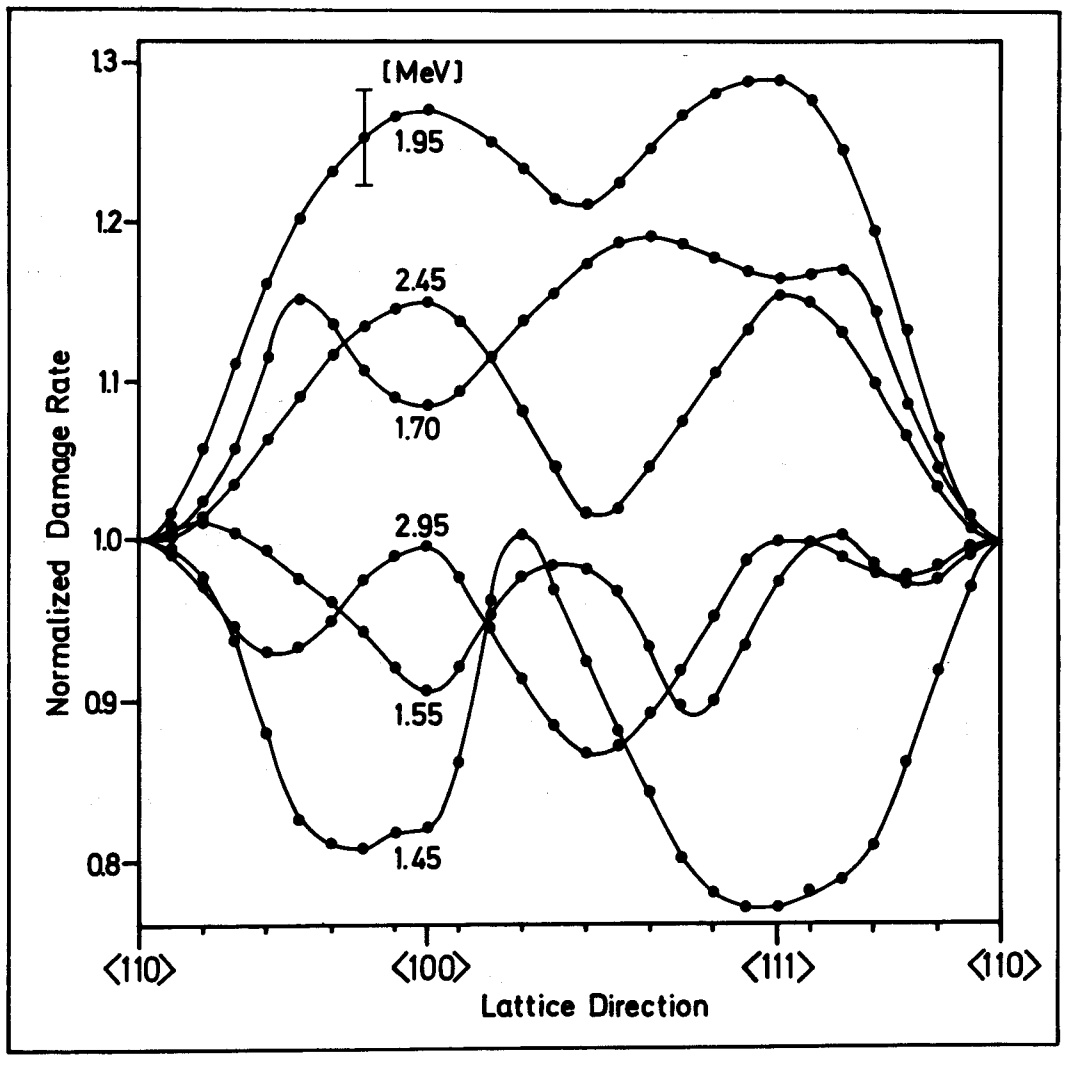


Fig. 4: Damage rates normalized to <110> in platinum as a function of crystal orientation at various electron energies (Ref. /1/).

In a computer analysis of these data, a variable threshold energy surface was used to calculate the displacement cross section in each direction. The best fit was obtained with the threshold energy ($T_d$) surface indicated in fig. 5. As was the case for copper, a ring shaped region was found with a minimum $T_d$ of 33 to 35 eV at about $10^o$ off the <110> direction and another minimum, $T_d$ = 34 - 36 eV at $20^o$ - $25^o$, off the <100> direction. $T_d$ values along the border of the fundamental triangle of fig. 5 are presented in fig. 6. Comparison with the computer data on copper (broken line) shows a general agreement in the low $T_d$ values along the <110> and <100> directions as well as the maximum at <111>. On the other hand the computer result exhibits less structure. In particular it is lacking the minimum $T_d$ belts around <110> and <100>. The analysis finally gave a value for the resistivity increase per unit concentration of Frenkel pairs in platinum of

$$\rho_f(Pt) = (9.5 \pm 0.5)\ 10^{-4}\ \Omega cm/u.c.$$

Jung and Schober /27/ have irradiated platinum crystals of different orientations with electrons of energies between 1.4 and 3.0 MeV, i.e., corresponding to recoil energies between 37 and 133 eV (1.1 $T_d^{min}$ to 3.9 $T_d^{min}$). Subsequent annealing experiments through stage I showed a strong dependence of

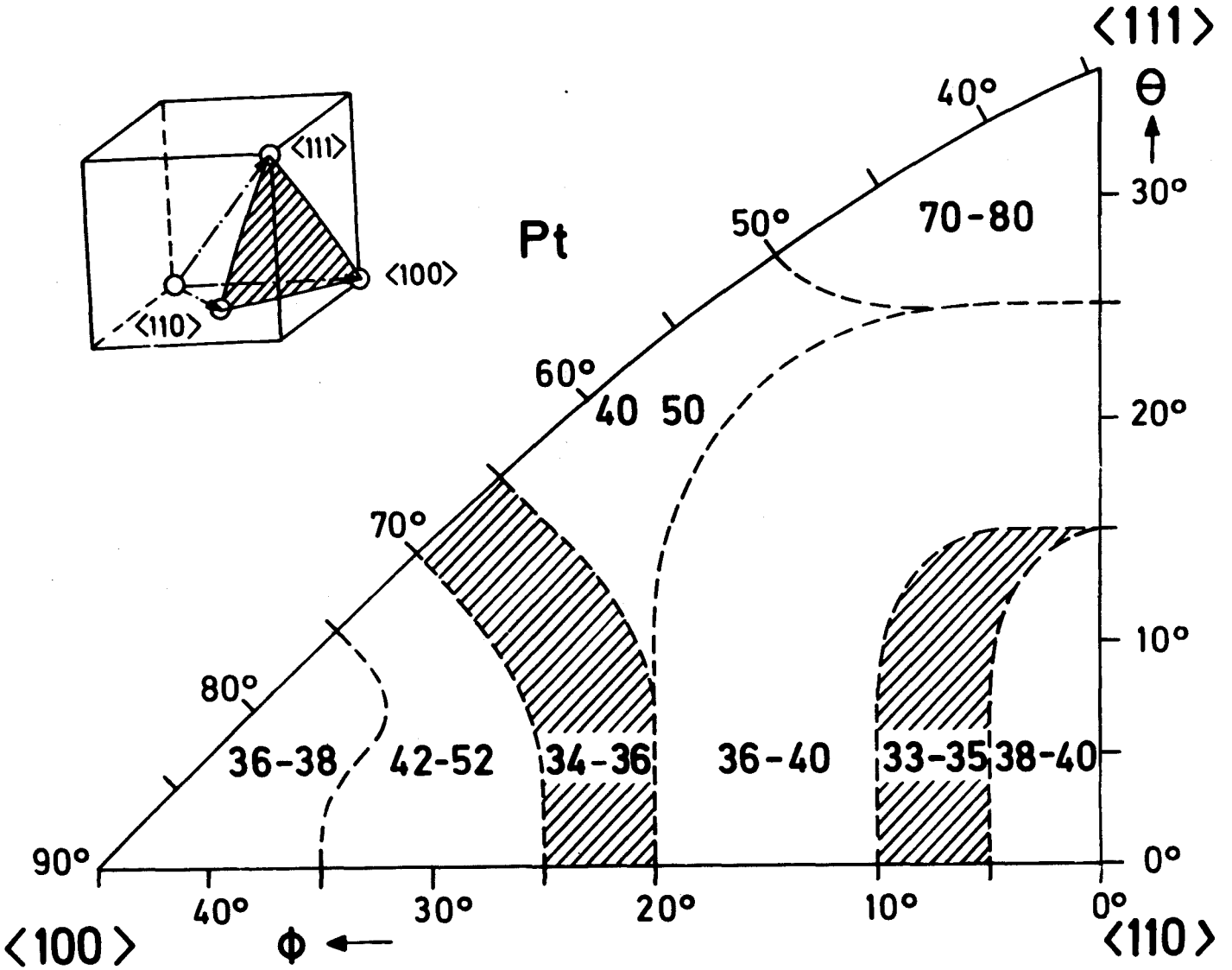


Fig. 5: Threshold energy profile in the fundamental triangle of platinum (Ref. /1/).

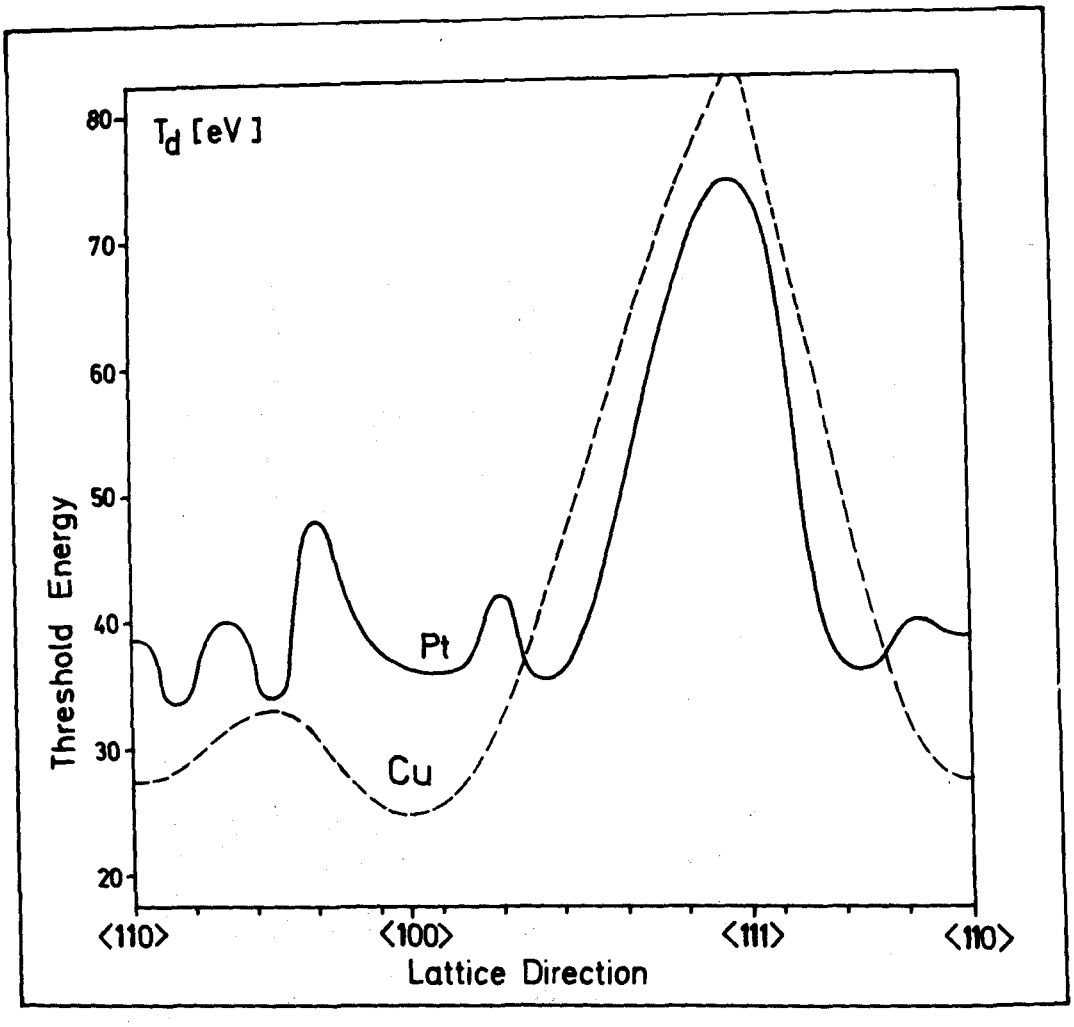


Fig. 6: Threshold energy contours in
platinum (experimental results Ref. /1/)
copper (theoretical results Ref. /18/)

the recovery on energy and crystal orientation, as shown in fig. 7a. Here are plotted normalized production rates of those defects, which anneal in the substages at 9-11 K, 14-16 K, 19-22 K and above 22 K, labelled A,B,C and F, respectively. For recoil energies $T_m$ below 50 eV, the production of close-

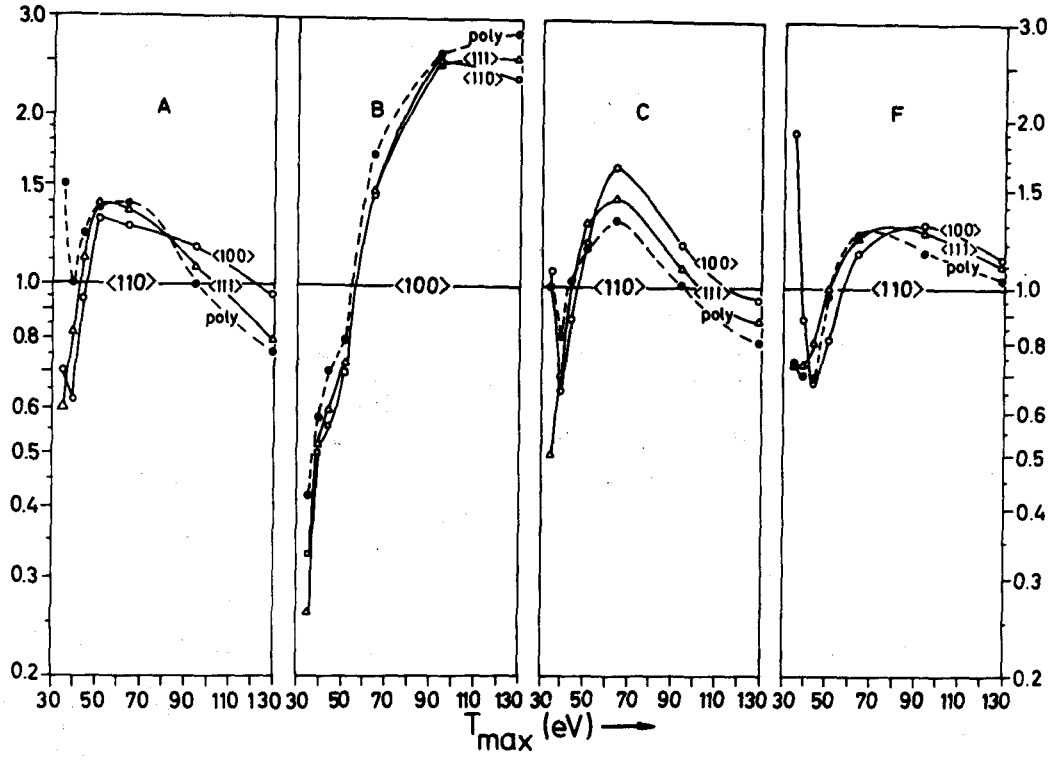


Fig. 7a: Normalized production rates of defects in platinum as a function of maximum transferred energy and irradiation direction, recovering in substages $I_A$(A), $I_B$(B), $I_C$(C), and above $I_C$(F) respectively (Ref. /27/).

pair defects (A,B and C) was strongly favored. Fig. 7a indicates that A and C defects are created by impacts near the <110> direction, while B defects are produced by impacts close to <100>. It was possible to relate the production of these defects to the minimum regions (shaded areas of fig. 5) in the $T_d$ surface. Analysis of the data of Fig. 7a showed (Fig. 7b), that at energies slightly above the minimum threshold energy

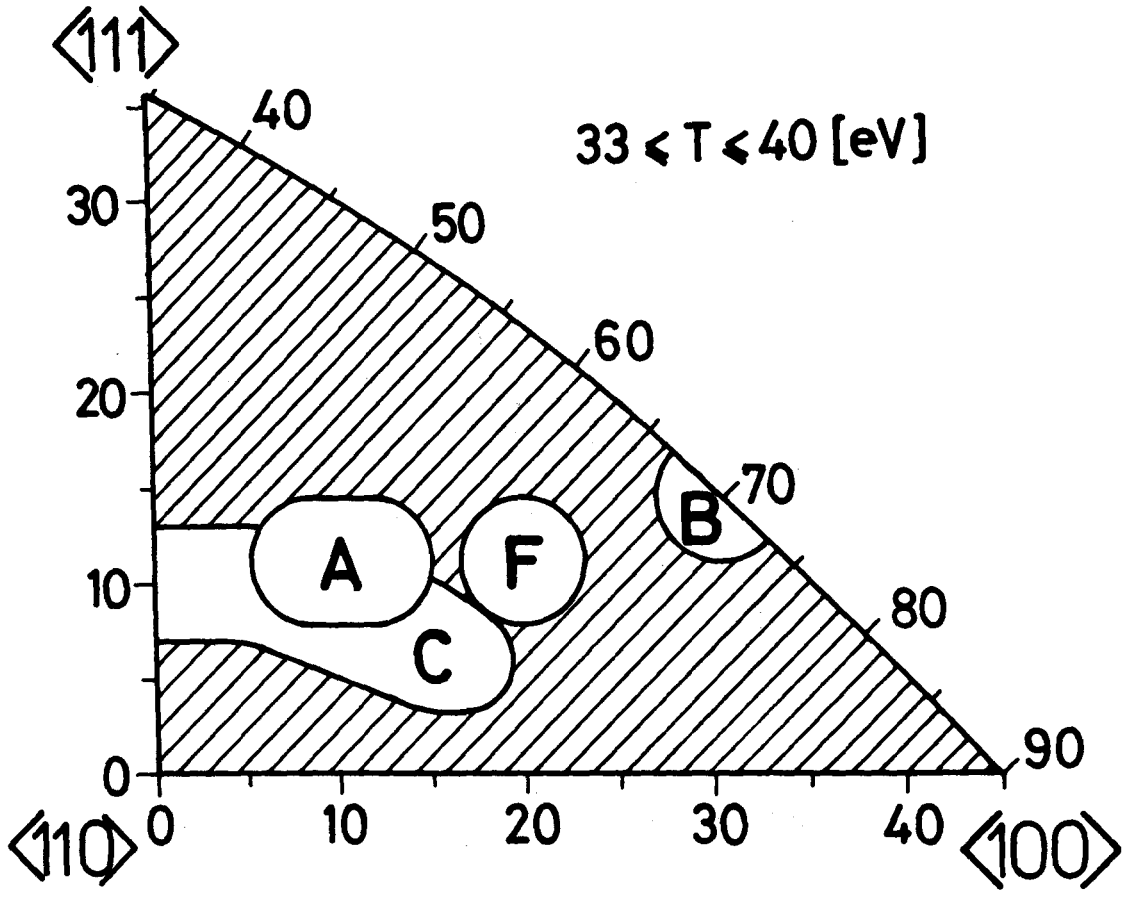


Fig. 7b: Areas in the fundamental triangle of platinum where defects of type $I_A$(A), $I_B$(B), $I_C$(C) and free migration of energies below 40 eV are produced (Ref. /27/).

($T \leq 40$ eV), type B defects stem from impacts in region $20^o$ off <100> on the <100> - <111> boundary, while production of A- and C-defects occurs in the ring $10^o$ off <110>. At higher energies (40-50 eV), production of A-defects tends to cease, while mainly F- and C-production increases.

## III.3 Influence of temperature on the displacement process

Only recently computer simulations were started, which investigated temperature effect on the displacement process by including thermal vibration of the lattice atoms.

Beeler et al. /28/ found for fcc-iron, that the minimum threshold energy was not altered significantly, but that the anisotropy of the threshold energy tended to be reduced by including lattice vibrations. A further result was, that the threshold energy for permanent displacement along a certain lattice direction was distributed over a range of values instead of being unique as was found in a rigid lattice.

Recent computer simulations of Tenenbaum et al. /29/ for copper gave a reduction of the minimum threshold energy by less than 5 eV and a reduction of the length of replacement sequences along <110> and <100> between 0 K and 293 K.

Experimental results on the anisotropy of radiation damage in metals around room-temperature have been obtained by the high voltage electron microscopy (Reference 30 cites several examples). In these experiments the loop-nucleation and growth or the growth of preinjected dislocation loops is measured as a function of electron energy and direction. The growth rate of the loops is then used as a measure of the atomic displacement rate: Drosd /31/ has measured the minimum threshhold energy for copper at different temperatures. He found,

that the threshold energy decreased with increasing temperature.

In a different approach Roth et al. /32/ investigated dislocation pinning in copper after electron irradiation at 78 K and 400 K. They found a threshold energy at 400 K which was below the value at 78 K by about 3.5 eV. Lauzier et al. /33/ also did dislocation pinning experiments on copper and found a decrease of about 1.5 eV between 75 K and 220 K. The only experiments using resistivity measurements were performed on copper by Becker et al. /34/. They did not find a measureable change of the minimum displacement energy between 8 K and 93 K. This means that in all experiments a reduction of the minimum threshold energies, at least at higher temperatures, was found. On the other hand, experimental results on the temperature dependence of the anisotropy of the threshold energy are still lacking.

## III.4 Defect stability

The stability of a vacancy-interstitial pair greatly depends on the time-scale and the temperature considered.

The effect of the time-scale on the defect stability was studied in computer simulations by Doran and Schiffgens /35/. The processes following the transfer of energy to a lattice atom may be viewed as taking place in three phases.

The first extends from the creation of the primary knocked-on atom to that time ($10^{-14}$ - $10^{-13}$ sec.) when the energy of the most energetic atom in the cascade falls below $T_d$. The second phase lasts from the end of cascade expansion until sufficient order is restored to distinguish distinct and stable vacancies, interstitials and clusters throughout the cascade region. The significance of this phase stems from the fact that, except for the sum total of formation energies for the eventually stable vacancies, interstitials and clusters, the energy deposited by the radiation is spent causing atom turbulence in the neighbourhood of the cascade as the energy flows out to the rest of the lattice atoms. For this phase a period of $10^{-12}$ to $10^{-11}$ sec. is required during which local order is sufficiently reestablished for diffusion processes to proceed later on by thermal activation. Finally, there is the third phase, the short-term annealing phase, characterized by thermal activation processes. During this phase, the defects either annihilate,cluster or escape from the cascade to be absorbed by other sinks.

For most metals, two broad temperature regimes can be identified in annealing experiments: a low temperature one (stage I) in which only interstitials are mobile and a high temperature one (stage III) in which vacancies migrate.

The temperature effect on defect stability in platinum was studied by Sonnenberg, Schilling and co-workers /36-40/. A typical isochronal annealing curve for electron irradiated platinum is shown in fig. 8. On the abscissa the recovery stages I, II and III are identified.

The stage I consists of a number of subpeaks ($I_A$, $I_B$, $I_C$, $I_D$ and $I_E$). Stages $I_A$, $I_B$ and $I_C$ are ascribed to the recombination of so-called close Frenkel pairs; that is recombination of Frenkel pairs where the interstitial and vacancy are so close together that the energy barrier for recombination is lowered appreciably by their mutual interaction. In stages $I_D$ and $I_E$ interstitials are thought to undergo free migration. Stage $I_D$ is associated with the recombination of interstitials with their own vacancies (correlated recombination). Stage $I_E$ is associated with recombinations involving other vacancies, and requires a larger number of steps (uncorrelated recombination). During $I_E$, the freely migrating interstitials can not only recombine with vacancies, but can also react with other interstitials or impurities, thereby becoming trapped in immobile agglomerates. These latter reactions lead to the retention of vacancies and interstitials in the lattice, so that recovery is not complete at the end of stage I. In stage II rearrangements take place among the initial clusters formed in stage I, whereby the small interstitial clusters are gradually eliminated and larger

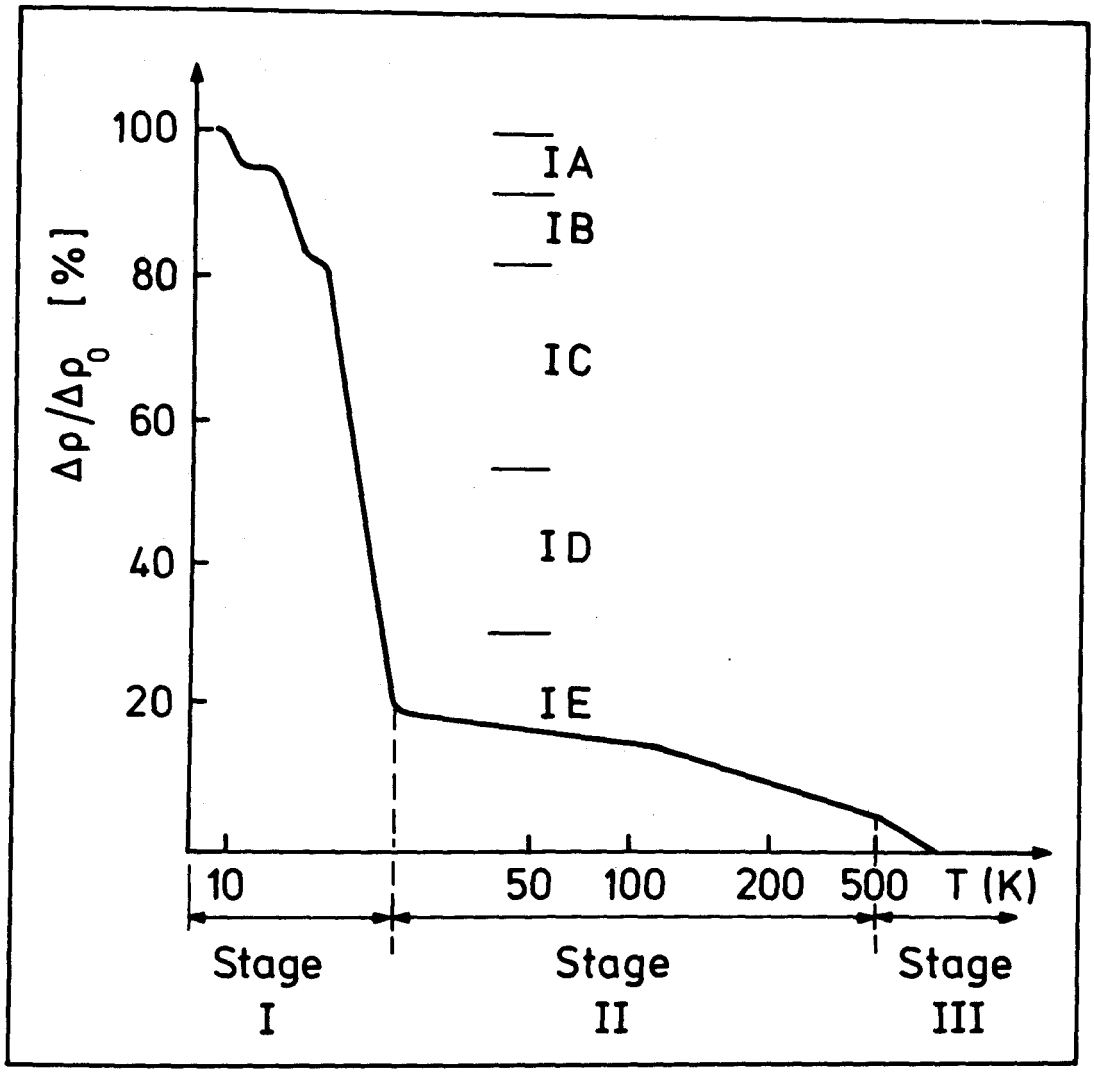


Fig. 8: Isochronal recovery of platinum irradiated at 4.5 K with 3 MeV-electrons to $\Delta\rho_0 = 56 \cdot 10^{-9}$ Ωcm (Ref. /36/).

clusters grow at the expense of the smaller ones. This process is accompanied by some interstitial-vacancy recombinations which give rise to the observed resistivity decrease in stage II.

Also the small substages near 120 K and between 200 and 500 K are probably not intrinsic in character but are related to detrapping of interstitial from residual impurities. The stage III recovery process is interpreted as vacancy migration in the temperature range above 450 K by taking into account the formation and more rapid migration of divacancies.

In resistivity measurements of defect production, the annealing stages I and III are reflected in a step wise reduction of the damage rate /41/ at the corresponding temperatures. To reduce possible errors the present experiment was done at temperatures off the main annealing stages, namely at 4 K (below stage I), 40 K (above stage I) and 400 K (below stage III).

# CHAPTER IV

## IV. Experimental technique

### IV.1 The specimens

The single crystal foils used in these experiments were prepared by vacuum deposition of platinum on rocksalt substrates.

The specimen material was cut from 6 mm platinum rods of 99,999% purity, from Degussa GmbH Frankfurt, West-Germany. The substrate materials were rocksalt (NaCl) single crystals without mosaic spread from Oriel GmbH Darmstadt, West-Germany. Substrate crystals were prepared by cleavage of crystals of the desired orientation (<100>, <110>, or <111>) from as-received NaCl crystals of dimensions 20x20x70 mm.

The cleaved crystals were then polished with a solution of 50% methyl alcohol - 50% distilled water,and subsequently tempered at 500°C for one hour. The shape of the substrates is shown in fig. 9A.

The platinum single crystal specimens of different orientations were grown epitaxially on the above substrates. The platinum was evaporated by electron beam heating in a vacuum of $10^{-8}$ to $10^{-9}$ mbar at evaporation rates between 2 nm/sec and 6.5 nm/sec. The substrate temperature was about 370°C. In the first attempts /42/, especially for the <111> orientation, an intermediate silver film on the substrates was used to suppress twin formation. Later on it was possible to produce platinum single crystals of all orien-

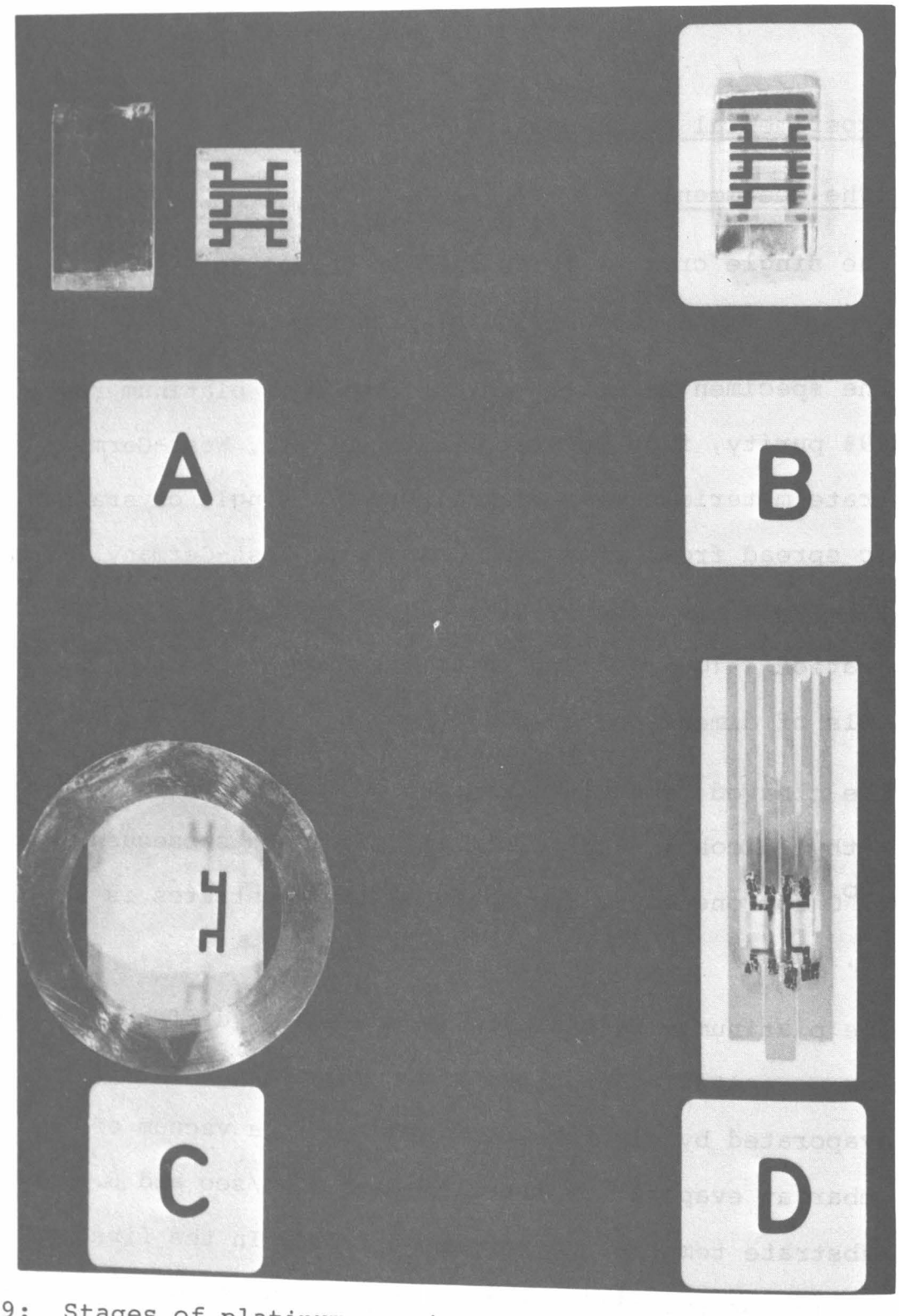


Fig. 9: Stages of platinum specimen preparation by vacuum deposition
A - Rocksalt substrates and the mask
B - The specimens after vacuum deposition
C - The specimen being attached to a colloid film
D - Two specimens after mounting on the alumina plates

tations with thicknesses up to 10 µm without this silver film. By using the masks shown in fig. 9A , three specimens of the shape shown in fig. 9B could be produced simultaneously. This shape was used for four-point resistivity measurements. It allowed the welding of potential leads without distortion of the central part of the specimens. After dissolving of the substrates in distilled water, the platinum specimen was attached to a colloid film as shown in fig. 9C. The colloid film consisted of a 1 : 4 mixture of HP 5000 5% in amyl acetate from Dynamit Nobel and isoamyl acetate ester.

The specimen holder was an alumina plate that had been metallized with Ni to complete the circuits from the samples to the lead-in wires. Two samples were spot welded to the nickel strips on a single plate as shown in fig. 9D.

After spot-welding the colloid film was dissolved in acetone. To remove stresses, the specimens were tempered by resistance heating for 30 minutes at 1400°C in air and afterwards slowly cooled to room temperature (cooling rate: about 6°C/min.).

The alumina plates were finally inserted into a plate-holder which is shown in fig. 10. This plate-holder was used for irradiation of the specimen in the cryostat and for resistivity measurements. It consists of a stainless-steel holder fixed to a stainless-steel tubing, which contains the six glass insulated copper lead-in wires. The wires are spot welded to the

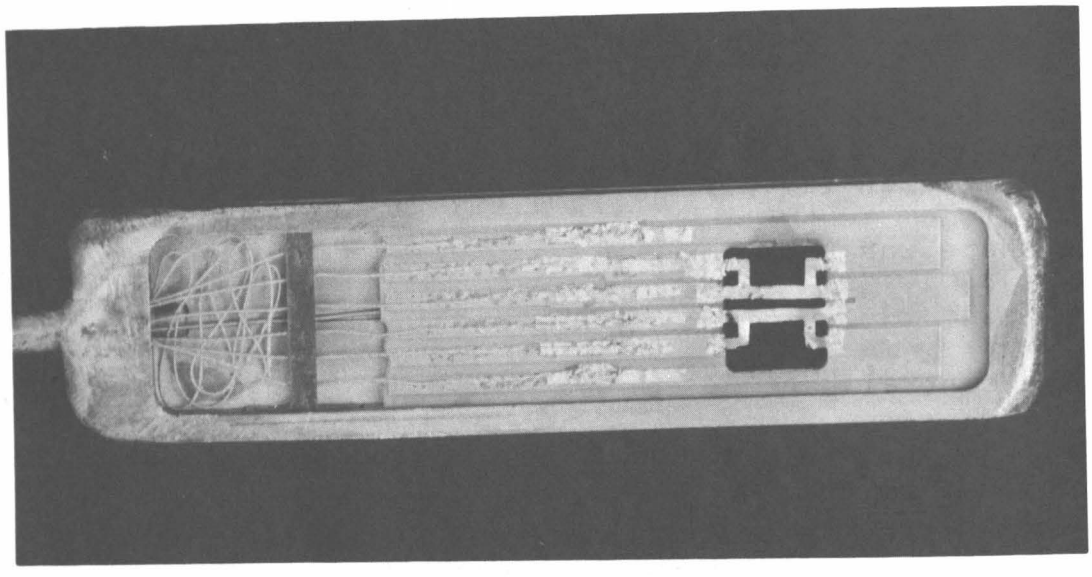

Fig. 10: Photograph of the specimen holder with the alumina plate and two specimens mounted.

Ni strips on the plate by use of Pt foils between the copper and nickel. The specimen temperature was measured by a thin, shielded Ni-NiCr thermocouple just behind the specimens. After mounting the specimens on the specimen-holders, they showed room-temperature-to-helium-temperature resistivity ratios of 170 to 240. Typical Laue transmission patterns of the specimens with the three orientations are shown in fig. 11-13.

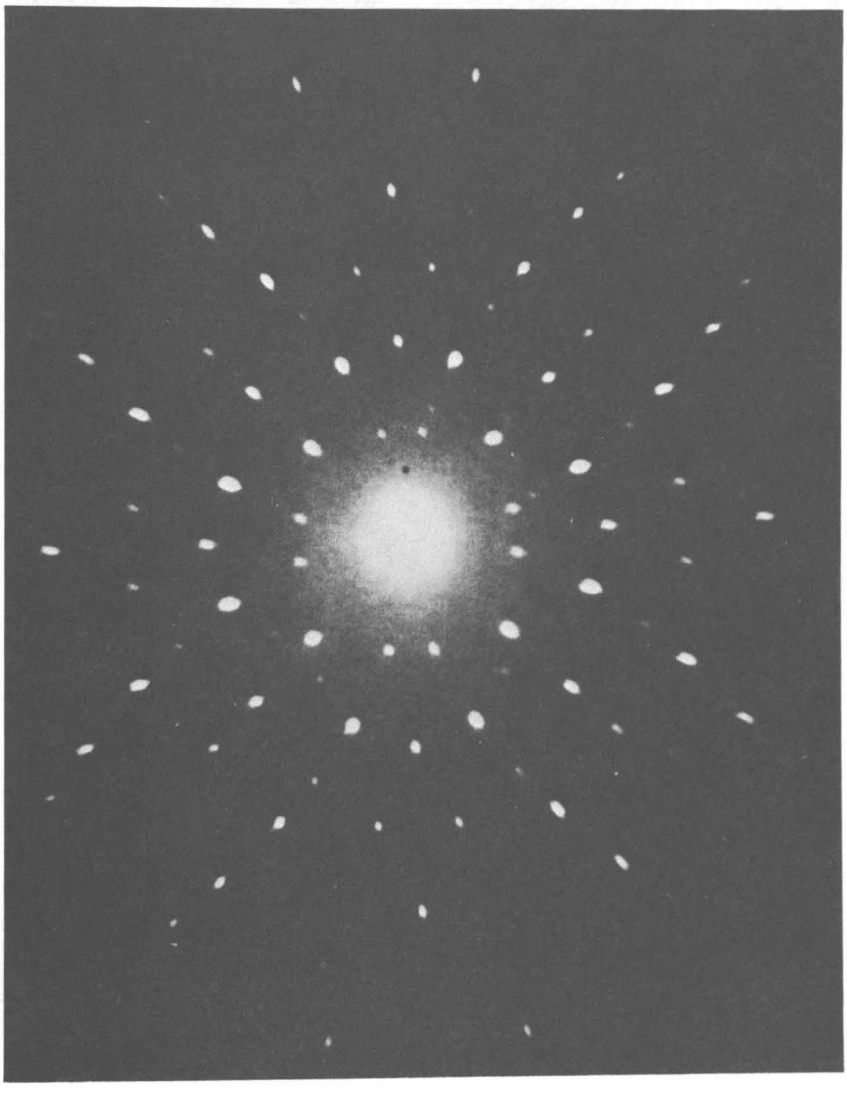

Fig. 11: Laue transmission pattern of a 10μm Pt specimen with (100) orientation and a <100> vertical axis.

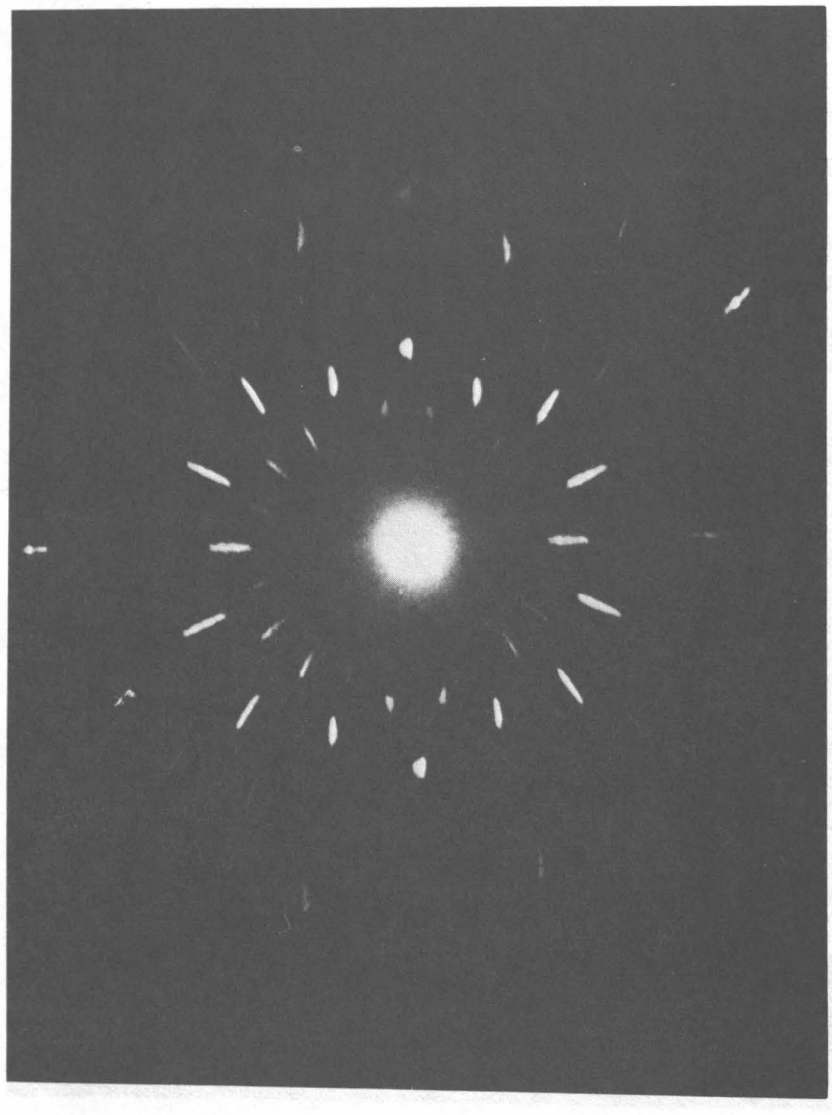

Fig. 12: Laue transmission pattern of a 10 μm Pt specimen with (110) orientation and a <100> vertical axis.

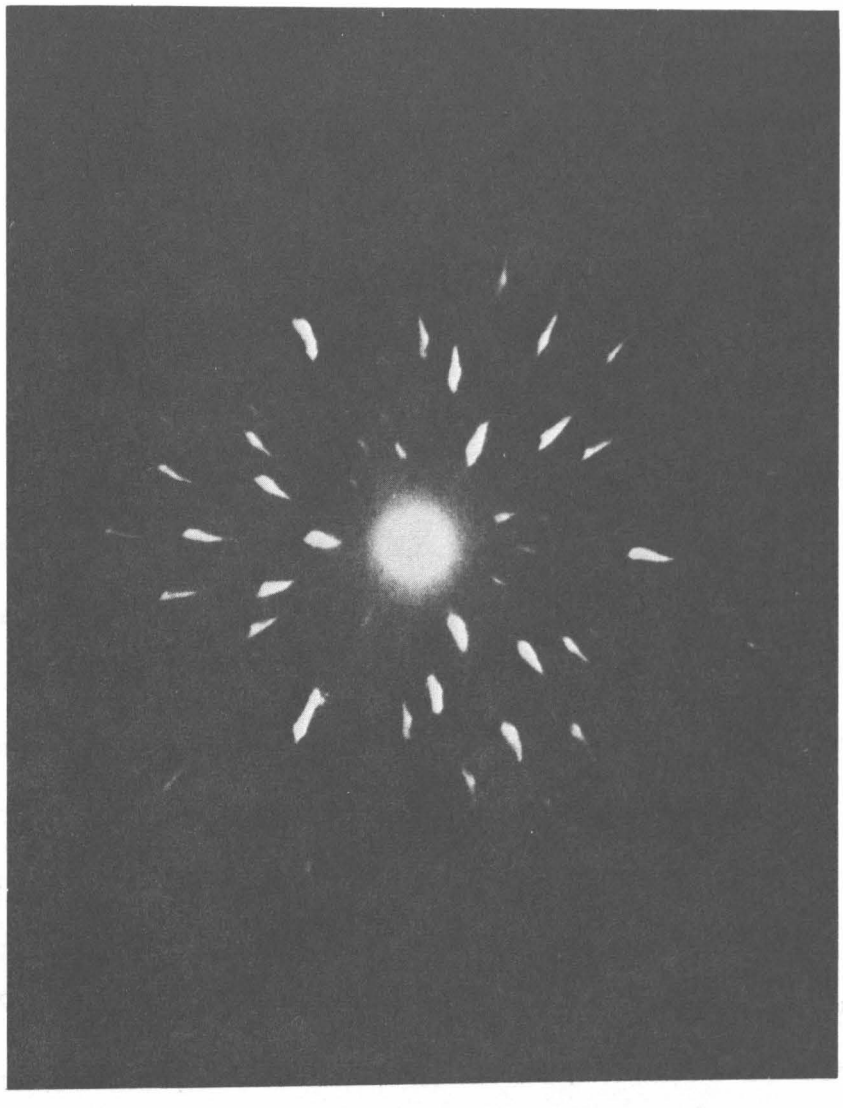

Fig. 13: Laue transmission pattern of a 10 μm Pt specimen with (111) orientation and a <110> vertical axis.

## IV.2 The cryostat

Irradiations were made with the samples in a cryostat that allowed the temperature to be varied between 4.5 K and 600 K. Resistivity measurements were at liquid helium temperature. Sample orientation was varied by rotating the whole irradiation chamber.

The cryostat is shown in figures 14-16. In fig. 17 the mechanical part of the cryostat is shown schematically. With the motor, M1, the specimens can be moved up to the irradiation chamber (IC) and down to the measurement chamber (MC). With the potentiometer, P1, the vertical position of the specimen is indicated. The irradiation chamber, including the specimens, is rotated using motor, M2. The rotation angle is limited to $\pm$ 55$^{o}$ by two switches. With the potentiometer, P2, the rotation angle was measured to an absolute accuracy of $\pm$ 0.5$^{o}$. This error includes relative movements of the specimen-holder in the irradiation chamber.

Figures 18-19 show the two helium circuits used for cooling the specimens during the irradiations and supplying the liquid helium for resistivity measurement.

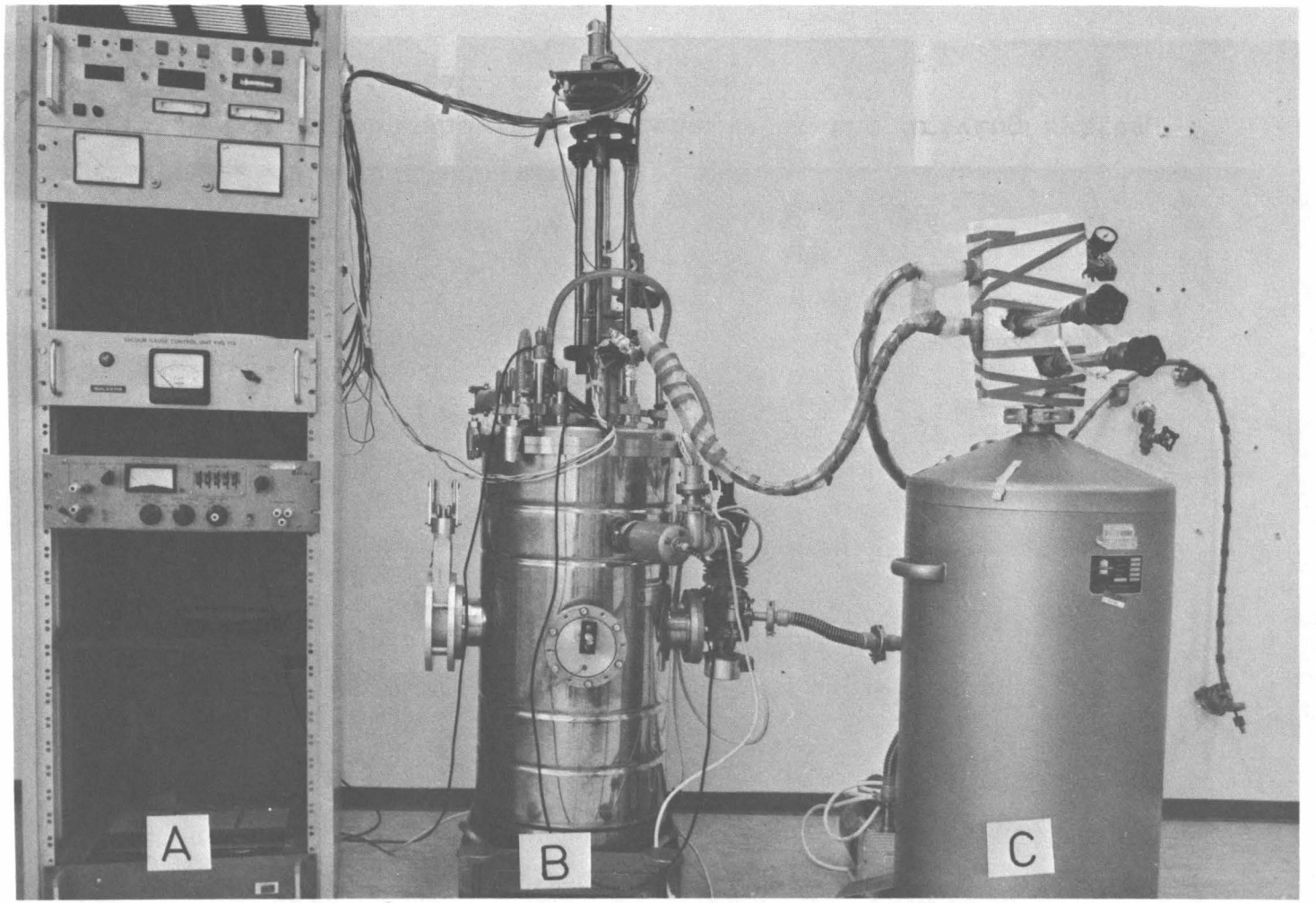


Fig. 14: Photograph of the irradiation facility:

A) The control pannel for the driving motors, the vacuum system and the heater.

B) The irradiation cryostat

C) The liquid nitrogen dewar containing the pre-cooler

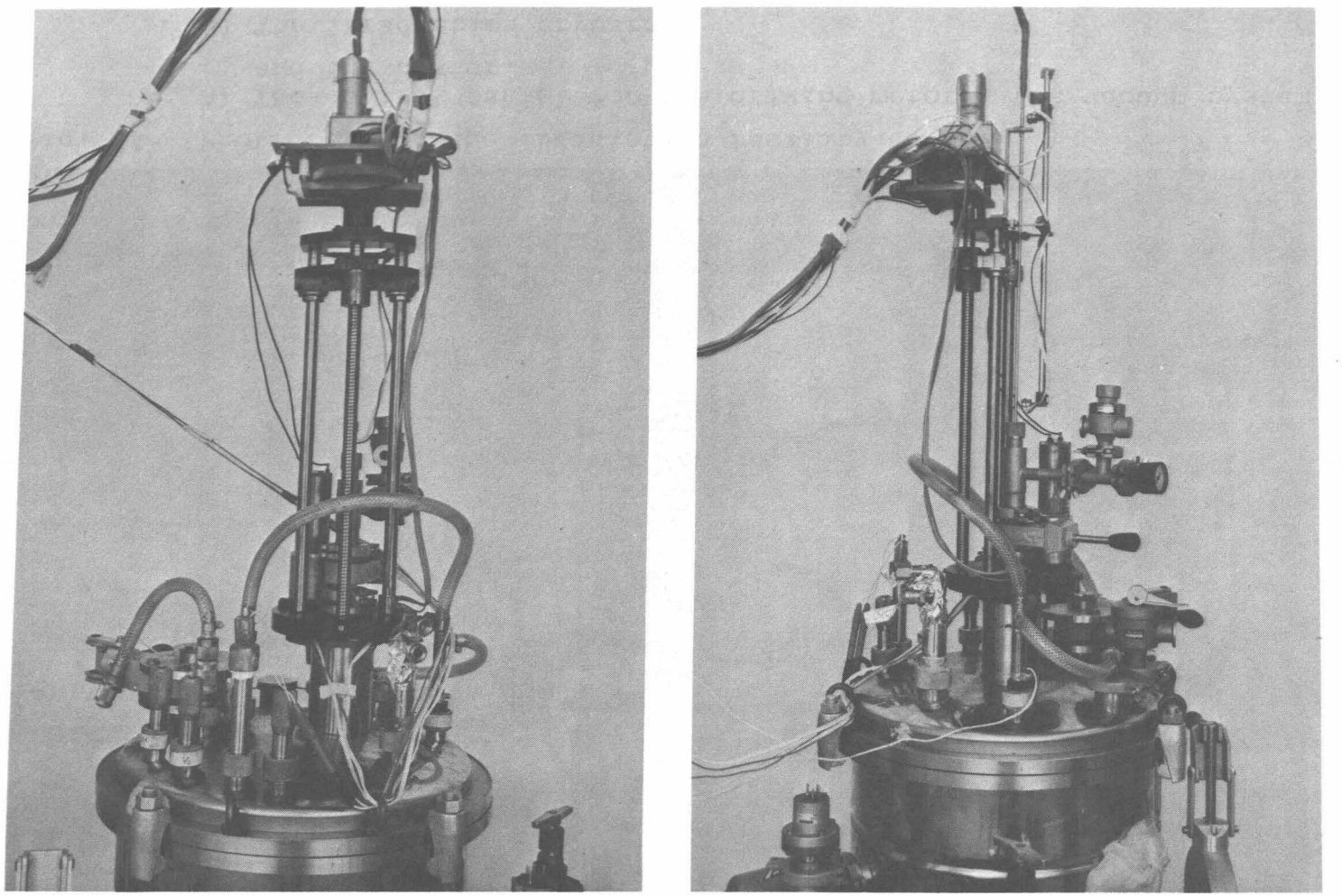

Fig. 15: Photographs showing the details of the driving system of the cryostat from two sides

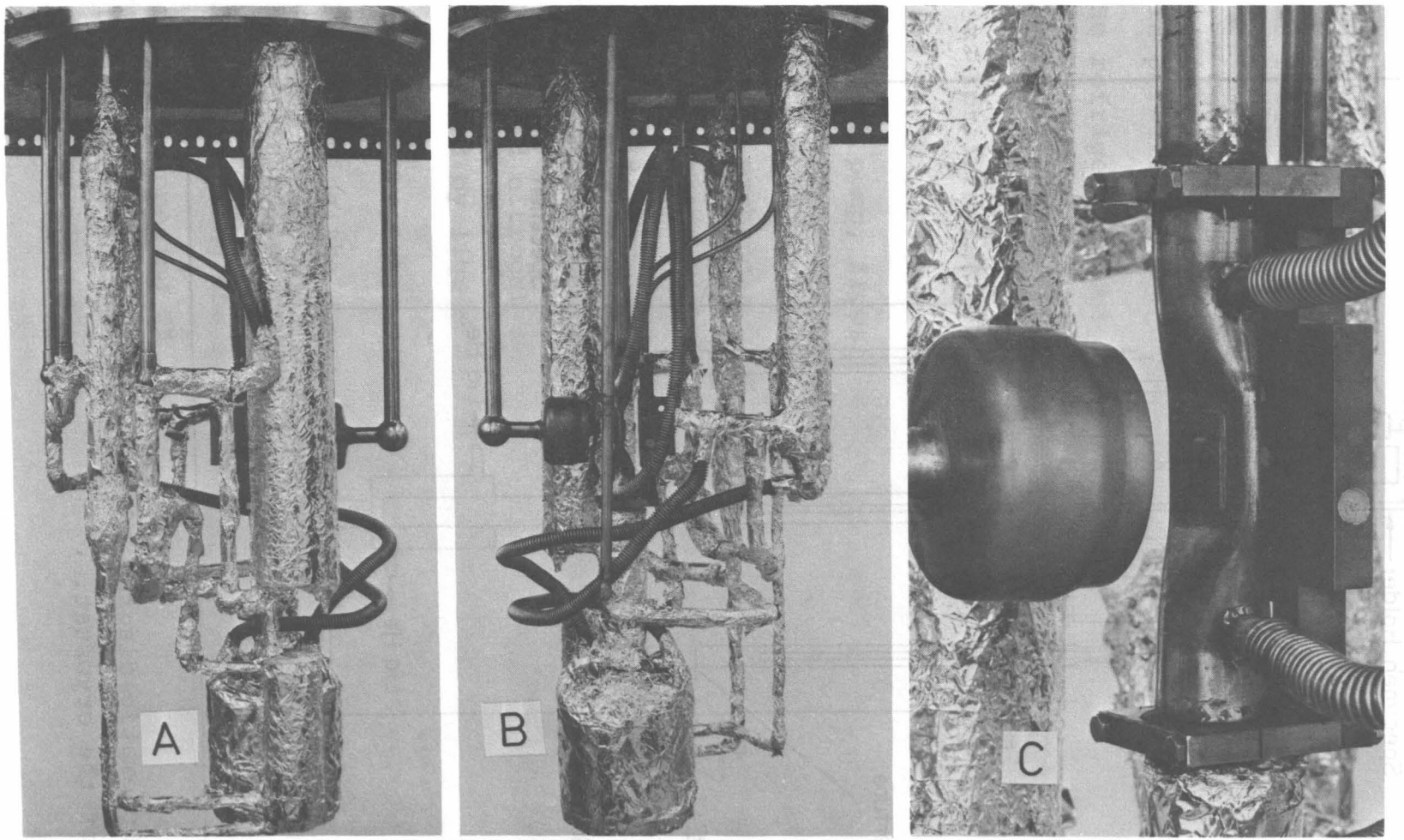


Fig. 16: Photographs showing details of the inner parts of the cryostat
A,B) The cooling system and the measuring chamber, wrapped with super-insulating foil.
C) The Faraday cup, the irradiation chamber and the aperture (from left to right).

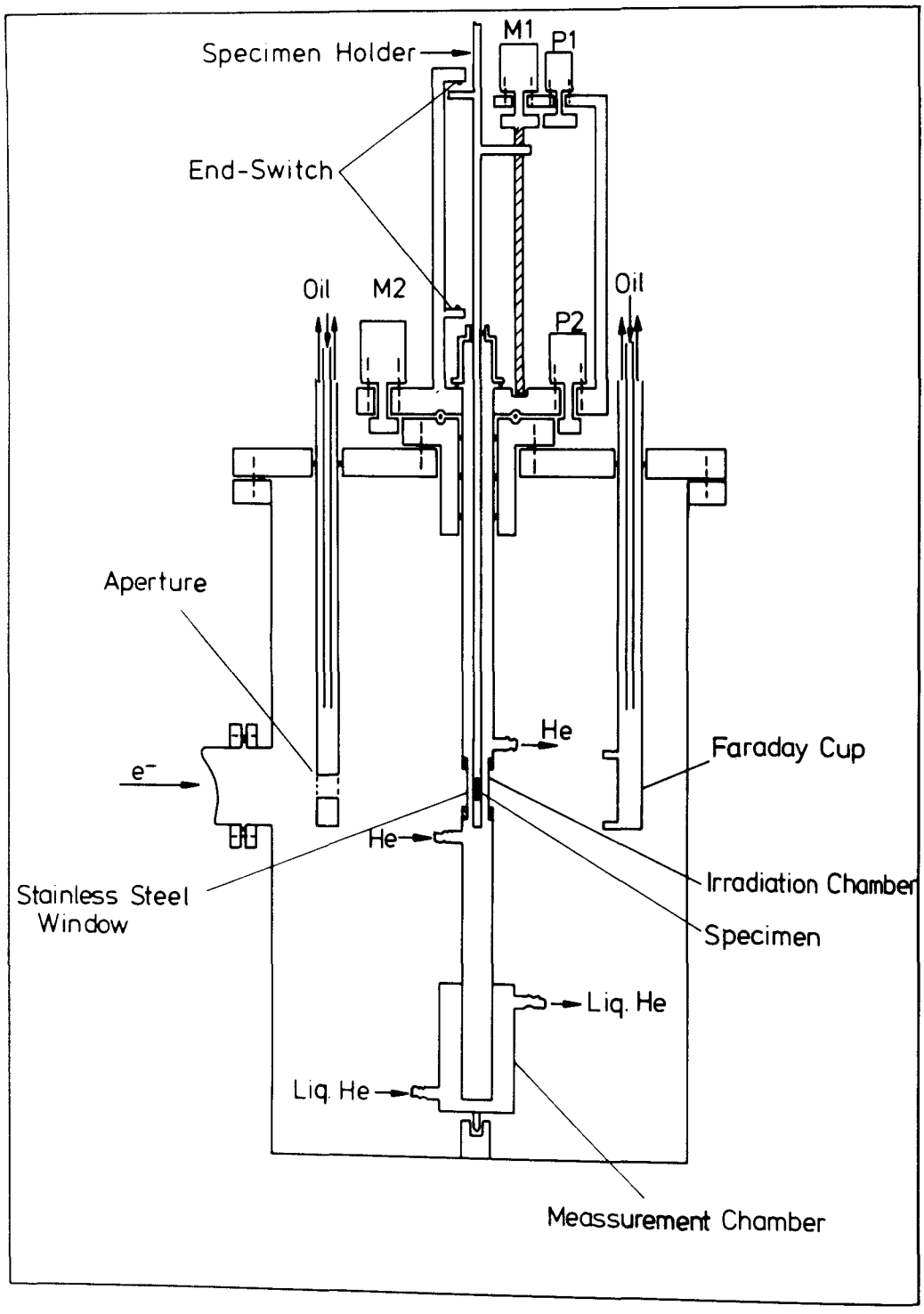


Fig. 17: Schematic diagram of the mechanical part of the cryostat.

The temperature in the irradiation chamber could be varied as follows:

Opening valves V2 and V3 places the irradiation chamber in parallel with the measurement chamber across the liquid He refrigerator output so that both chambers are at 4.5 K for this mode of operation (fat line in Fig. 18).

For irradiation above room temperature V4 and V6 are open and V1, V2, V3 and V5 are closed. Helium gas, circulated by an external pump, flows through the counterflow heat exchanger, HE, the cooler, CO (not in operation) the IC and back through the heat exchanger. The MC remains at 4.5 K. The both circles of gaseous and liquid helium are represented by the fat lines in fig. 19. For irradiation below room temperature V2, V3 and V6 are closed; V1, V4 and V 5 are open. The pre-cooler, PC, is cooled by liquid nitrogen and since V1 is open, the main cooler, CO, is cooled by liquid helium from the refrigerator.

A vacuum below $10^{-6}$ Torr is maintained in the cryostat. For changing the specimen holder in the cryostat, the specimen holder is pulled upward above the valve V7 which then is closed. After replacing the specimen holder the volume above V7 is evacuated by opening V8 before V7 is opened again. This procedure is necessary to avoid freezing of air to the cooled inner parts of the cryostat. Two specimens, generally of different orientation,

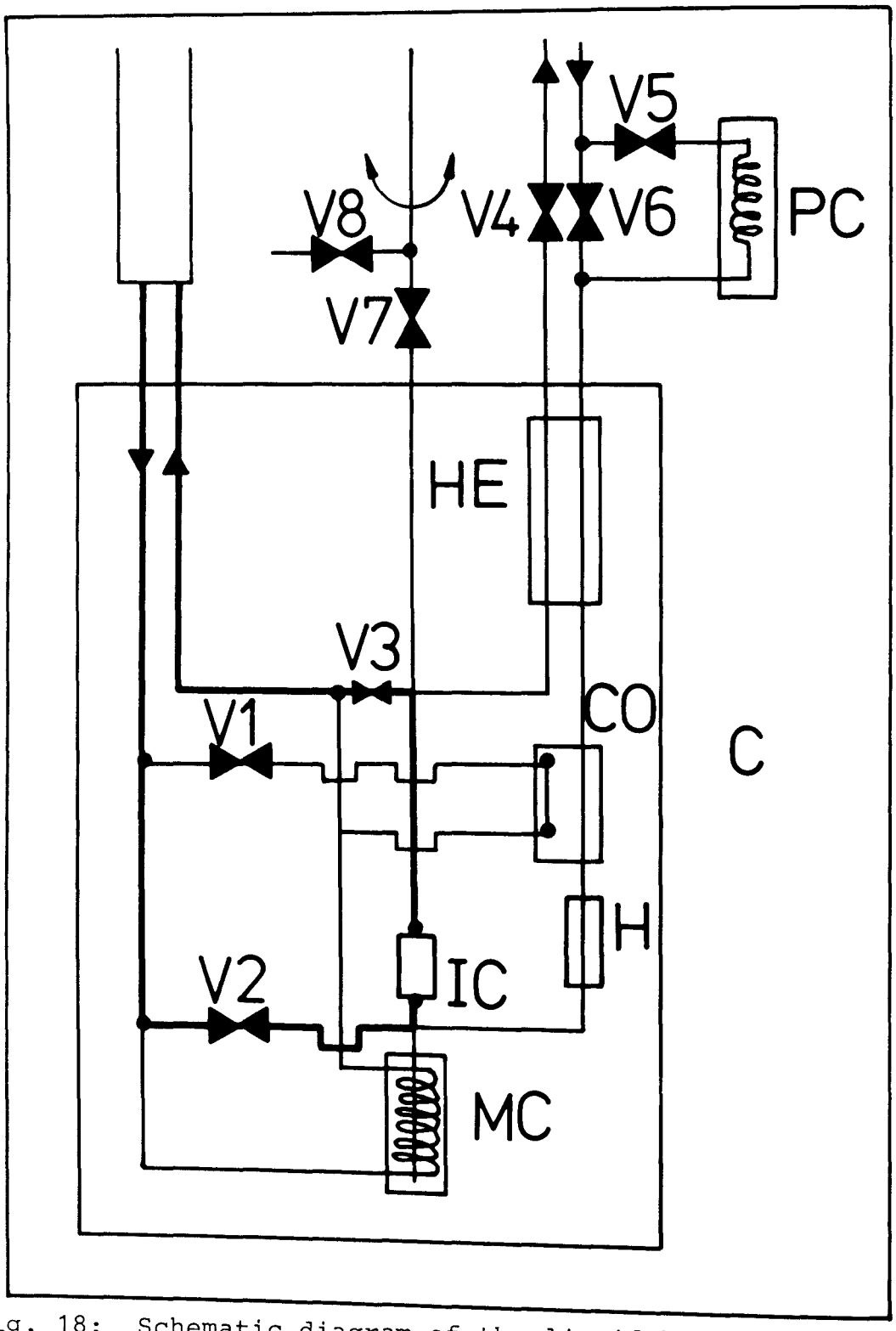


Fig. 18: Schematic diagram of the liquid helium cooling circuit used for the irradiation at 4.5 K.

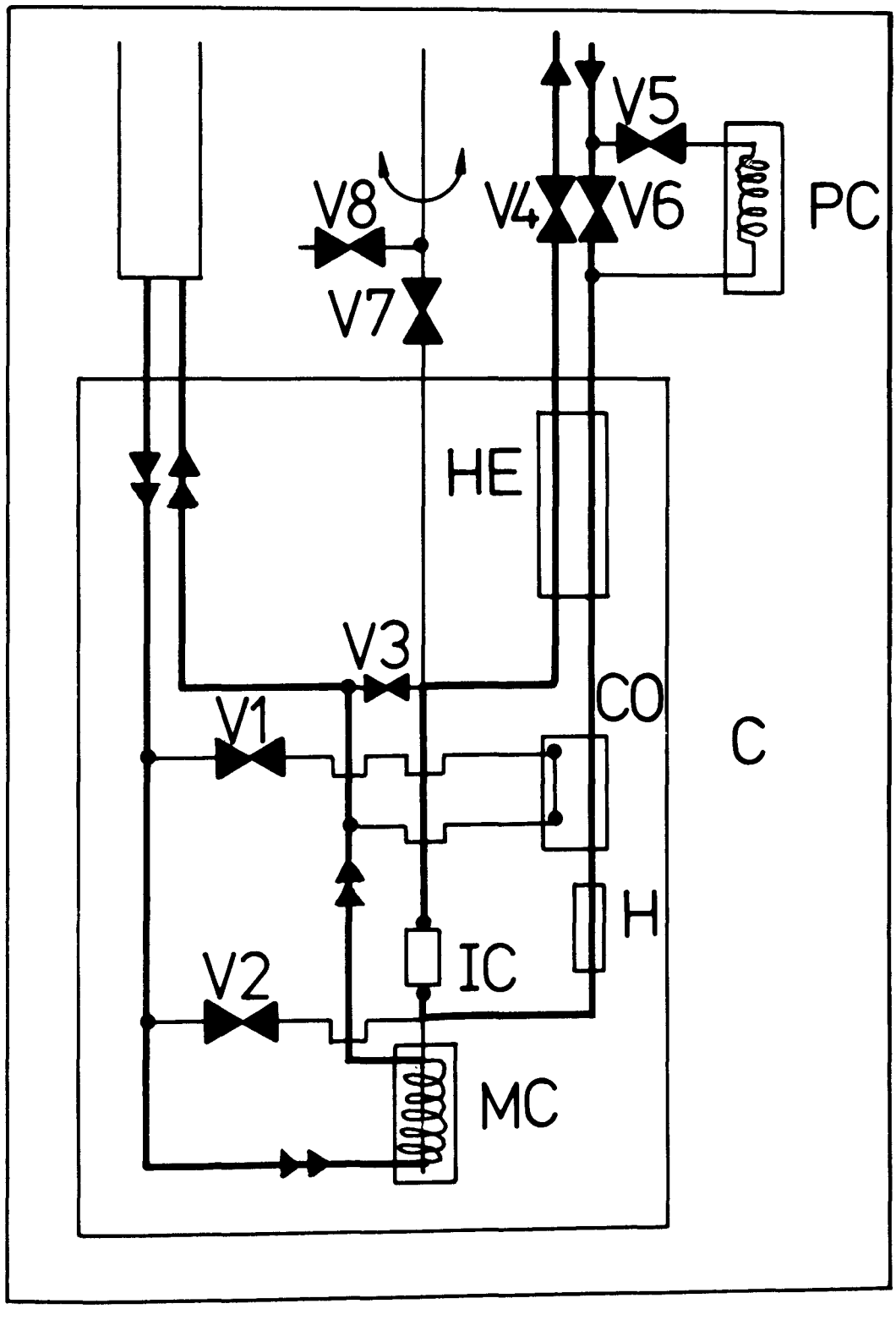


Fig. 19: Schematic diagram of the liquid helium cooling circuit (→→) for the resistivity measurements in the measuring chamber and the gaseous helium circuit (→) used for irradiation above 40 K.

were irradiated simultaneously in this cryostat.

The irradiation with monoenergetic electrons was made at the 3 MeV Van de Graaff Accelerator of the "Kernforschungsanlage Jülich, West-Germany" /43/. The cryostat was connected to the beam line which is shown in fig. 20. The electron beam was spread by quadrapol lenses uniformely across the specimens. The energy of the beam was calibrated by the $Be^{10}$ (e,n) reaction, with the neutrons being detected by the Ag (n,$\gamma$) reaction. The absolute beam current was measured by a Faraday cup in front of the specimen before and after each irradiation. The current density used in the present experiments was typically 10 $\mu A/cm^2$ corresponding to 6.2 $10^{13}$ electrons/$cm^2$sec.

A Faraday cup behind the irradiation chamber was used for checking the constancy of the beam current with time.

A schematic diagram of the resistivity measuring apparatus is shown in fig. 21. A highly stabilized current I flows through the two specimens S1 ,S2 and the standard resistor R. The voltage drops across S1, S2 and R were amplified by a factor of $10^3$ or $10^4$ by a precision amplifier before measurement by a digital voltmeter. The direction of the measuring current could be reversed by an inverter switch to eliminate errors by thermal voltages. Errors caused by fluctuating thermal voltages were reduced by repeating each measurement at least once.

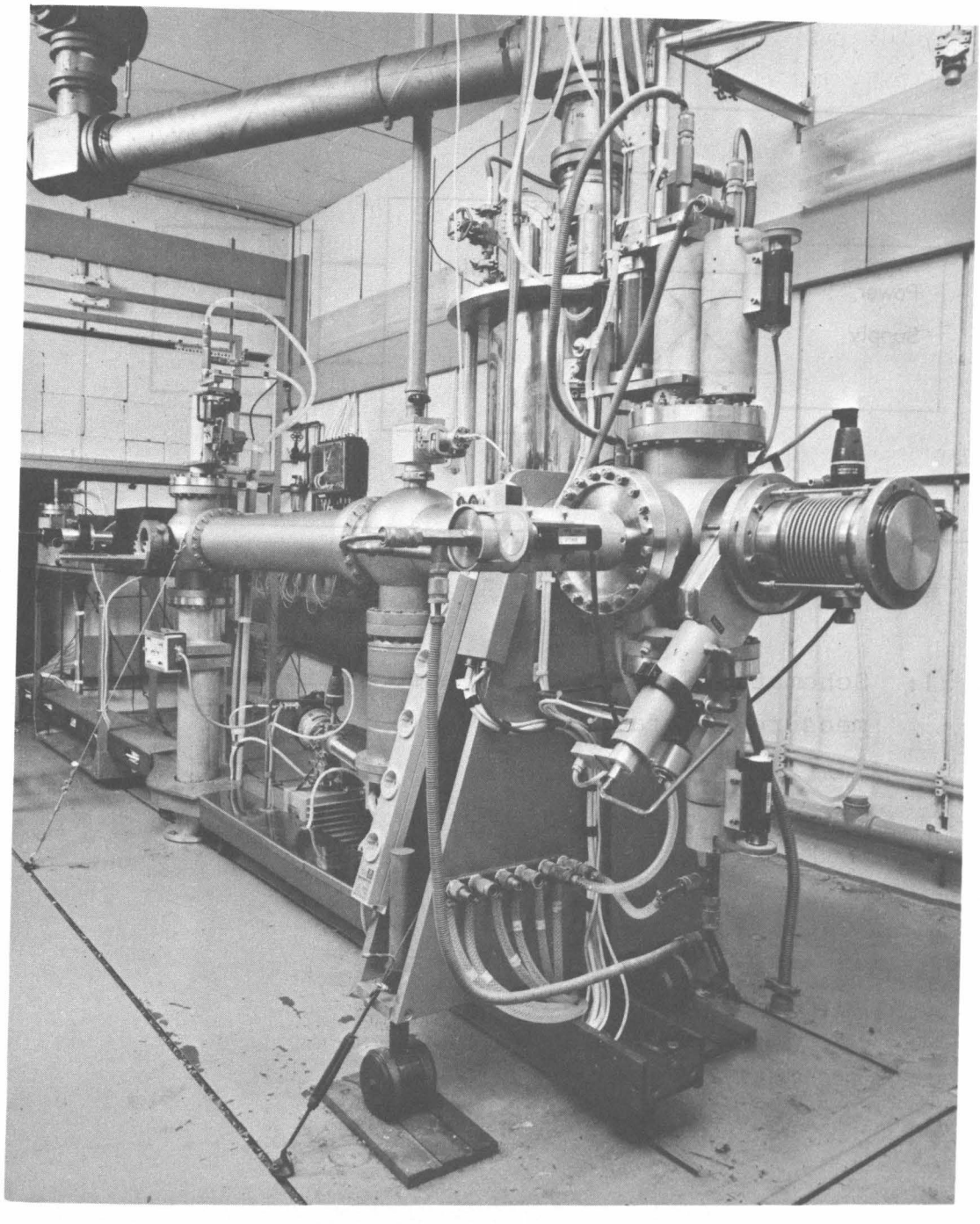

Fig. 20: A photograph of the beam line of the van de Graaff accelerator of the Institut für Festkörperforschung of the KFA Jülich , W. Germany.

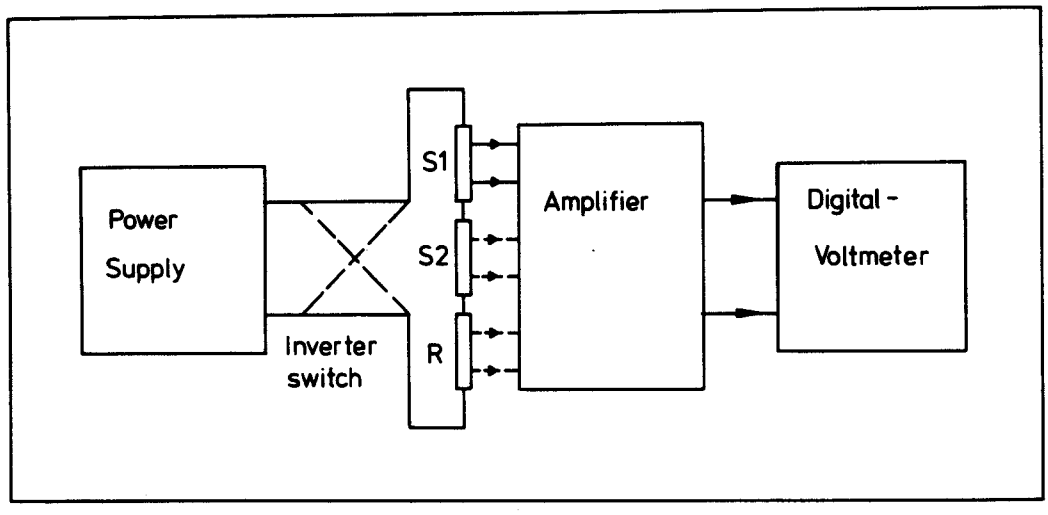


Fig. 21: Schematic diagram for the resistivity measurement facility.

# CHAPTER V

## V. Experimental results

### V.1 Directional dependence of damage production at 4.5 K

Fig. 22 shows the damage rate $\frac{\Delta\rho}{\Delta\phi}$ versus the resistivity induced by 1.81 MeV electrons in a (100)-specimen with <100>-axis. The different irradiation directions are identified by the different symbols. It is shown, that the damage rate $\frac{\Delta\rho}{\Delta\phi}$ decreases with increasing resistivity. Therefore the damage rates were normalized to the interpolated damage rate of the unrotated specimen (dashed line).

The rotation of the specimens by an angle $\tau$, causes an increase of the effective thickness of the specimen $\Delta d$:

$$\frac{d + \Delta d}{d} = \frac{1}{\cos \tau} \qquad (5.1.1)$$

The effect of this increase in thickness on the defect production rate is balanced in thin specimens /44/ by the decrease in beam density by a factor cos $\tau$. But the beam spreading will be increased by the increased effective thickness of the specimen which in turn results in an increase $\Delta s$ in the average pathlength of the electrons (see equation 2.2.5).

$$\frac{\Delta s}{d}(\tau) = \frac{(\bar{\alpha}^2)_{\tau=0}}{4 \cos \tau} \qquad (5.1.2)$$

Therefore the measured damage rate must be corrected by this factor. Fig. 23 shows the normalized damage rates $\frac{d\rho}{d\phi}$ versus the rotation angle, $\tau$, of the (100) <100> specimen and the (110) <100> specimen irradiated at 4.5 K with electrons of energy 1.81 MeV (specimen-holder I). Both specimens were irradiated simultaneously on one specimen-holder and rotated intermittently around their respective <100> axis. The damage rates are normalized to the damage rates of the unrotated specimen.

The damage rate measurements are done on specimens of all three crystallographical orientations (100), (110) and (111). The orientation and axis of the two specimens on one specimen holder were chosen in a way that lattice directions on one border of the orientation triangle of the cubic lattice were passed from opposite directions (fig. 24). By combining the results from both specimens it then was possible to eliminate empirically the effect of increased path length in a rotated specimen. It was further possible to minimize errors caused, for example, by misalignment of specimens. Fig. 25 shows damage rates at 4.5 K and energies of 1.41 and 1.81 MeV normalized to the value of the <110> direction.

## V.2 Directional dependence of damage production at 40 K and 400 K

The purpose of this work was, to compare the directional de-

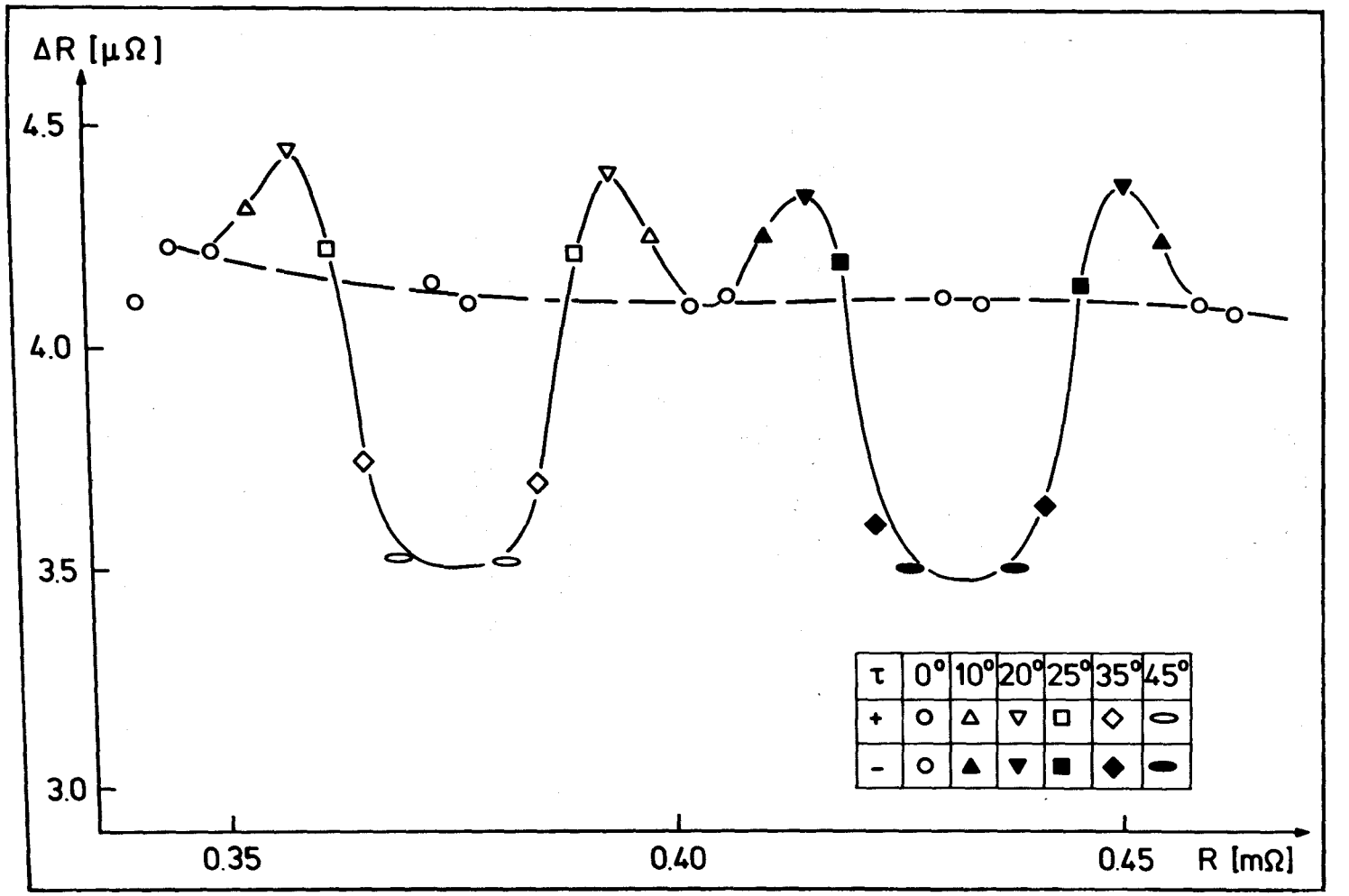


Fig. 22: A plot of the induced resistance change at 1.81 MeV versus the specimen resistance for the (100) <100>-platinum specimen at 4.5 K.

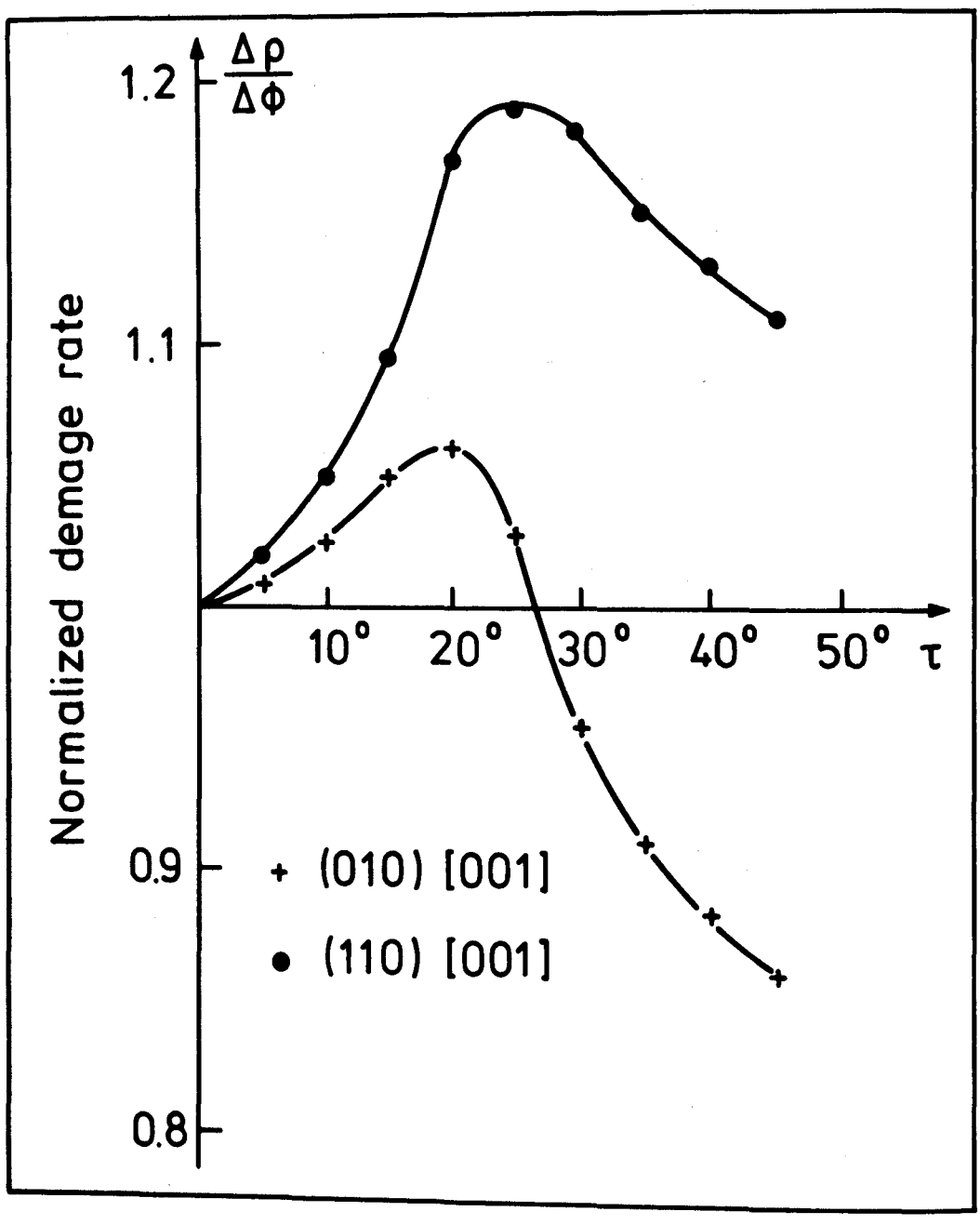


Fig. 23: Normalized damage rates versus the rotation angle τ of the (010) [001] and the (110) [001] specimens irradiated at 1.81 MeV and 4.5 K.

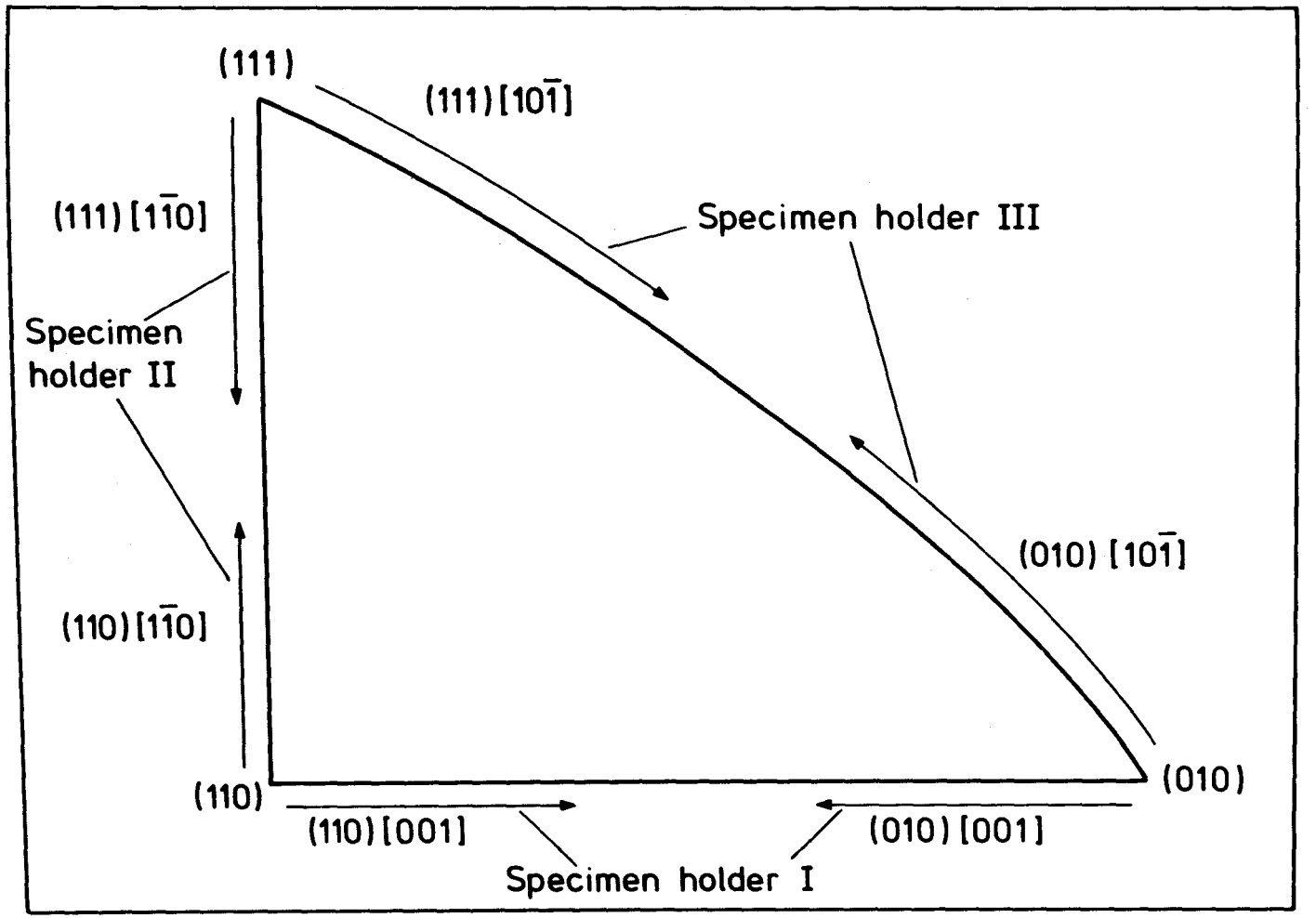


Fig. 24: Covering the lattice direction along the border of the fundamental triangle by rotating the specimens on the different specimen holders.

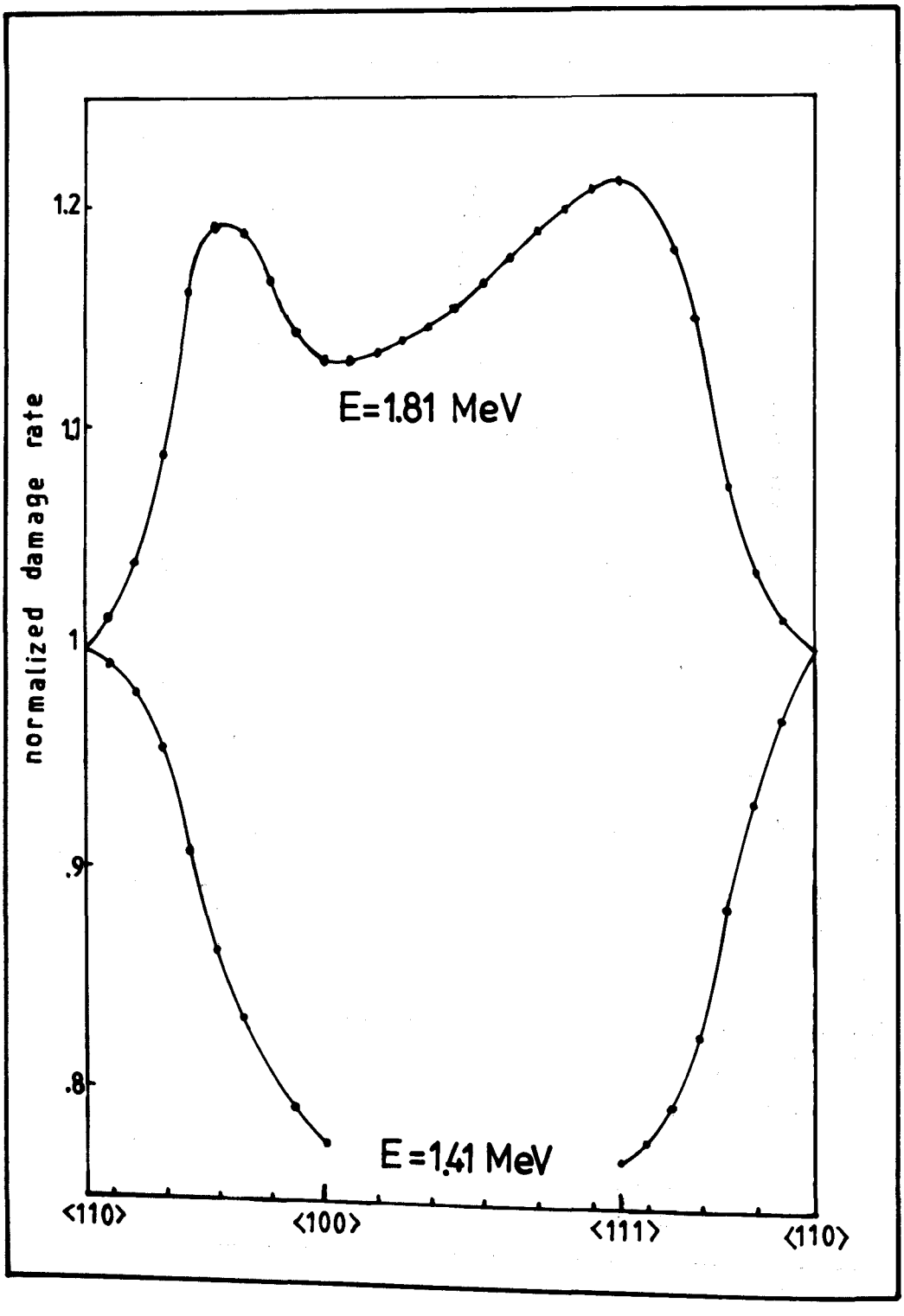


Fig. 25: Damage rates normalized to the value of the <110>-direction versus the lattice direction at 4.5 K.

pendence of the damage rate at different temperatures. As was already explained, the temperatures of 4.5 K, 40 K and 400 K were chosen to stay outside the main annealing stages. For the same reason precise control of the specimen temperature is important to avoid annealing of defects, especially during the warming up period after a resistivity measurement at 4.5 K. The variation of the specimen temperature during irradiation at 40 K and 400 K is shown in fig. 26 and 27 respectively. In the case of the 40 K - irradiation, the temperature is stable from the beginning till the end of irradiation. In the case of irradiation at 400 K large temperature gradients in the heat exchanger cause temperature drifts of about 5 K during the irradiation. Stabilisation periods of several hours before each irradiation would have been necessary to reduce these drifts.

On the other hand it was found that reproducible results were obtained, when the beam off-measurement-beam on cycle was done at a reproducible schedule. As is best seen in fig. 27, the beam was already turned on before the specimen had reached the nominal temperature. This was done to obtain a smooth transition with negligible overshooting. Resistivity measurements during irradiation at both temperatures showed that the temperature was raised by about 2 K by the beam of 10 $\mu A/cm^2$.

Fig. 28 shows the energy dependence of the damage rates for the main crystallographic directions at the three irradiation

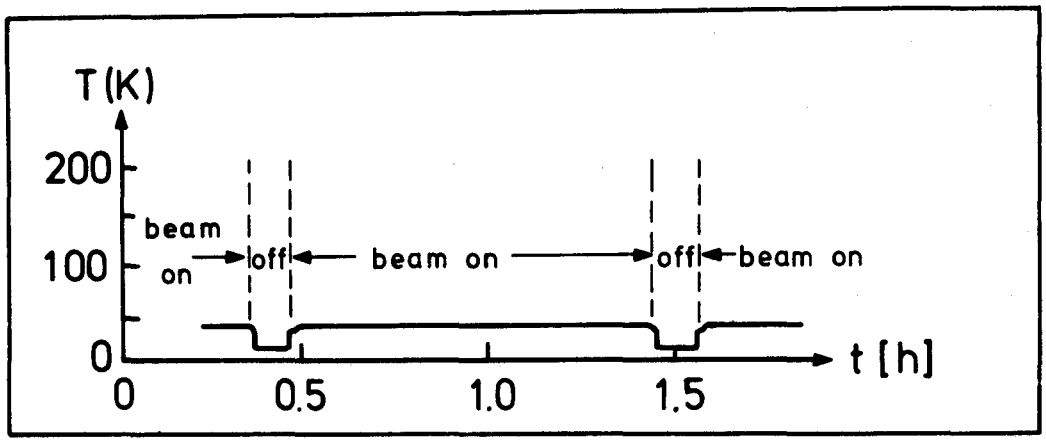


Fig. 26: The variation of the specimen temperature during measuring and irradiation at 40 K

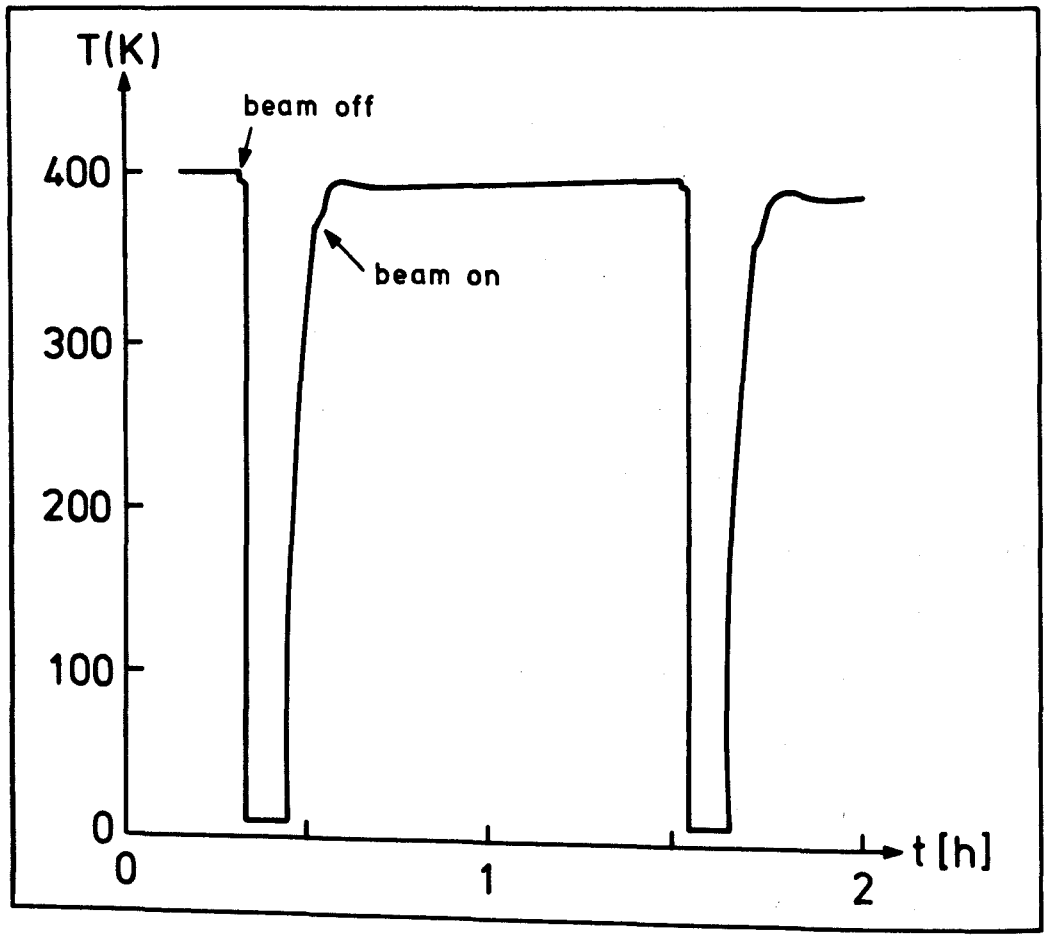


Fig. 27: The variation of the specimen temperature during measuring and irradiation at 400 K.

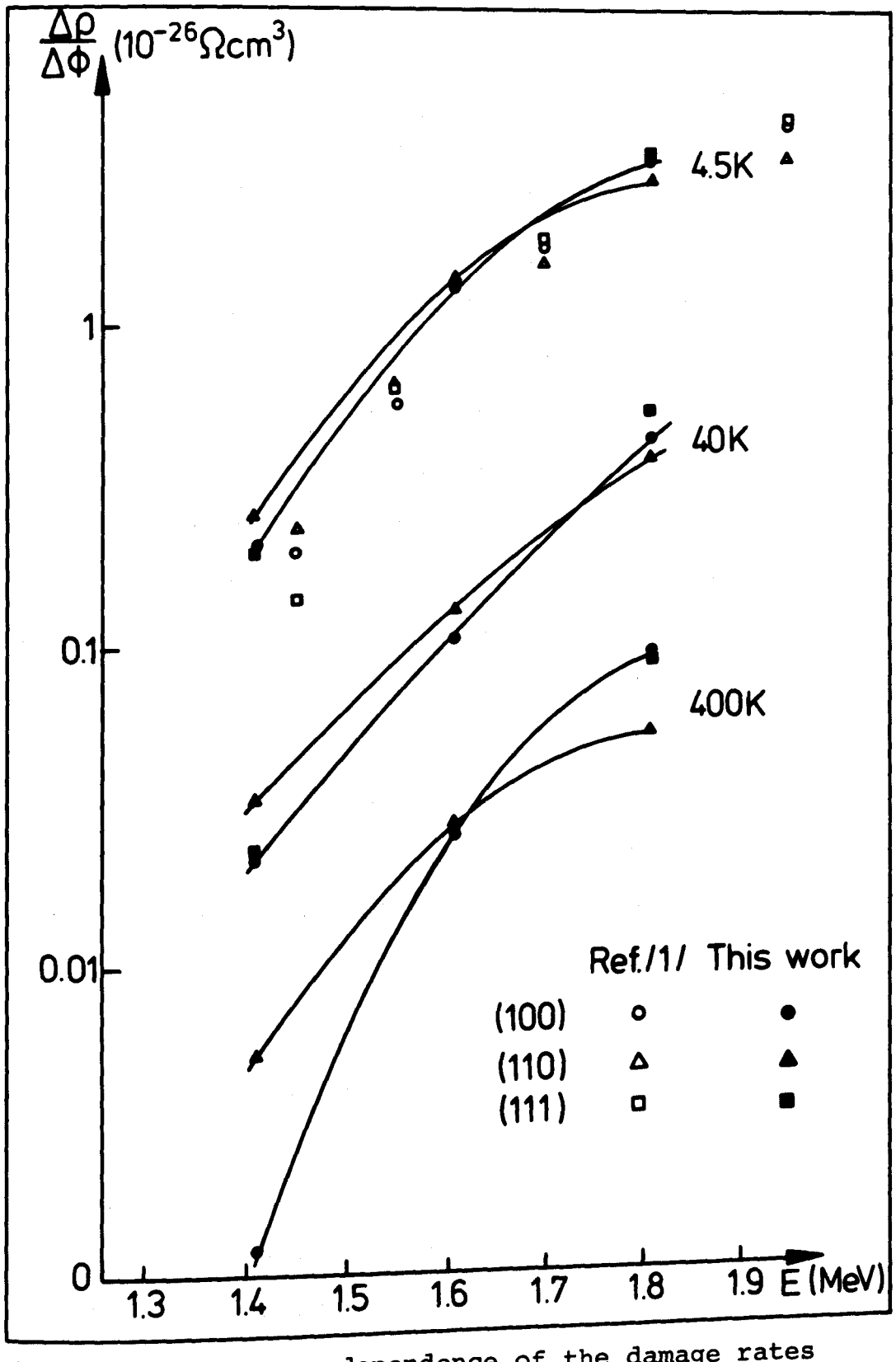


Fig. 28: The energy dependence of the damage rates for the mean crystallographical directions at various irradiation temperatures.

temperatures. Notwithstanding a rather large scattering of the absolute 400 K - data, especially at the lowest energy, it is safe to say, that at all temperatures the <110> direction shows the highest damage rates at low energies. That means the minimum threshold energy corresponds to this direction. On the other hand a temperature dependence of the (extrapolated) minimum threshold energy could not be determined unambiguously, due to the above mentioned errors at low energies, especially at 400 K. For the moment suffice it to say, that the 4.5 K - data are in agreement with a minimum threshold energy value around 34 eV as derived from polycrystalline data /26/, while at 400 K this value may be slightly lower. Also included are data from a previous work at 4.5 K /1/. The small shift in energy ($\sim$ 0.03 MeV) between both sets of data is within the error of the energy calibration of the van de Graaff (see section IV.2) and the error in the calculation of the energy loss in the apparatus (see section II.1).

In Fig. 29 the normalized damage rates for irradiations along lattice direction on the border of the orientation triangle at the different temperatures are shown. The value of the damage rate is normalized to the value of the <110> direction. At 1.81 MeV for all temperatures maximum damage rates were found at or close to the <100> and <111> directions, while at 1.41 MeV these directions always showed minimum values. The height of

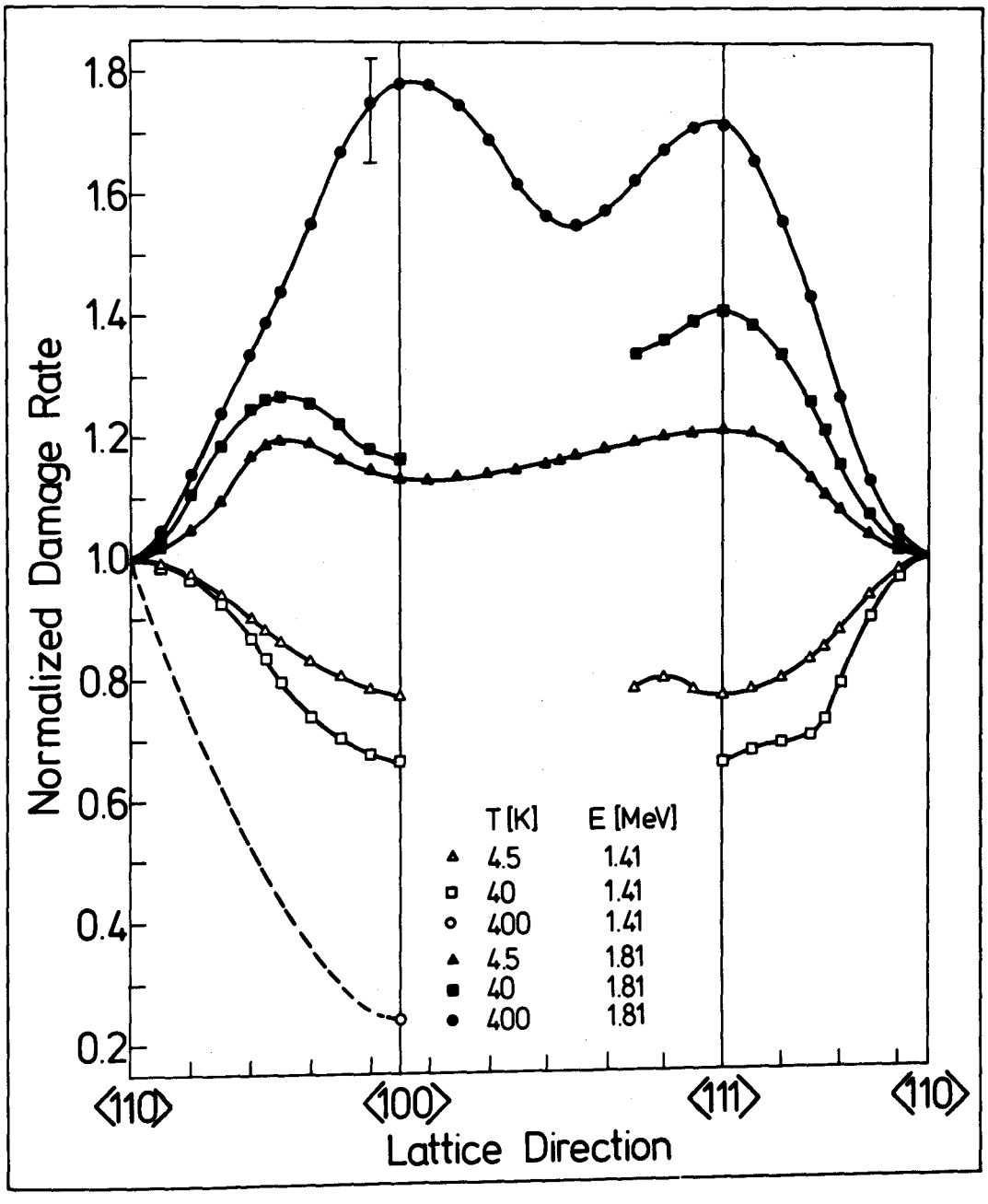


Fig. 29: Damage rates normalized to <110> in platinum as a function of the crystal orientation, at various electron energies and irradiation temperatures.

these minima or maxima increases with increasing temperature. That means the damage production becomes more anisotropic at higher temperatures.

## V.3 Error analysis

Possible errors of the measured damage rate may be caused by

a) Errors in the resistivity measurements, for example by fluctuating thermo voltages across the specimen, by instabilities of the voltage amplifier or by the limited resolution of the digital voltmeter (see section IV.2). The sensitivity of the present device is about $1.0 \times 10^{-8}$ Volt. For the 4.5 K irradiation, the resistivity measurements were done in liquid helium. In this case a measuring current of 1 A was used, giving a resolution of 10 nΩ. At the higher irradiation temperatures when the resistivity measurements were done in the condensed helium in the measuring chamber a lower current of 0.2 A was used to avoid evaporation of the helium. In this case the resolution was about 50 nΩ.

This resolution is about 0.3 % and 4 % of the resistance accumulated during the respective irradiation periods at 4.5 K and 400 K.

b) The error in the measurement of the absolute intensity of the electron beam is about 10 %. Long term fluctuation and

inhomogeneities of the beam across the specimens are about 3%.
c) The error caused by misalignment of the plains or axes of the specimens are estimated from Laue patterns of the mounted specimens. Laue patterns are taken at three different positions of the specimens with respect to the X-ray beam. The first is taken at an incidence normal to the specimen holder to check the alignment of the specimen's plane. The second and third is taken after rotating the specimen to the next main planes (left and right direction). From these Laue patterns errors in the axis can be estimated. From these tests the best specimens are selected for irradiation. The errors in specimen orientation and the error in the measurement of the rotation angle add up to about $3^{o}$, while relative rotation angles are measured to an accuracy of about $0.5^{o}$.
d) In the case of the 400 K irradiation temperature drifts up to 5 K may cause errors due to annealing. The reproduceability of measurements in the unrotated position indicates that these errors are below 10 %.

The effective absolute error of the measured damage rate is about 10 % mainly due to errors in the beam current density. Above 4.5 K larger errors arise due to differences in the simultaneous annealing due to different damage structures and impurity levels. These errors do not include the errors

which may arise from an incorrect calibration of the accelerator energy. For example an error in this energy of 0.02 MeV would change the damage rate at 1.4 MeV by about 30 % and at 1.8 MeV by about 6 %.

Since relative damage rates rather than absolute rates were used almost exclusively in evaluating the data, these errors have little influence on the calculated threshold energy profile.

The relative errors increase with the distance from the <110> direction. For the damage rates along the <100> and <111> directions typical errors relative to the <110> value are 5 %.

Somewhat larger relative errors must be ascribed to the data for directions between <100> and <111> because here the errors relative to the <100> or <111> directions and the errors of these directions relative to <110> must be added.

# CHAPTER VI

## VI. Determination of the threshold energy profile

In this section the measured displacement rates will be explained in terms of an anisotropic threshold energy. This will be done by comparing displacement rates calculated from an assumed threshold energy profile to the measured data. For these calculations an averaged differential cross section must be used to include the spreading of the electron beam.

### VI.1 The averaged differential cross section of a spreaded electron beam

Fig. 30 shows the Gaussian distribution of the electrons, which is calculated (see section II.2) for electrons of energies 1.46 MeV and 1.86 MeV after having passed through the stainless steel window (thickness 12.5 μm), 2 mm of liquid helium and half the thickness (5 μm) of a 10 μm platinum specimen. The electron energies are then degraded to 1.41 and 1.81 MeV, respectively. The Gaussian width is calculated from the equations 2.2.2 and 2.2.3 as 20.2 and 16.3 degrees for the 1.41 MeV and 1.81 MeV electrons, respectively. The integral over the solid angle of the curves in fig. 30 is normalized to unity.

For calculating the displacement cross section the McKinley-Feshbach differential cross section (2.2.3) including the correction factors given by Oen /17/ were used, as given by the solid lines in fig. 31. The cut offs at angles of about 18 and

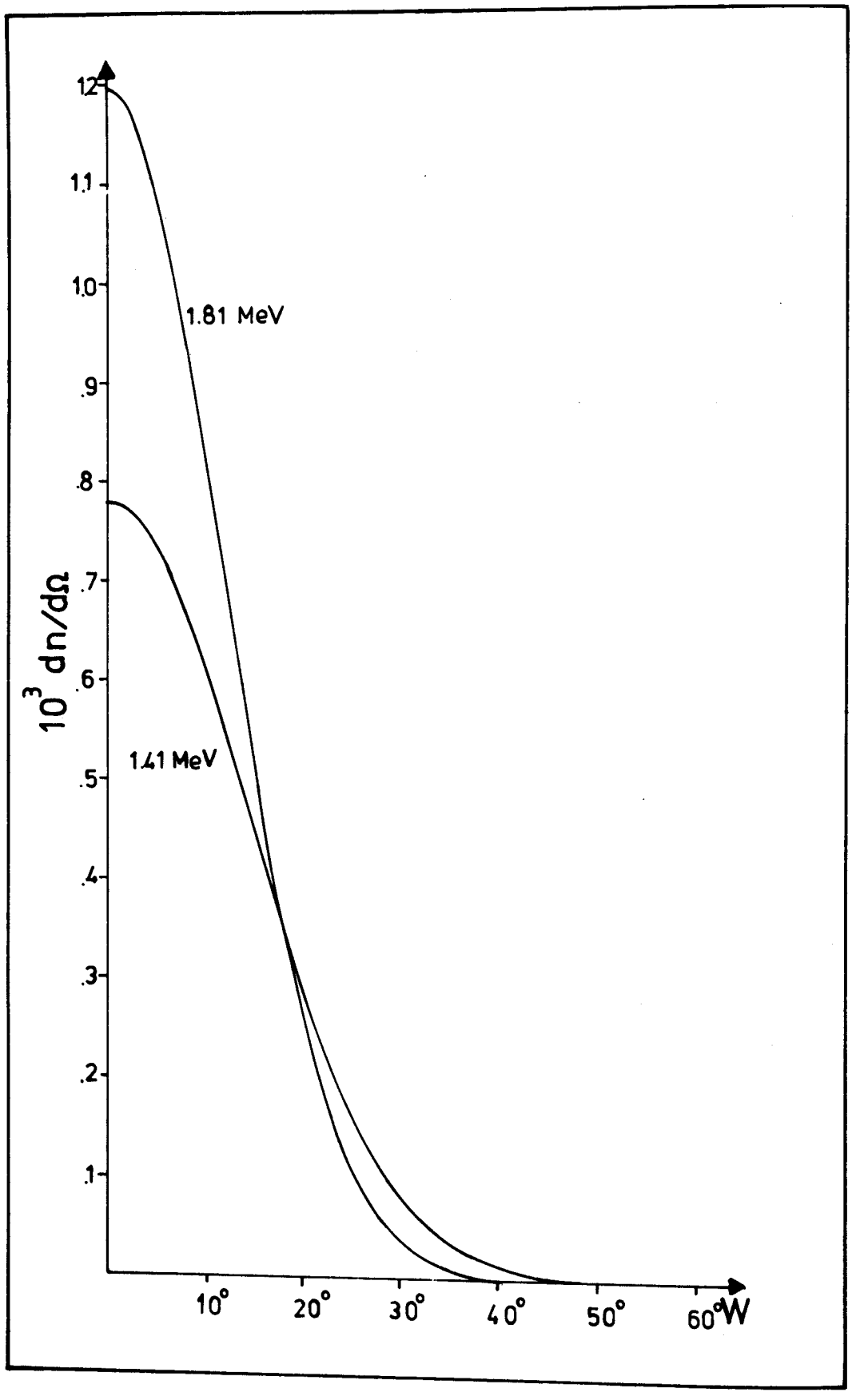


Fig. 30: The angular distribution of the irradiation electrons.

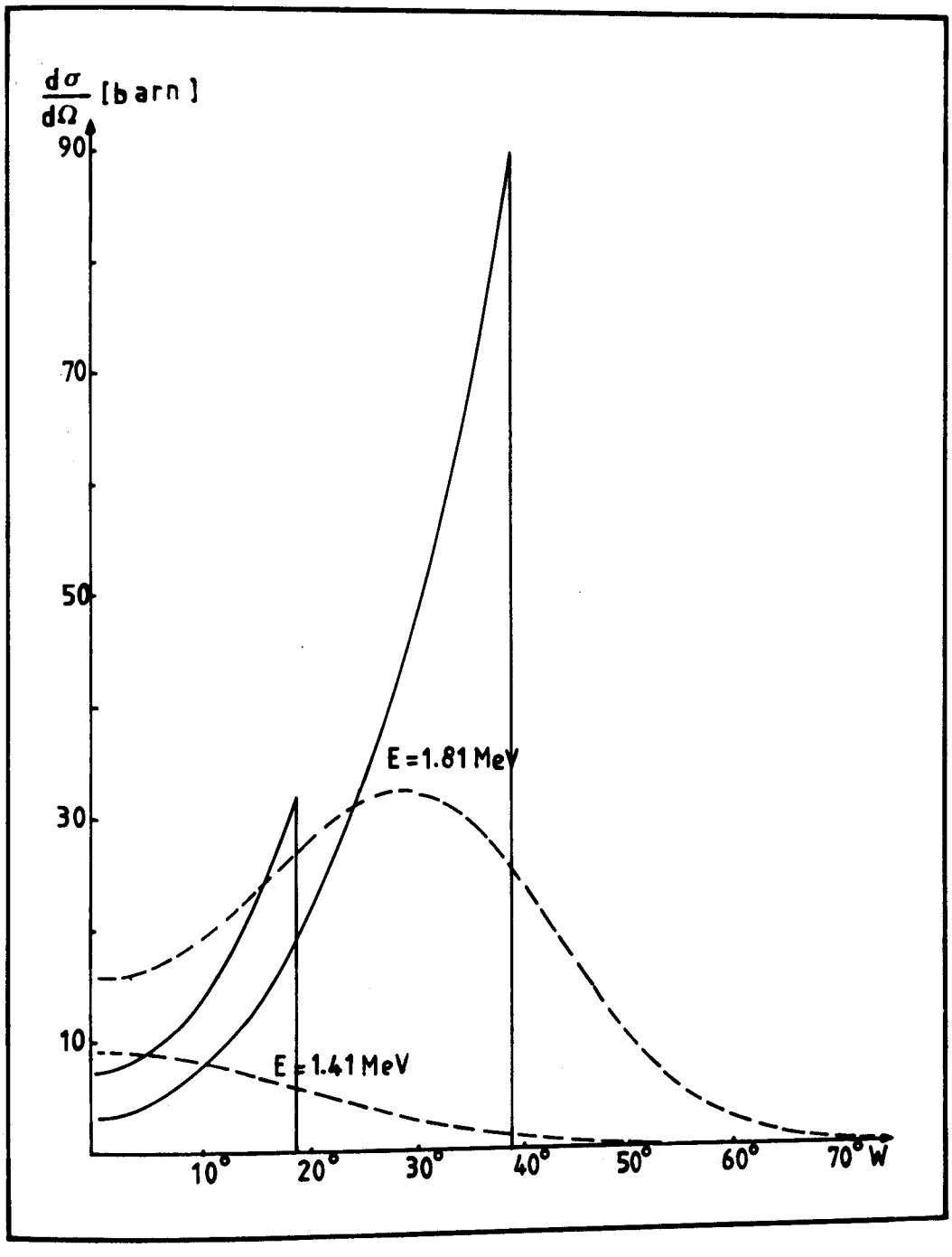


Fig. 31: Differential cross section for irradiation of platinum with electrons of different energies. The solid lines correspond to an unidirectional beam, the dashed line to the beam after traversing the irradiation window, cooling helium and 5 µm of platinum.

38 degrees, respectively, correspond to a uniform threshold energy of 34 eV. A higher threshold energy, for example, would give cut offs at smaller angles. The calculation of the displacement cross section including beam spreading was done on the computer. The program for this calculation is given in Appendix A. In this program the differential cross section for a certain threshold energy was folded by the Gaussian distribution of the spreaded beam to obtain the averaged differential cross section for the spreaded beam.

The calculations was done for threshold energies between the minimum threshold (in the case of platinum $T_d$ = 34 eV) and the maximum transferred energy (38 eV for 1.41 MeV and 57 eV for 1.81 MeV) in steps of 2 eV. The averaged differential cross sections are shown by the broken lines in fig. 31. It can be seen, that at 1.41 MeV the angular dependence of the averaged cross section is dominated by beam spreading while at the higher energy the influence of the scattering cross section prevails.

## VI.2 The fitting procedure

For calculating the defect production rate, the relation between the differential cross section and the defect production rate must be known. When an electron of energy E, incident along a lattice direction $(\theta_o, \phi_o)$, knocks an atom into a direction

$(\theta,\phi)$, the damage rate is given by:

$$\frac{\Delta\rho}{\Delta\phi}(E,\theta_o,\phi_o) = \rho_F \int_o^{2\pi} \frac{d\sigma}{d\Omega}(E,W)\, P(T,\theta,\phi)\, d\Omega \qquad (6.1.1)$$

The recoil angle W is given by:

$$\cos W = \cos\theta \cos\theta_o \cos(\phi-\phi_o) + \sin\theta \sin\theta_o \qquad (6.1.2)$$

The displacement probability $P(T,\theta,\phi)$ is given by

$$P(T,\theta,\phi) = \begin{cases} 0 & \text{for } T(E,W) < T_d(\theta,\phi) \\ 1 & \text{for } T(E,W) \geq T_d(\theta,\phi) \end{cases} \qquad (6.1.3)$$

The transferred energy $T(E,W)$ is given by the equation (2.3.1) and (2.3.2) and $T_d(\theta,\phi)$ represents the (unknown) anisotropic threshold energy profile.

For the integration of equation (6.1.1) it is useful to introduce a new coordinate system $(\theta',\phi')$ with the irradiation direction $(\theta_o,\phi_o)$ through the origin. This is obtained by two rotations of the original coordinate system as shown in fig. 32:

a) The system $(\theta,\phi)$ is rotated around the Z-coordinate by an angle $\phi_o$.

b) and subsequently rotated around the new Y-coordinate by an angle $\theta_o$.

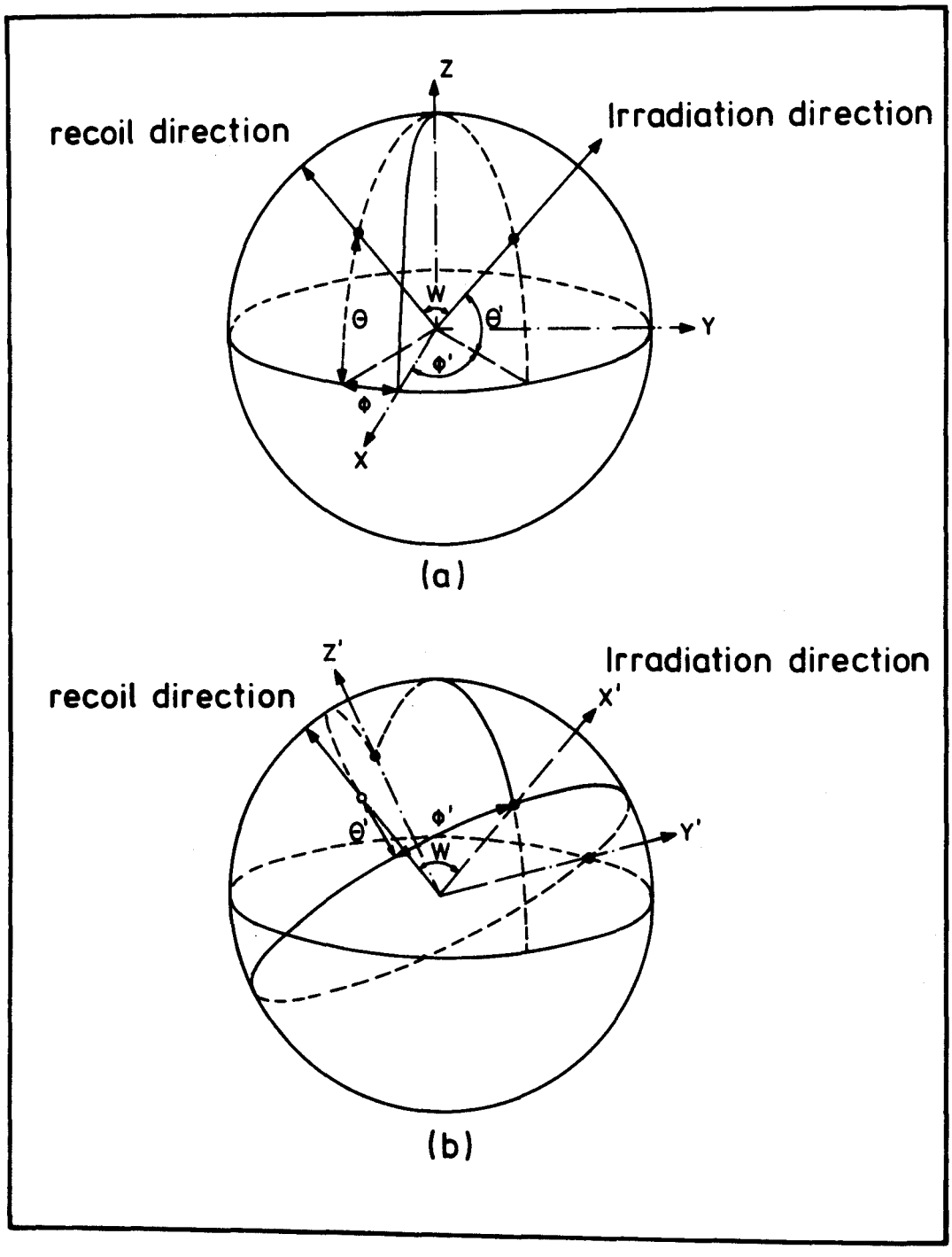


Fig. 32: Schematic representation of the co-ordinate systems.
a - before the rotations
b - after the rotations

The recoil direction $(\theta, \phi)$ is then described by

$$\sin \theta = \cos \theta' \cos \phi' \sin \theta_o + \sin \theta' \cos \theta_o \qquad (6.1.4)$$

and

$$\sin \phi = \frac{\cos\theta'\cos\phi'\sin\phi_o\cos\theta_o+\cos\theta'\sin\phi'\cos\phi_o-\sin\theta'\sin\theta_o\sin\phi_o}{\sqrt{1 - \sin^2 \theta}} \qquad (6.1.5)$$

The recoil angle is now given by:

$$\cos W = \cos \theta' \cos \phi' \qquad (6.1.6)$$

and the element of the solid angle is:

$$d\Omega = \cos \theta' d \theta' d \phi' \qquad (6.1.7)$$

Multiple displacement was not considered in equation (6.1.1) because even for the highest energy used (1.81 MeV), the maximum transferred energy ($\sim$ 57 eV) was less than twice the minimum threshold energy.

The calculation of the displacement rates was done by a computer program given in Appendix B. The integration over the solid angle was done in steps of $5^o$. Also the threshold energy profile used constant values in $5^o x 5^o$ areas as shown in fig. 33. For an assumed threshold energy profile, the defect production rates were calculated and compared to the measured damage rates.

The threshold energy profile was changed until the calculated values of the displacement rate reasonably fitted the measured damage rates. The quality of the fit was determined by calculating the standard deviation. The resistivity per unit concentration

$\rho_f$ was determined by comparing the calculated cross section for the <110> direction with the respective damage rate of the 4.5 K irradiation.

According to the limited number of experimental data, a rather simple threshold energy profile was used which consisted of three zones around the main crystal directions. The size and the threshold energy value in these zones could be changed independently to obtain a good fit of the experimental data.

By using the above computer program, the measurements at 4.5 K 40 K and 400 K were best fitted by the threshold energy profiles given in fig. 34. It is found, that the optimal threshold energies in the three zones are independent of temperature:

| | | |
|---|---|---|
| Zone 1 | around <110> | $T_d(1) = 34$ eV |
| Zone 2 | around <100> | $T_d(2) = 36$ eV |
| Zone 3 | in between | $T_d(3) \geq 57$ eV |

The maximum $T_d$ value which can be derived from these experiments is 57 eV corresponding to the maximum transferred energy for the highest energy used (1.81 MeV). Especially the fit of the 400 K data is rather sensitiv to the $T_d$ value in zone 3. It was found that reasonable fits were possible for $T_d(3) > 50$ eV with an increase in the quality of the fit at higher values.

The temperature only influences the size of the zones. This influence is most pronounced for zone 2. Increasing tempera-

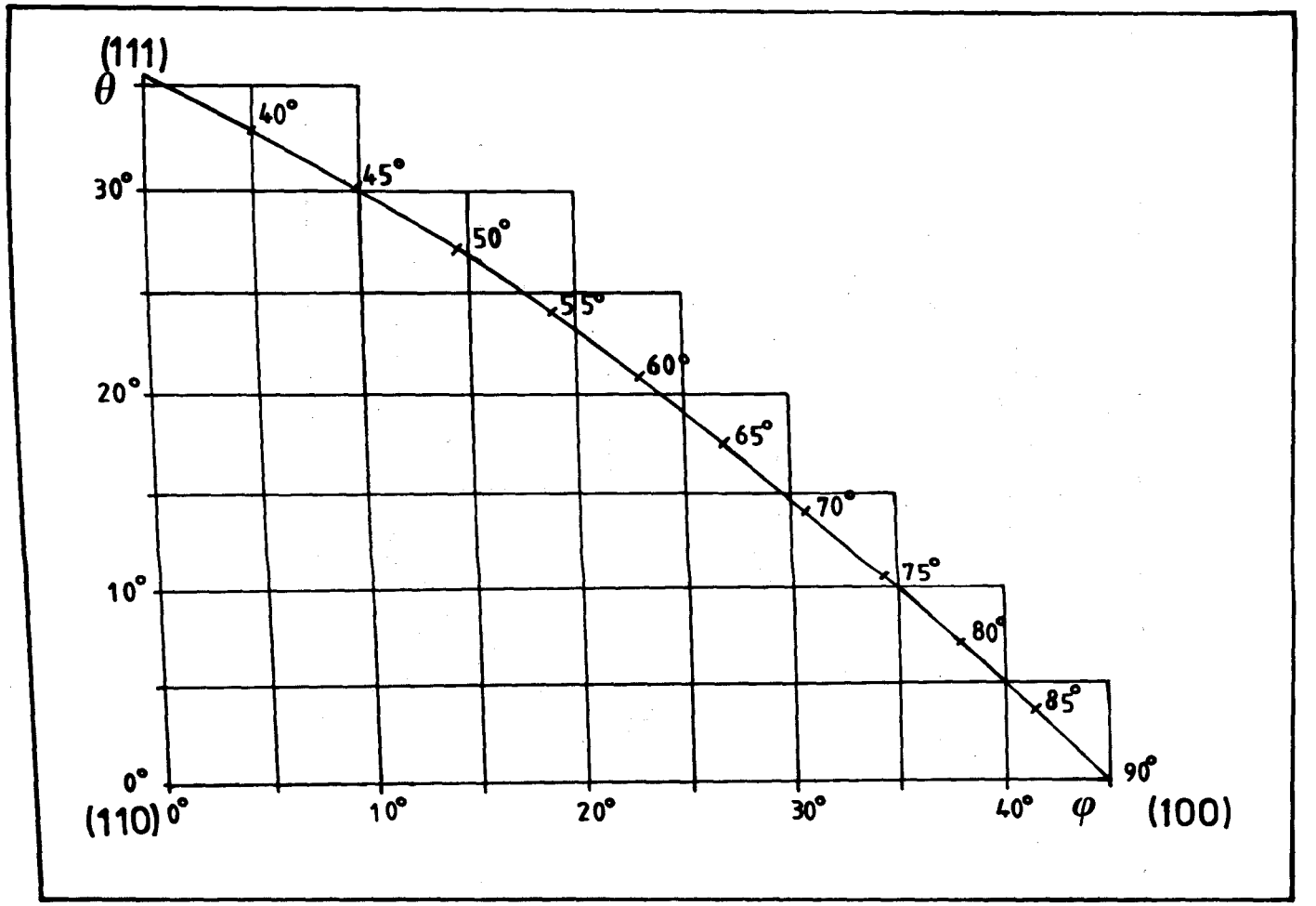


Fig. 33: The threshold energy profile subdivided in areas of $5^{o}x5^{o}$.

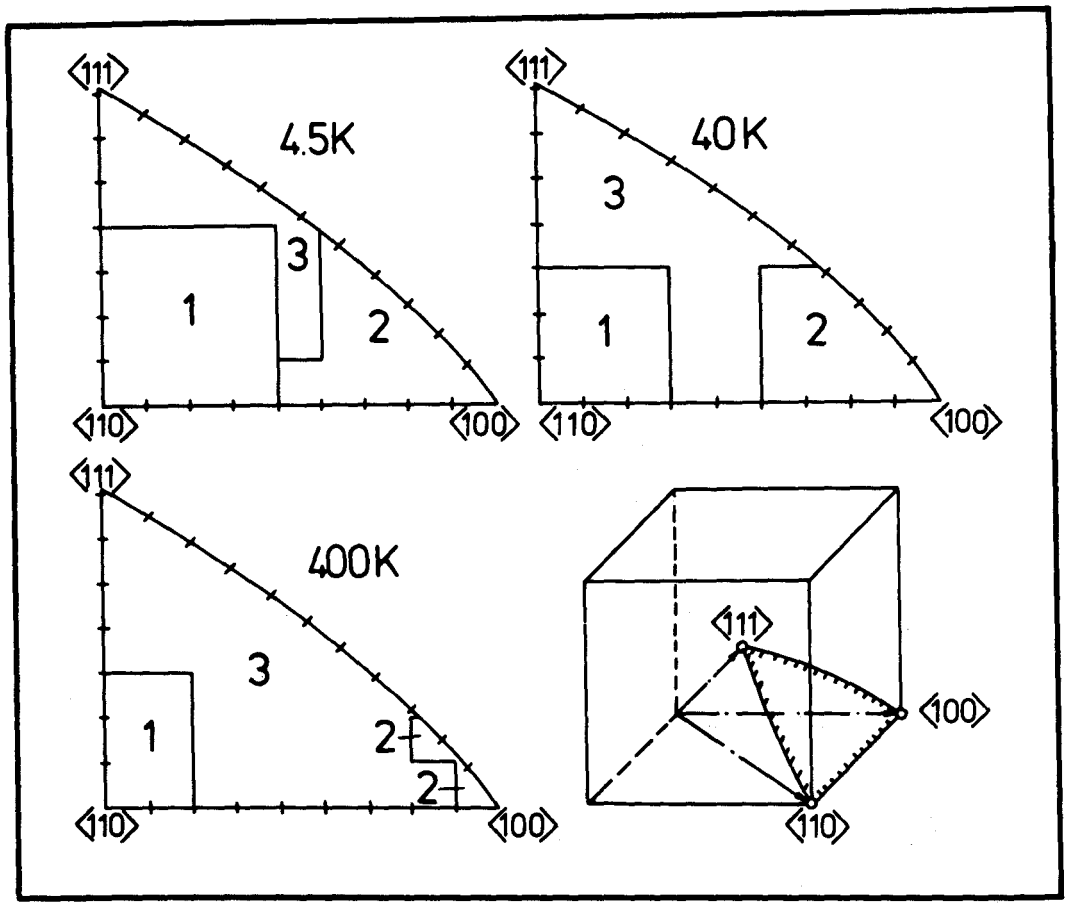


Fig. 34: The optimal threshold energy profiles at various irradiation temperatures.

ture decreases the areasof zones 1 and 2, and increases the area of zone 3.

The resistivity per unit concentration of defects $\rho_f$ was used as an independent parameter in the evaluation of the 4.5 K data (see above), while it was eliminated for the high temperature data by using only normalized data in the fit. Absolute defect production rates at elevated temperatures cannot be measured because an unknown number of defects are lost by recombination and trapping processes. If data from both energies of the 4.5 K irradiations (1.41 and 1.81 MeV) are evaluated seperately the respective $\rho_f$ values are 7.3 $10^{-4}$ Ωcm/u.c. and 9.6 $10^{-4}$ Ωcm/u.c.. The 1.81 MeV - value is in good agreement with the value given by Jung /1,26/. The lower $\rho_f$ value at 1.41 MeV is probably caused by a strongly reduced damage rate on the back side of the specimen at this energy, or by an error in the energy calibration (see above).

## VI.3 Influence of details of the threshold energy profile on the defect production rate

Fig. 35 compares the calculated defect production rates for three different profiles to the data points of the 4.5 K irradiation:

1) the profile of fig. 34 for 4.5 K with the threshold data as given above (solid line).

2) the same profile without the window around <110> (that means $T_d(1) \geq 57$ eV) (broken line).
3) the same profile without the window around <100> (that means $T_d(2) \geq 57$ eV) (dash pointed line).

The $\rho_f$ values were always adjusted to fit the <110>-value at 1.81 MeV. In this case, the calculations overestimate the defect production at 1.41 MeV. As mentioned above this can be explained by an inhomogeneous damage at this low energy or by errors in the energy calibration. Therefore this profile (1) is considered to be a reasonable fit as it describes the directional dependence quite well for both energies. Fig. 36 and 37 shows corresponding results for 40 K and 400 K-data by using the corresponding profiles. For these temperatures the calculations were also adjusted to fit the <110>-value of the 1.81 MeV-data. It is seen at all three temperatures that zone 1 alone already gives a fair approximation of the data, while zone 2 alone is far off a reasonable fit.

Fig. 38-40 show calculated displacement rates obtained by changing the sizes of zones 1 and 2 of the optimum profiles for 4.5 K, 40 K and 400 K (compare fig. 34). The change consisted in extending or reducing the border of the zones by $5^o$. The influence of this change is larger for the higher temperatures, with their smaller zones, than in the case of 4.5 K.

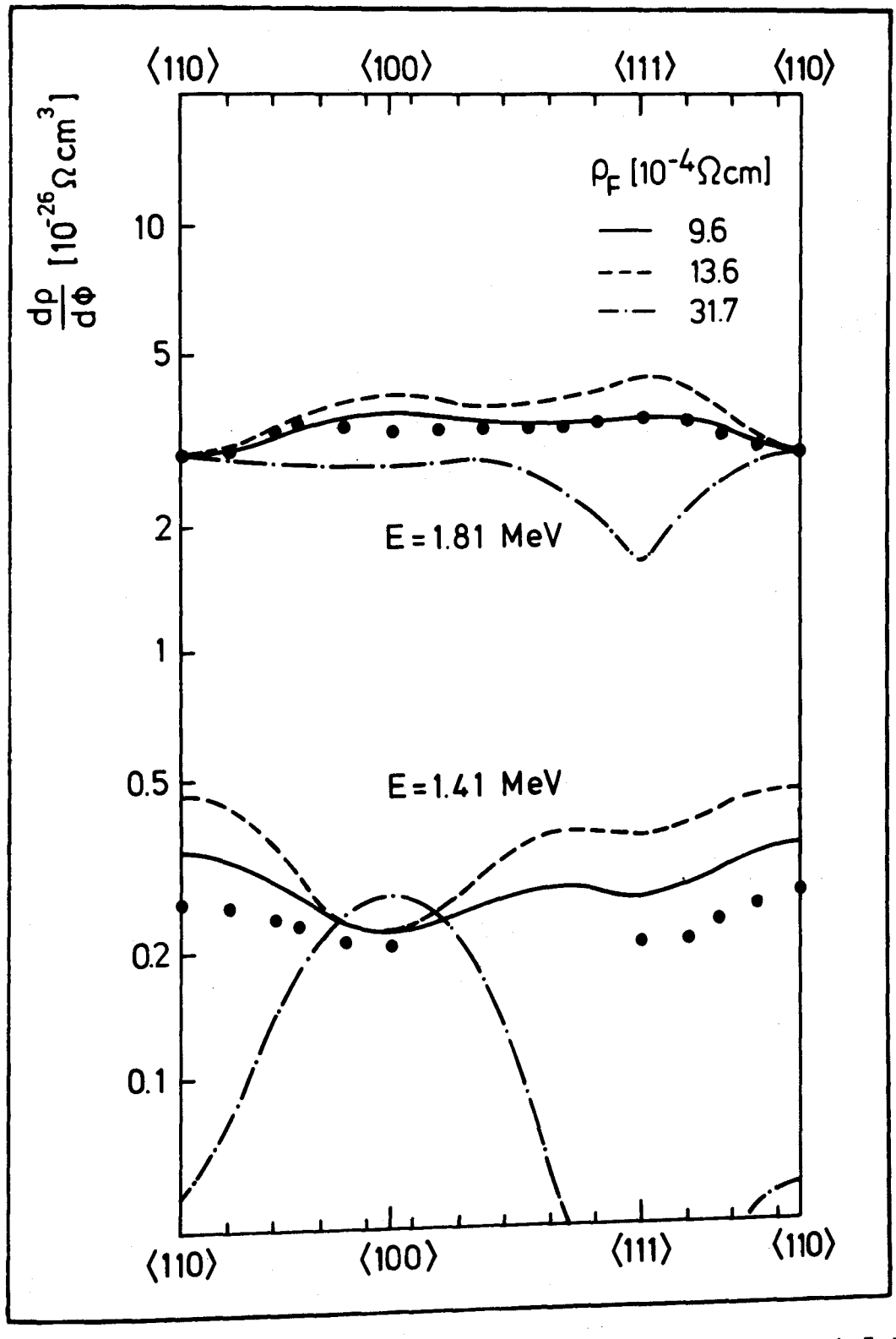


Fig. 35: Comparison of the measured damage rates at 4.5 K (●) to calculated damage rates for the threshold energy profile of Fig. 34 (—), and for this profile with omitting the windows around <110> (--) and <100> (-·-), respectively.

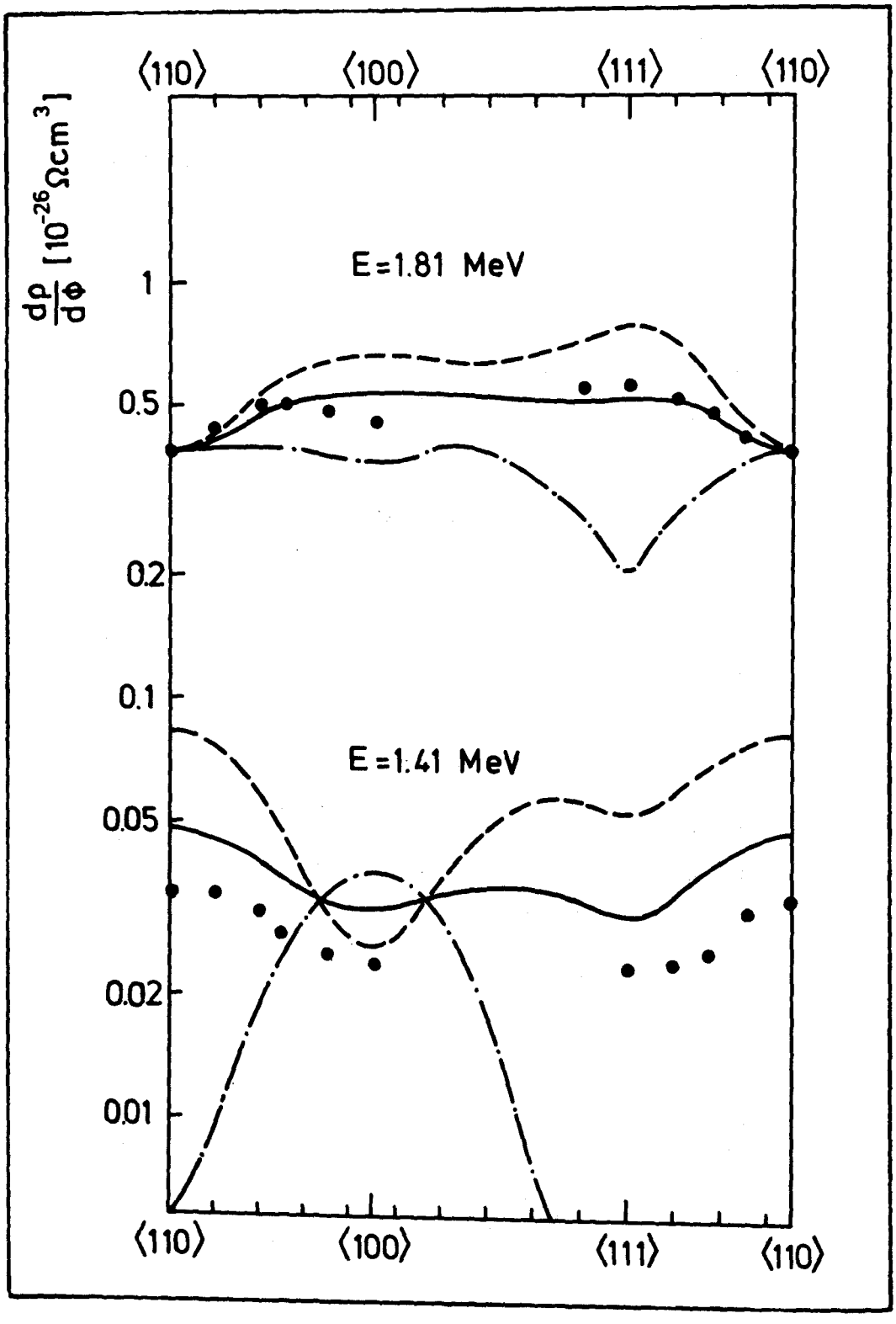


Fig. 36: Comparison of the measured damage rates at 40 K (●) to calculated damage rates for the threshold energy profile of Fig. 34 (—), and for this profile with omitting the windows around <110> (--) and <100> (-·-), respectively.

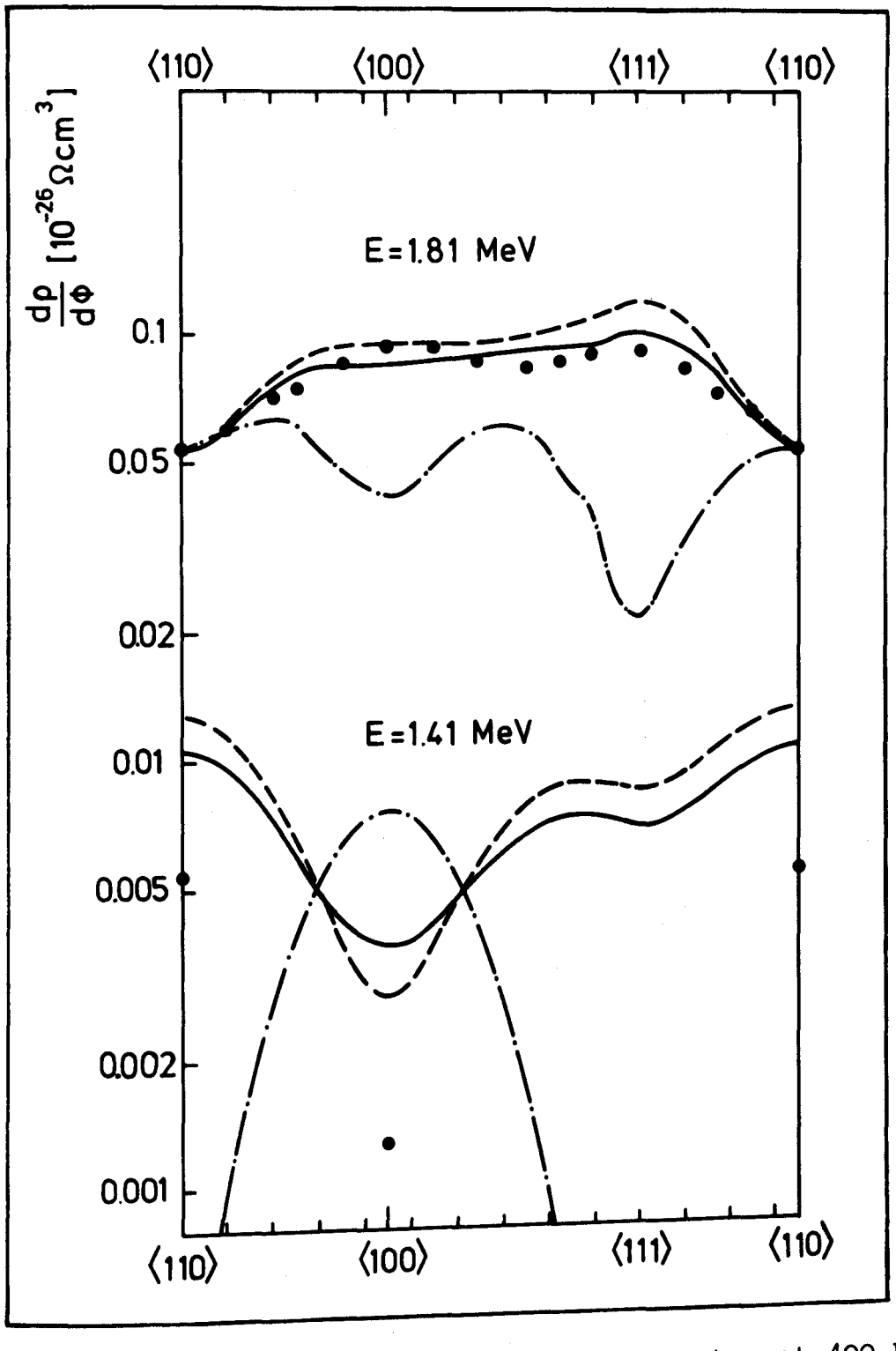


Fig. 37: Comparison of the measured damage rates at 400 K (•) to calculated damage rates for the threshold energy profile of Fig. 34 (—), and for this profile with omitting the windows around <110> (--) and <100> (-.-), respectively.

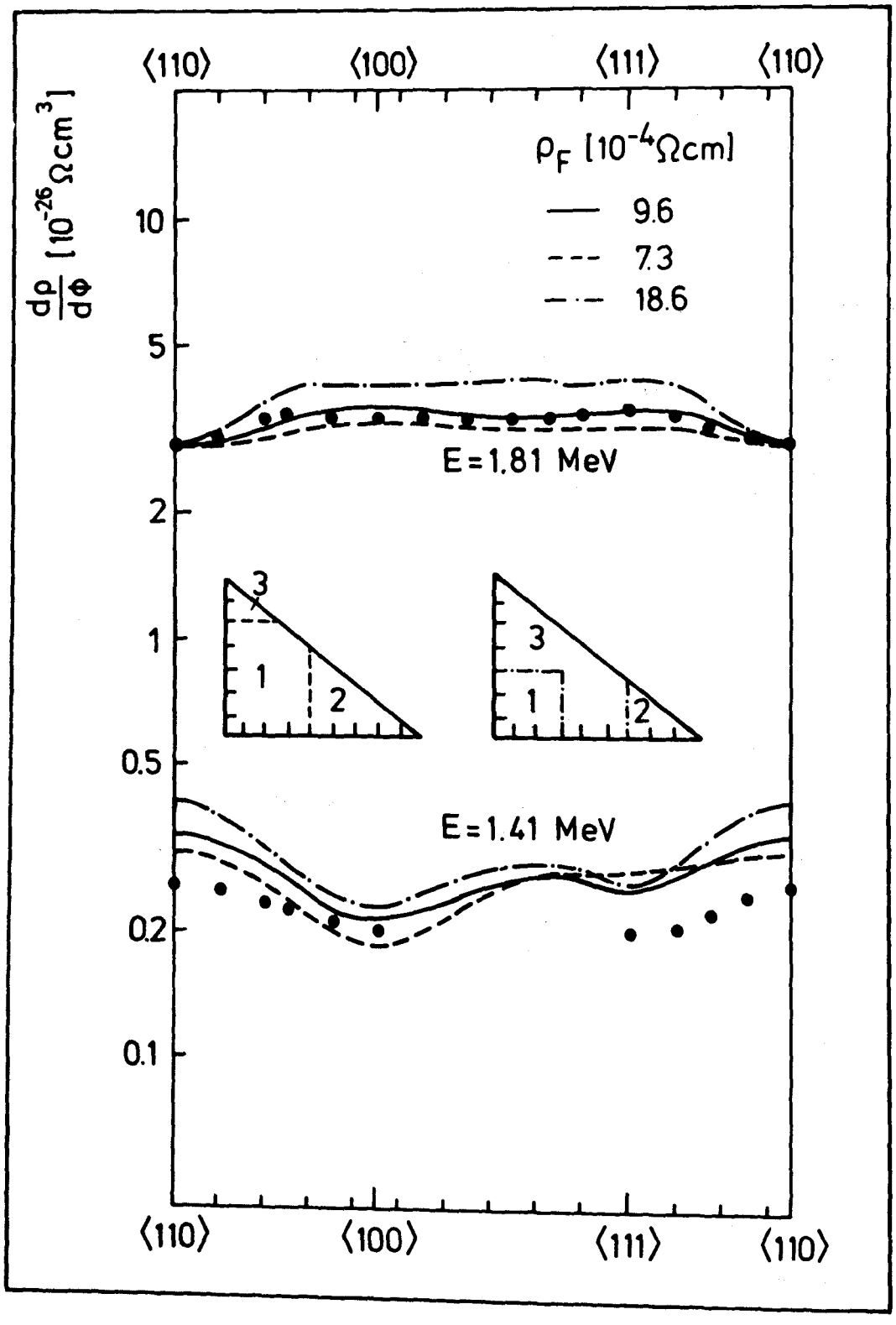


Fig. 38: The effect of the sizes of zones 1 and 2 of the optimal threshold energy profile on the calculated damage rates at 4.5 K.

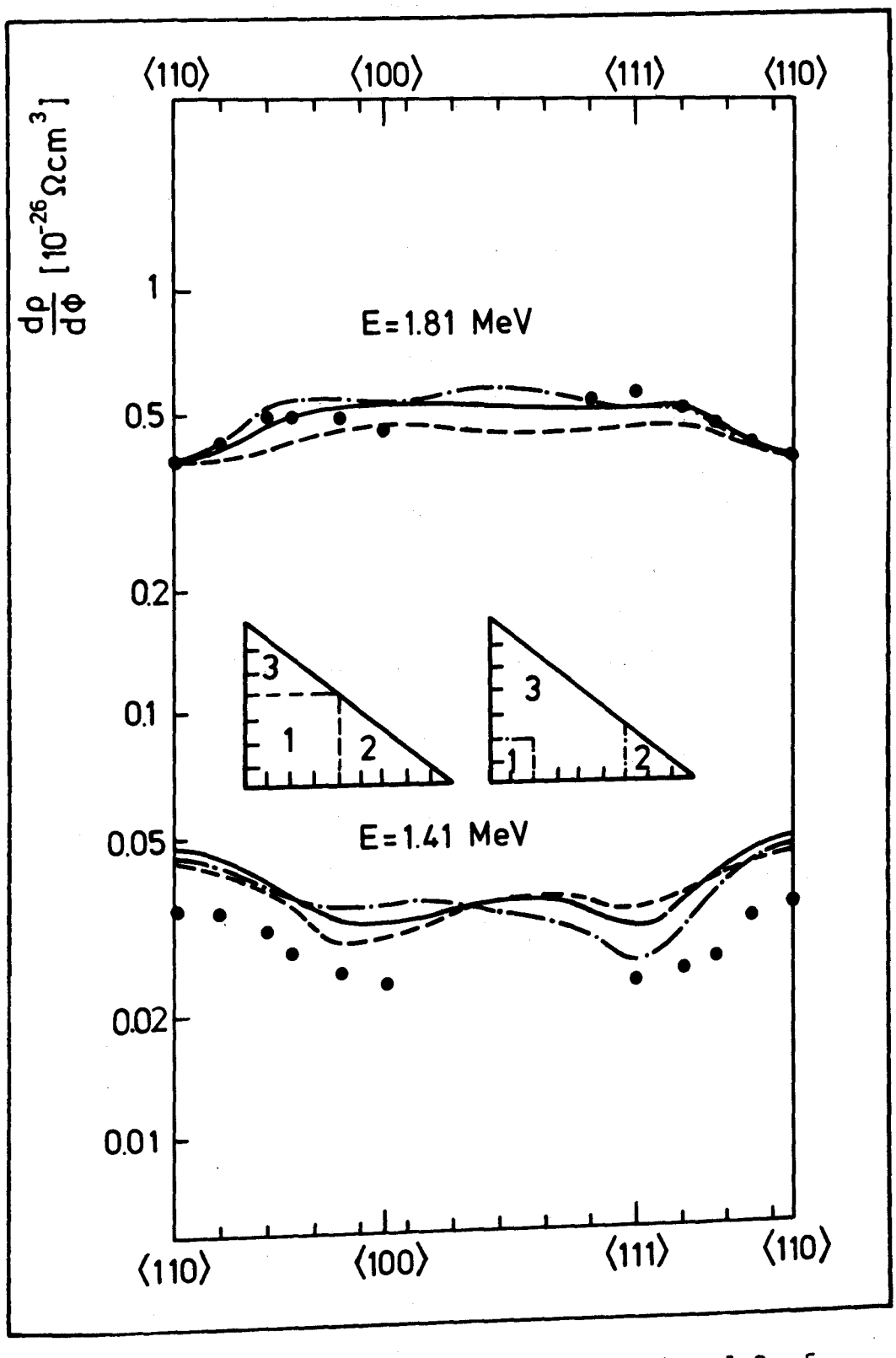


Fig. 39: The effect of the sizes of zones 1 and 2 of the optimal threshold energy profile on the calculated damage rates at 40 K.

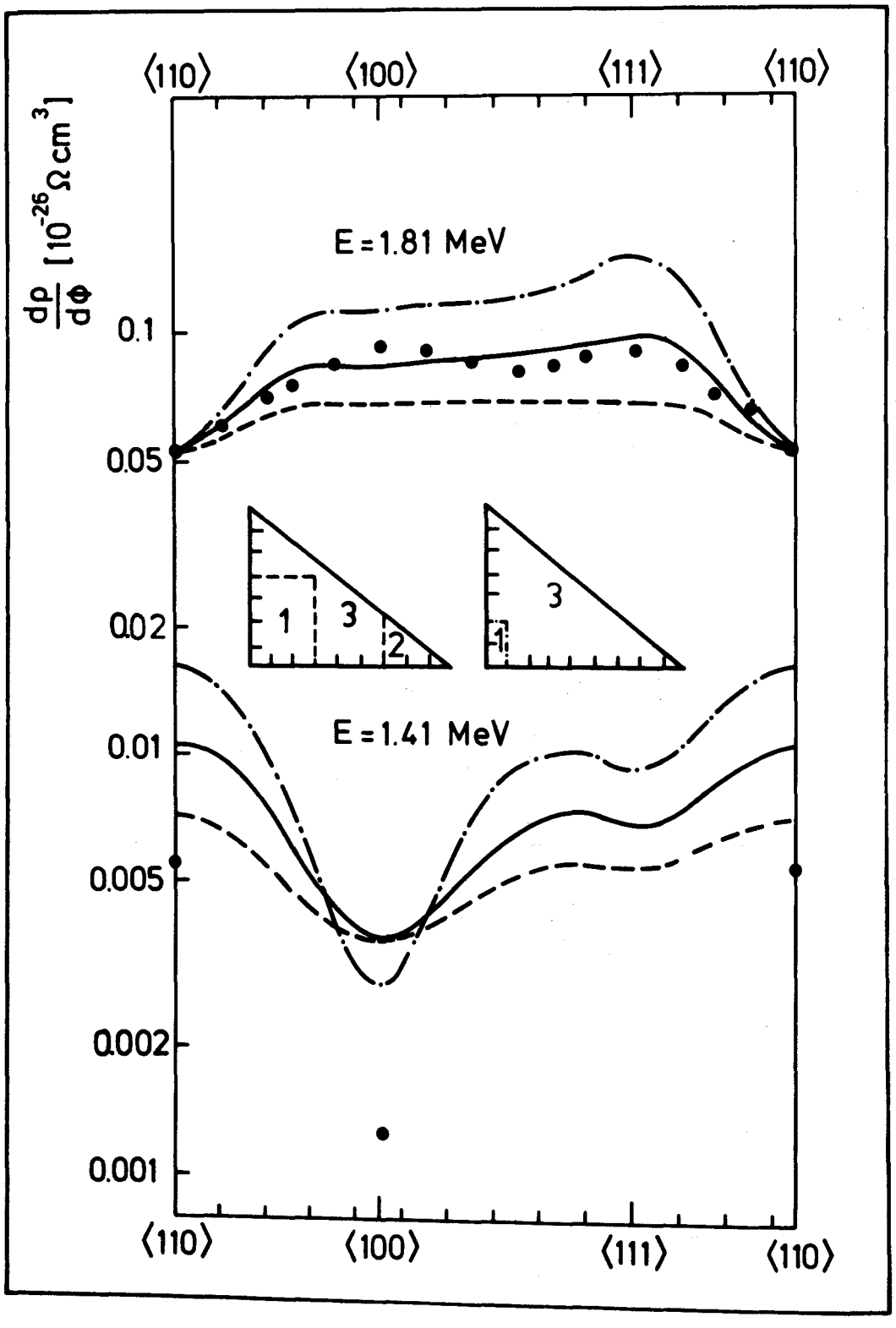


Fig. 40: The effect of the sizes of the zones 1 and 2 of the optimal threshold energy profile on the calculated damage rates at 400 K.

The fit is much more sensitive to changes of the threshold energy values in the "low-threshold" zones (1) and (2) than to changes of the value in zone (3). On the other hand, the value in this zone must be known to estimate the so-called displacement energy. The displacement energy is defined as the average of the threshold energies over all lattice directions.

An attempt was made to find a lower limit of the threshold energy in zone (3) which would be in agreement with the measurements. In the figures 41-43 curves calculated with the three profiles given in fig. 34 are compared to the data with $T_d(3)$ equal to 40,50 and 57 eV. For all three temperatures fits within the experimental error bars were obtained only when $T_d(3)$ was above 50 eV. At 4.5 K the calculations are very insensitive to $T_d(3)$ due to the small area of zone (3). On the other hand, at 400 K, 50 eV as well as 57 eV give reasonable fits. With 50 eV as a lower limit of $T_d(3)$ for all three temperatures, lower limits of the average displacement energies are derived:

4.5 K: 39 eV

40 K: 43 eV

400 K: 47 eV

The limit at 4.5 K is in reasonable agreement with the average displacement energy of around 42 eV derived from Ref. /1/. The data at 40 K and 400 K seem to indicate an increase of the average displacement energy with temperature.

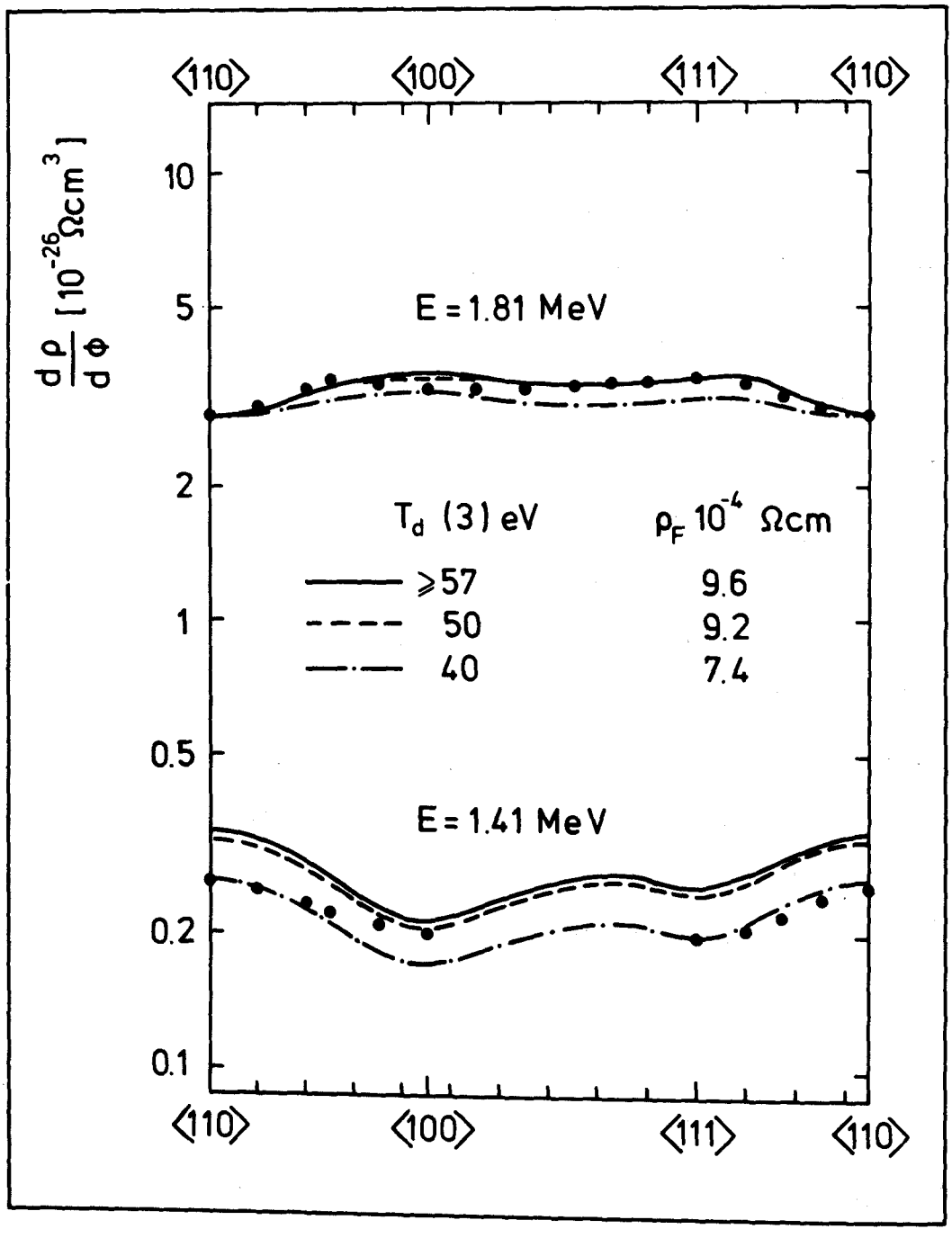


Fig. 41: The effect of the threshold energy value in zone 3 of the optimal threshold energy profile on the damage rate at 4.5 K.

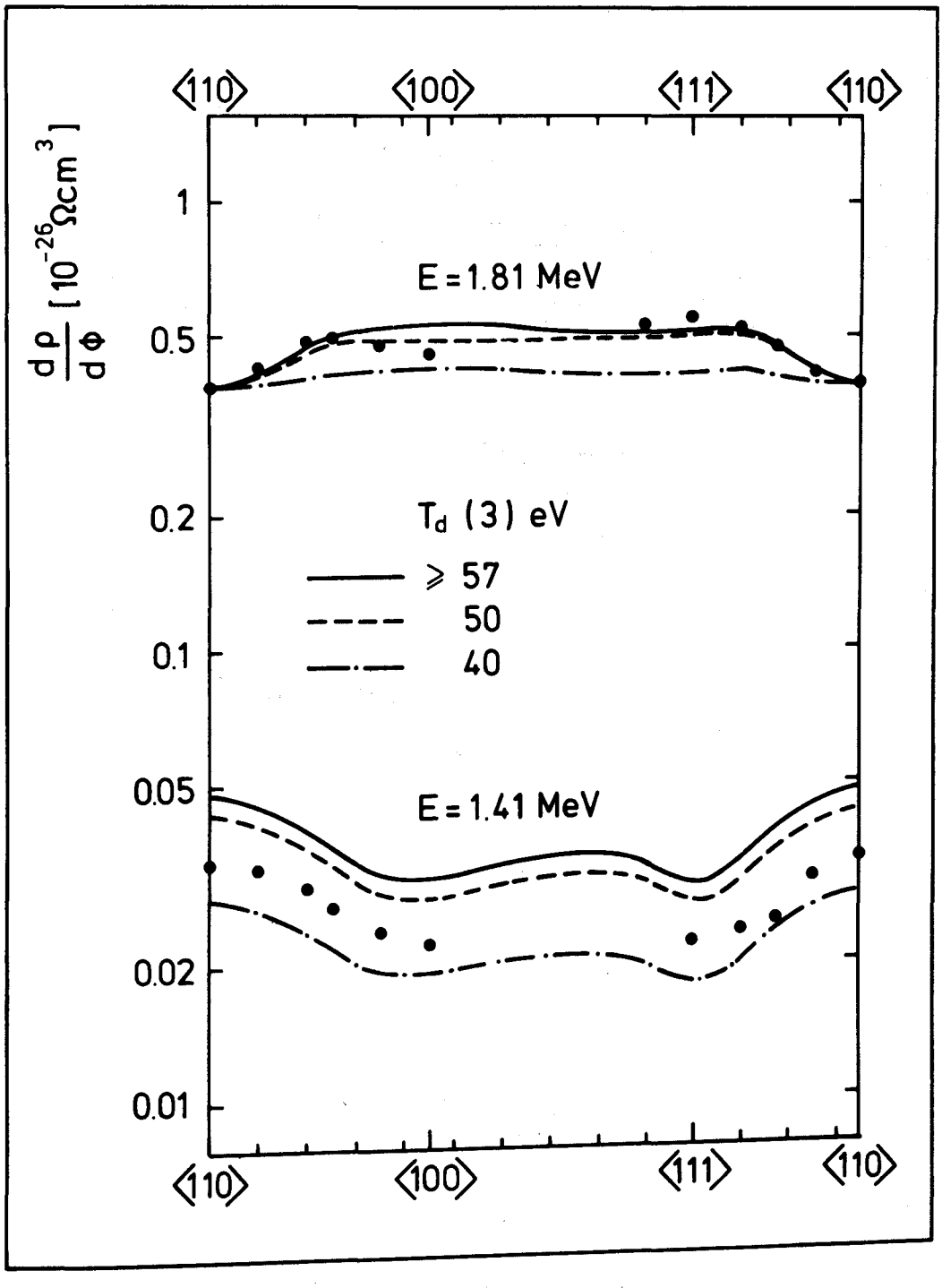


Fig. 42: The effect of the threshold energy value in zone 3 of the optimal threshold energy profile on the damage rate at 40 K.

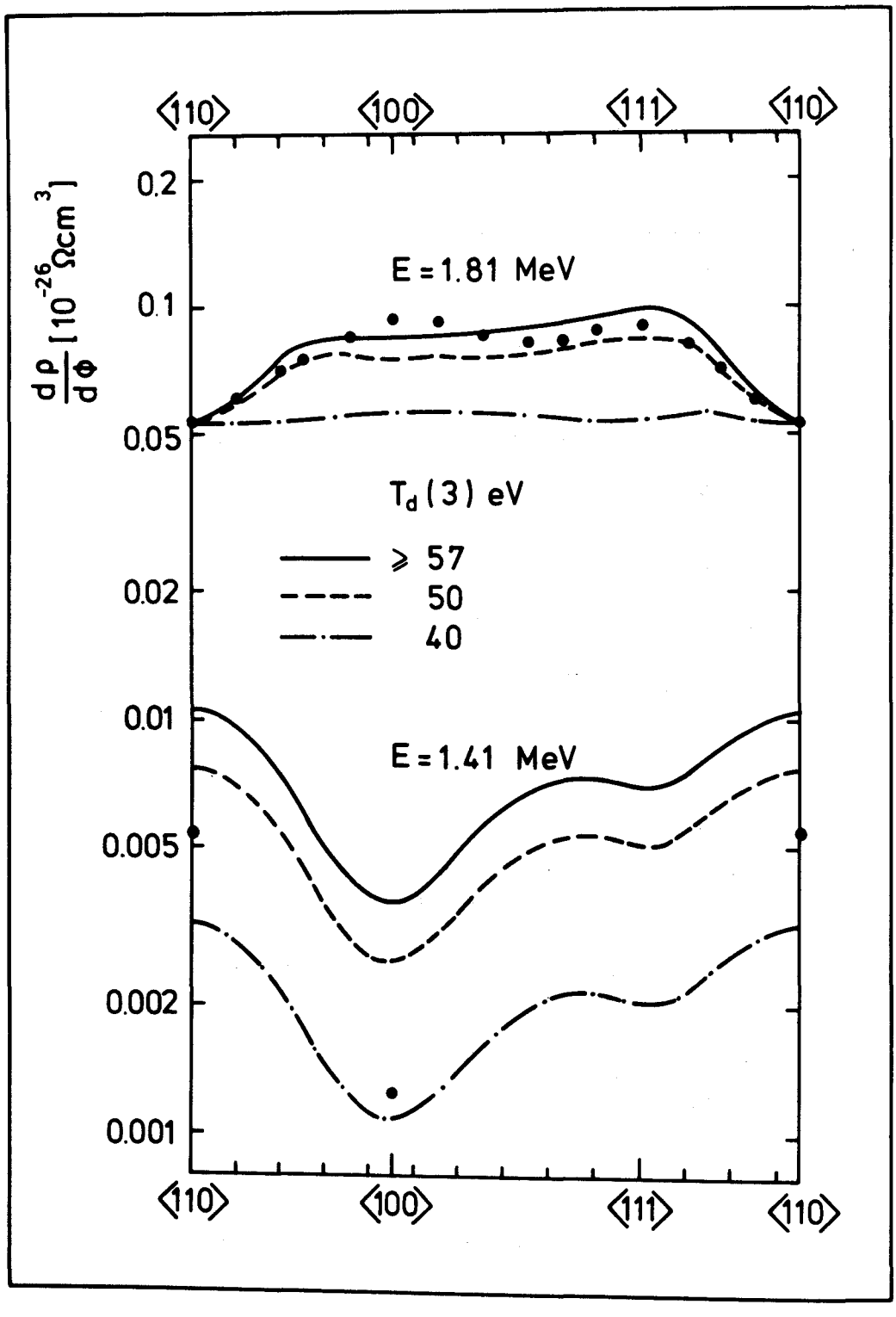


Fig. 43: The effect of the threshold energy value in zone 3 of the optimal threshold energy profile on the damage rate at 400 K.

## VI.4 Effect of beam spreading on the calculated damage rates

A further calculation was made to investigate the influence of beam spreading on the damage rates for a given threshold energy profile. The anisotropy of defect production is calculated by using the profile of fig. 34. The results for the three temperatures are shown in fig. 44-46. The average cross section for the spreaded beam gives a significantly reduced anisotropy (solid line) especially at the lower energy, compared to the calculations for an unspreaded beam (broken line). This effect is even more pronounced at the higher temperatures due to the more anisotropic threshold energy profiles. It is seen, that reducing beam spreading by omitting a window and using thinner specimens - as is done for example in HVEM experiments - should make it possible to investigate finer details of the threshold energy profile.

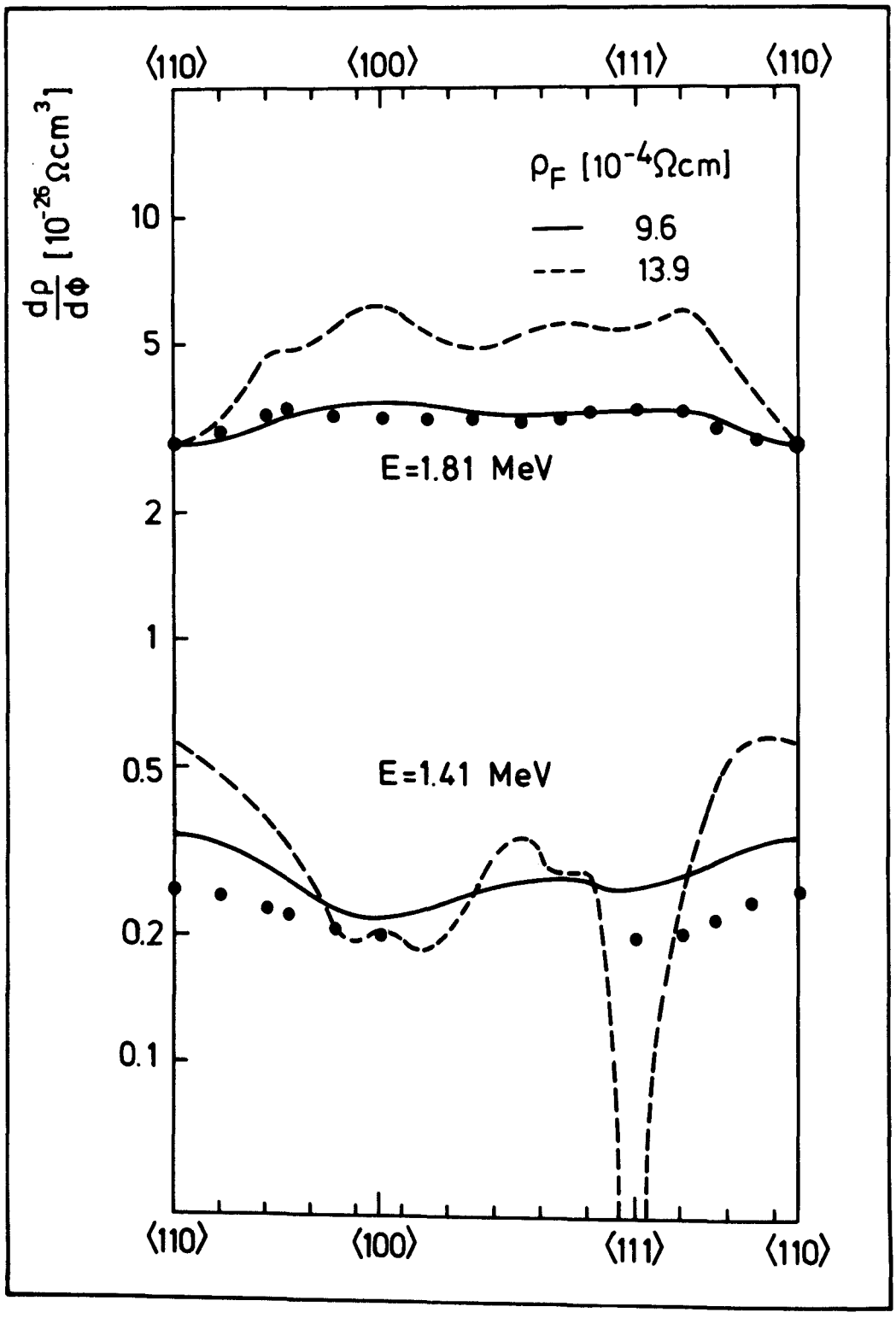


Fig. 44: The effect of the electron beam spreading on the damage rate at 4.5 K.

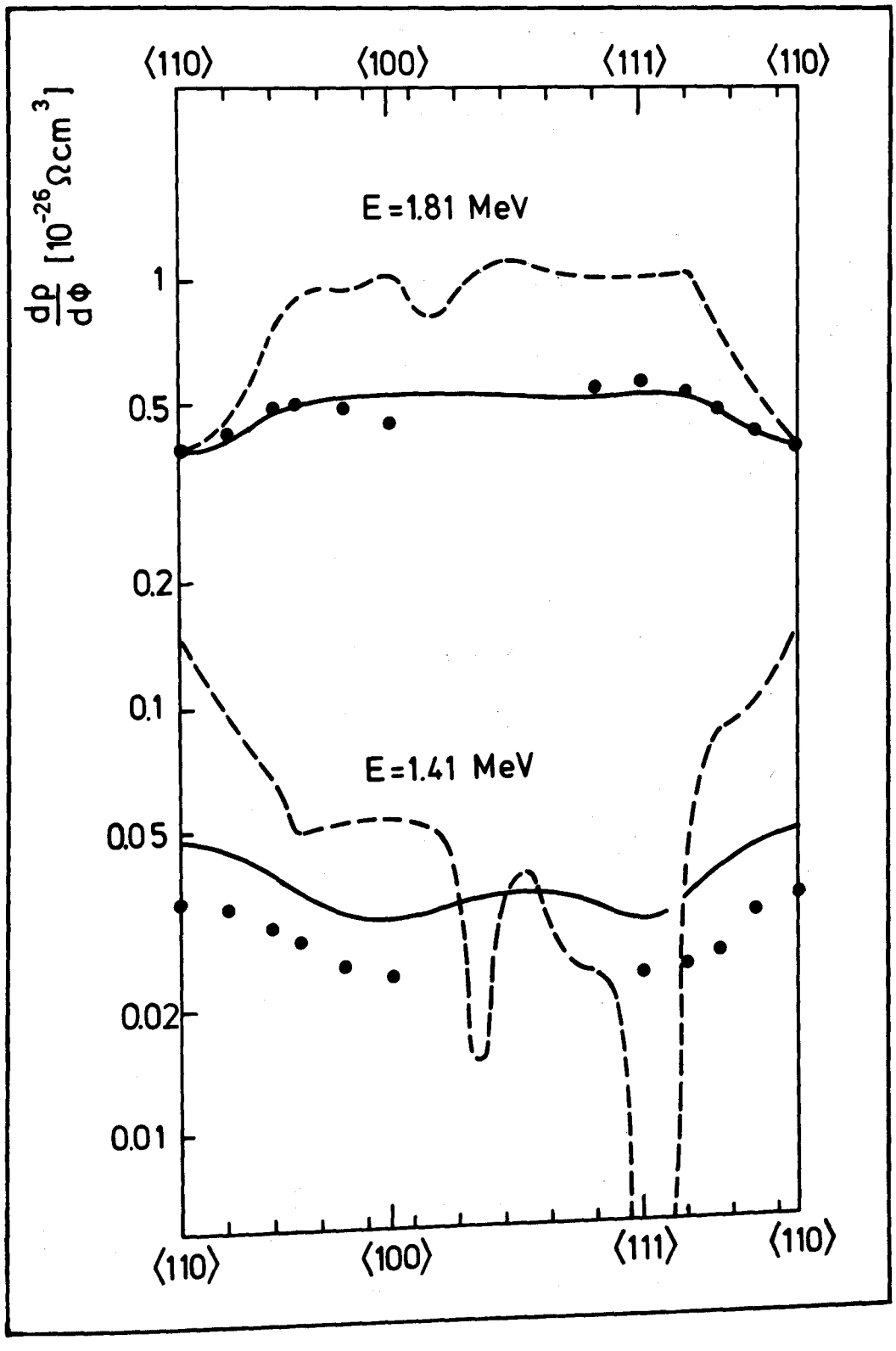


Fig. 45: The effect of the electron beam spreading on the damage rate at 40 K.

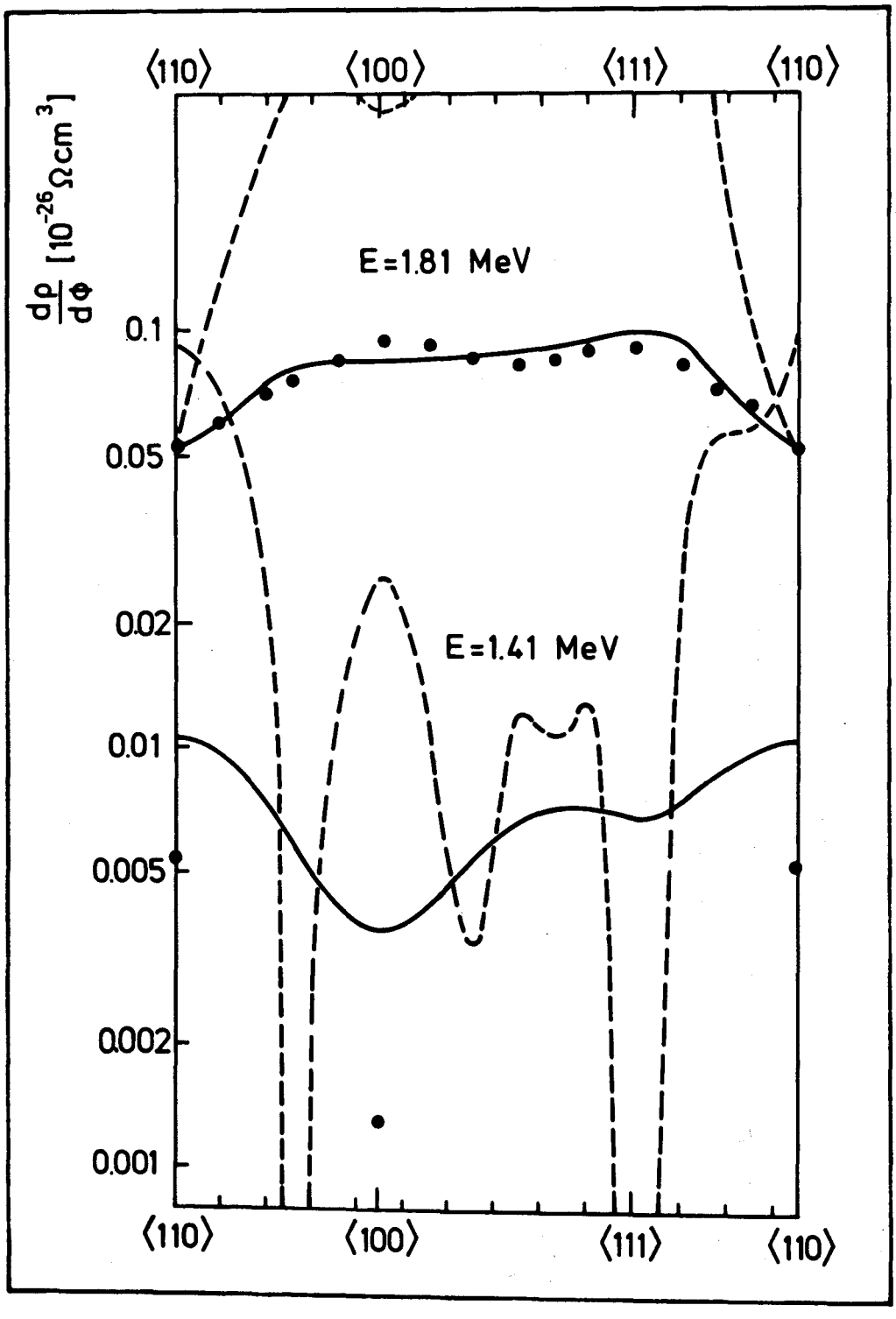


Fig. 46: The effect of the electron beam spreading on the damage rate at 400 K.

# CHAPTER VII

## VII. Discussion

In this section the following main results of this work will be discussed:

1) The measured damage rate decreases with temperature.
2) The directional dependence of the damage rates and consequently the threshold energy profile becomes increasingly anisotropic with increasing temperature.
3) The minimum threshold energy shows no significant dependence on temperature.

The damage rate $\frac{\Delta\rho}{\Delta\phi}$ of irradiations at temperatures above stage I is determined by two processes

a) the production of freely migrating interstitials
b) the prevention of part of these interstitials from recombination by trapping at impurities or clustering.

For small defect concentration $c_F$, when clustering is negligible, the damage rate is given by /45/:

$$\frac{\Delta\rho}{\Delta\phi} = \sigma_F \left(1-\frac{r_v}{r_p}\right) \frac{\rho_F^t c_t r_t}{c_t r_t + c_F r_V} \qquad (7.1)$$

$\sigma_F$ is the production cross section of freely migrating interstitials and the factor $(1-\frac{r_v}{r_p})$ gives the probability for these interstitials to avoid recombination with their own vacancies during their thermally activated migration. $r_p$ is the average

distance from the vacancy at which these interstitials are produced and $r_v$ is the radius of the recombination volume of the vacancy. As the concentration of active traps $c_t$ and their average capture radius $r_t$ and possibly also the resistivity contribution $\rho_F^t$ of a Frenkel pair, consisting of an isolated vacancy and a trapped interstitial, depend on temperature, it is necessary to keep the last factor in equation (7.1) constant to get some information on the temperature dependence of the production term $\sigma_F(1-\frac{r_v}{r_p})$. This has been done for copper by Becker et al. /45/ by extrapolating to zero defect concentration ($c_F = 0$) and for platinum by Coltman et al. /46-47/ by annealing after each irradiation to a fixed temperature above the maximum irradiation temperature. In these cases the damage rate was found to increase between the end of stage I and 200 K /45/ or 270 K /46/ by about a factor of two.

In the present experiment, it was not possible for experimental reasons to apply either technique to keep the last factor in equation (7.1) constant. In this case the reduction in trap concentration with increasing temperature will in general cause the damage rate to decrease. Experimentally a drop of the damage rate by a factor of 2.3 from 8 K to 30 K and by a factor of about 3 from 200 K to 350 K was found by Jackson /48/ after 22-MeV deuteron irradiation of platinum. Similarly a drop by a factor of 4 between 210 K and 418 K can be extrapolated from Coltman et

al.'s thermal neutron data /47/. In the present experiment an even steeper decrease of the damage rate was found between 4.5 K and 40 K. This is in agreement with the more pronounced annealing in stage I after low energy electron irradiation /36/ compared to thermal neutron and fast-deuteron irradiation. At the moment it cannot be decided whether the steeper decrease from 40 K to 400 K must be ascribed to a higher temperature sensitivity of the production term due to the much softer recoil spectrum or to the higher and possibly different trap population in the present experiment.

In this experiment the directional dependence of the damage rate is determined by comparing damage rates of one specimen for various irradiation directions. In this case, the last factor in equation (7.1) is constant and therefore the anisotropy of the damage rates directly reflects the anisotropy of the production term $\sigma_F(1-\frac{r_v}{r_p})$. There is experimental as well as theoretical evidence that all three parameters in this term are anisotropic.

In computer calculations an anisotropic recombination radius $r_v$ /18/ and a dependence on lattice direction of the radius of Frenkel pairs $r_p$ was found. $r_v$ is maximum along <110> and decreases with increasing temperature /29/, while $r_p$ at low energy is also maximum along <110> and also decreases with temperature /29,49/. Annealing experiments on platinum /27/ showed

that the production cross section of free interstitials $\sigma_F$ for an irradiation energy of 1.41 MeV is maximum for irradiation along <110>, while at 1.81 MeV this direction exhibits a minimum (Fig. 7a) in agreement with the present experiment.

That means, the directional dependence of the damage rate at 40 K can be explained by the anisotropy of $\sigma_F$, while $\frac{r_v}{r_p}$ is expected to be rather isotropic as the directional dependence of $r_v$ and $r_p$ are similar.

The smaller low-threshold energy windows found at 40 K compared to 4.5 K can be explained in terms of the different defect patterns which are produced by a 4.5 K and a 40 K irradiation. At 40 K close Frenkel pairs and correlated pairs are not stable, and it is known /27/ that at low impact energies close pairs are preferentially produced by impacts offthe <110> and <100> directions (Fig. 7b). If the close pairs are extinct on irradiating at 40 K, the outer areas of the zones around <110> and <100> are missing, causing the low threshold energy zones around these directions to shrink.

An alternative explanation would be in terms of temperature effects on the defocussing of replacement sequences by thermal lattice vibration. As thermal vibrations are still low at 40 K, their influence on the defect production processes via $r_p$ is assumed to be small at this temperature. On the other hand the increasing anisotropy between 40 K and 400 K may well be ascribed to this effect.

The effect of thermal lattice vibrations on the length $r_p$ of a replacement sequence is shown schematically in fig. 47. While in a rigid lattice (0 K) an impact at an angle $\alpha$ is focused along the close packed direction resulting in a length of the sequence beyond the recombination radius $r_v$, focusing is reduced or inhibited by the lattice vibrations at the higher temperature, thus reducing the radius $r_p$ of the Frenkel pair /45/. When the radius is reduced below the recombination radius, no stable defect is produced.

An alternative explanation would be in terms of a temperature dependence of the recombination radius $r_v$ (fig. 48). At a given impact energy, replacement sequences are shorter for increasing angles $\alpha$. If an increase in the recombination radius with increasing temperature is assumed, a Frenkel pair which is stable at 4.5 K becomes unstable at 400 K. Only long replacement sequences resulting from small angles $\alpha$ would then be stable at higher temperatures (fig. 48b).

On the other hand theoretical considerations /50/ as well as the experimentally found increase of the damage rate throughout stage II /45-47/ point to a reduction of $r_v$ with increasing temperature.

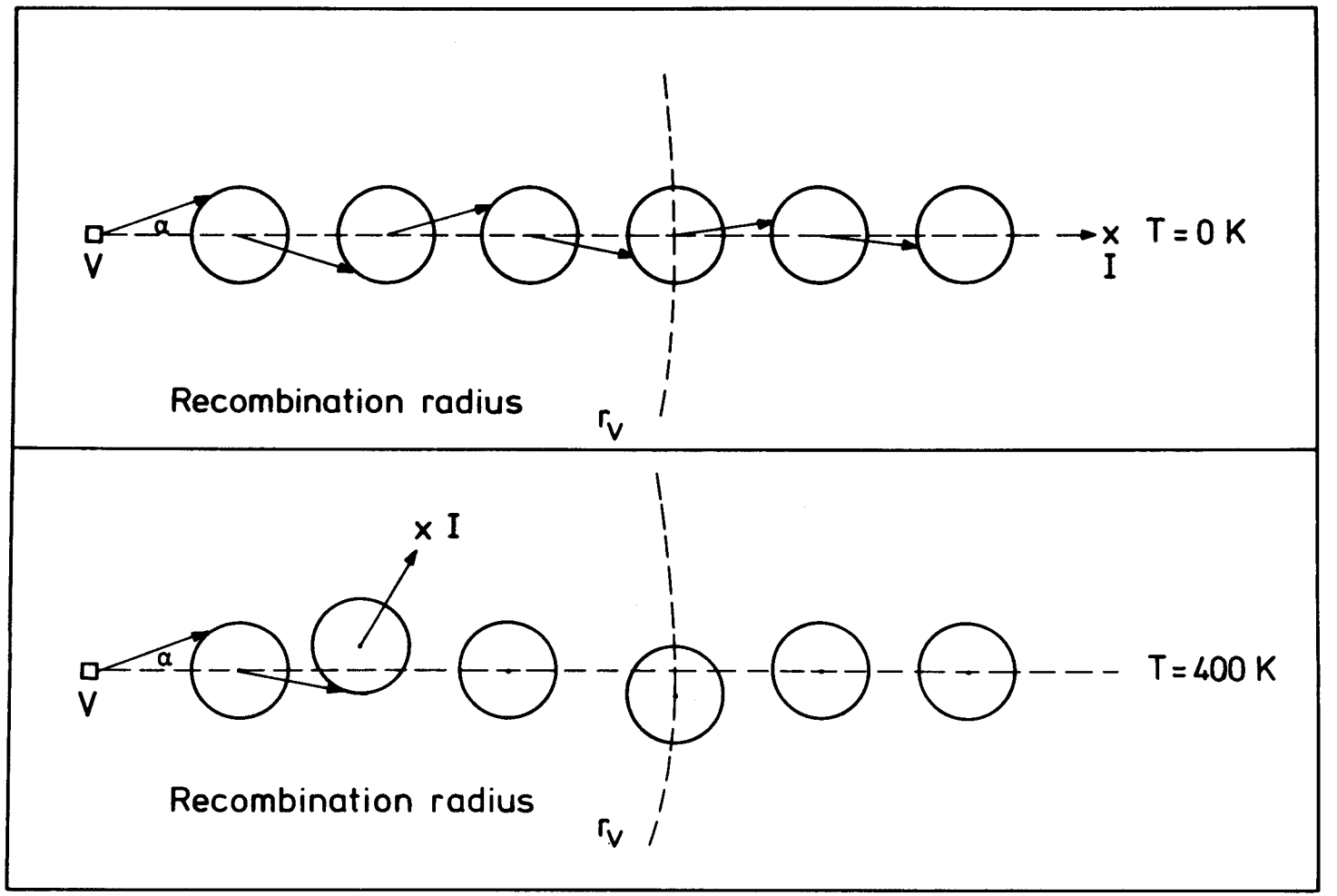


Fig. 47: A postulated model explaining the role of thermal vibrations on the replacement sequences.

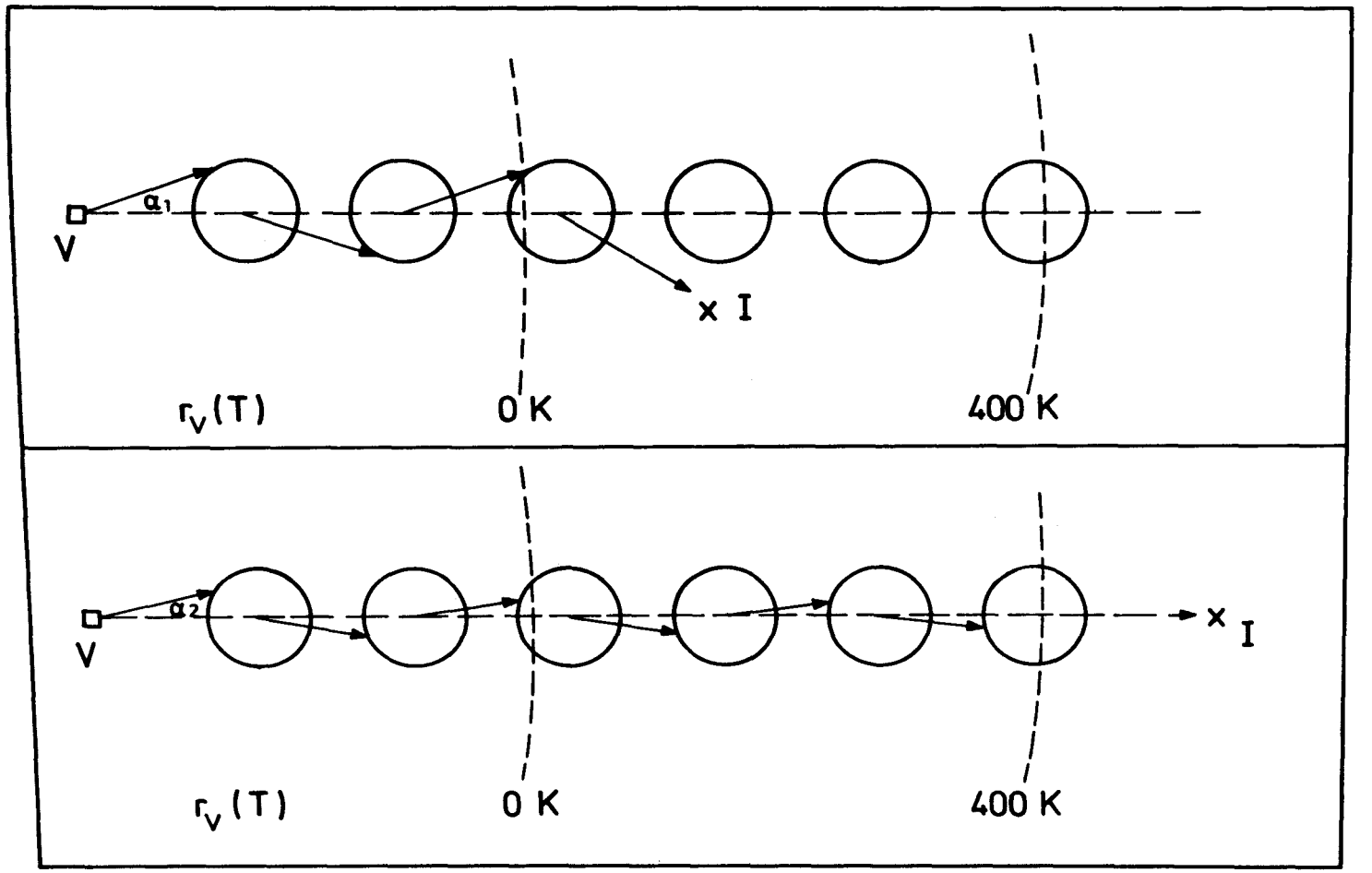


Fig. 48: The effect of the temperature dependence of the recombination volume on the replacement sequences.

With the exception of the work of Roberts et al. /51/ on silver, experimental results on the temperature dependence of the minimum threshold energy are available so far only for copper /31-34,52/. The general result is, that the minimum threshold energy is fairly constant up to temperatures of about 100 K /33,34/ and drops gradually at higher temperatures by up to a factor of two /31,32,52/. At the moment, the reason for this decrease is not established, precluding any inferences for the case of platinum.

Computer simulations for the cases of Cu /28,29,49/ and W /53/ consistently gave a more or less symmetric distribution of threshold energies around the 0 K-value at higher temperature instead of an unique value at 0 K. That means the minimum threshold energy may be slightly reduced at higher temperatures, e.g. by about 20% at 300 K in W /53/.

A reduction of the minimum threshold energy by this factor is within the error bars of an extrapolation of the 400 K data in fig. 28.

This uncertainty in the minimum threshold energy precludes for the moment safe statements about a temperature dependence of the average displacement energy.

# CHAPTER VIII

## VIII. Conclusions:

Conclusions of this work are:

1. By electron irradiation of platinum the anisotropy of the damage rate increases with increasing temperature.
2. Fitting of the damage rate data by a threshold energy profile gives:
   a) Zones of minimum threshold energy are around the <110> and <100> direction, while the maximum threshold energy is found around the direction <111>.
   b) with increasing temperature the areas of the windows with small threshold energy around the close-packed directions <110> and <100> decrease.
3. The increasing anisotropy of the threshold energy with temperature is explained by two mechanisms:
   a) The change in the defect pattern between 4.5 K and 40 K due to the instability of close pairs.
   b) The defocusing of replacement sequences by thermal lattice vibration.
4. No safe statements about the temperature dependence of the minimum and the average displacement energy are possible.

# APPENDICES

# Appendix A

Computer program: Average displacement cross section of a spreaded beam.

```
C     BERECHNUNG DES GEMITTELTEN STREUQUERSCHNITTS FUER AUFGEWEITETEN
C     ELEKTRONENSTRAHL (WINKELABHAENGIGKEIT)
C     IE = ZAHL DER VERWENDETEN ENERGIEN (MAXIMAL 5)
C     ID = ZAHL DER VERWENDETEN DICKEN (MAXIMAL 4)
C     ITD = ZAHL DER VERWENDETEN SCHWELLEN
C     SB = SCHRITTWEITE (IN GRAD) BEI DER BERECHNUNG
C     SW = SCHRITTWEITE (IN GRAD) BEI DER INTEGRATION
C     TDSW= SCHRITTWEITE DER SCHWELLEN
      DIMENSIONE(5),RK(5,37),SINUS(180),COSIN(180),SINUB(180),COSIB(180
      DIMENSION Q(1001),H(180,180),WQ(90)
      CALL MASKE
C
      READ(5,1001) IE,ITD,TDSW,SW,SB
 1001 FORMAT(2I2,3F4.1)
      READ (5,1002) Z,A,TDMIN
 1002 FORMAT (3F7.3)
      WRITE(6,1003) Z,A,TDMIN,SW
 1003 FORMAT(1X,'KERNLADUNG:',F5.0,3X,'ATOMGEWICHT:',F7.3,
     1 3X,'MINIMALE SCHWELLE:',F4.1,/,
     2 1X,'SCHRITTWEITE BEIM INTEGRIEREN:',F4.2,' (GRAD)',/)
C
      PI    = 3.14159265
      BOG   = PI / 180.
      BOS = SW * BOG
      BOQ = BOS**2
      BOOS = BOQ/PI
      BOB = SB * BOG
      BOZ = 2.5* BOG
      CK1   = 0.079383  *Z*Z
      CK2   = PI*Z/137.
      CKE = 560.8 / A
C
      FSH = 180. / SW
      NSH = FSH
      NHO = NSH/2
      NH1 = NHO + 1
      ARG = -(PI+BOS) / 2.
      DO 5 I = 1,NSH
      ARG = ARG + BOS
      SINUS(I) = SIN(ARG)
    5 COSIN(I) = COS(ARG)
C
      FS1 = 90./SB
      NS1 = FS1
      ARG = -BOB
      DO 6 I = 1,NS1
      ARG = ARG + BOB
      SINUB(I) = SIN(ARG)
    6 COSIB(I) = COS(ARG)
C
      DO 10 I = 1,IE
      READ(5,1005) E(I)
 1005 FORMAT(1X,F6.3)
      READ(5,1006) (RK(I,II),II=1,36)
 1006 FORMAT(9(1X,F5.3))
      RK(I,37) = 1.0
      READ(5,1015) D,AQ
 1015 FORMAT(2(1X,F6.3))
      AB = AQ * BOG
      ABQ = AB**2
      ES = E(I)/0.511
      ESS = ES * (ES + 2.0)
      ESS2 = (ESS) **2
      ESP = ( ES + 1.0) **2
      TM = ESS * CKE
      TD = TDMIN - TDSW
      C1 = CK1 * ESP / ESS2
      C2 = ESS/ESP
      C3 = CK2 * SQRT (C2)
C
      DO 14 ICB = 2,1001
```

```
      CB1 = ICB - 1
      CB = CB1/1000.
      CC = CB**2
      AR = ARCOS(CB) / BOZ + 1.5
      IR = AR
   14 Q(ICB) = C1*(1.-C2*CC+C3*(CB-CC)) * RK(I,IR) / (CB*CC)
C
C     ODER EINLESEN DER WIRKUNGSQUERSCHNITTE
C     READ(5,1014) (Q(IB),IB = 1,91)
C1014 FORMAT(10(1X,F6.2))
C
      DO 15 LT = 1,NSH
      CLT = COSIN(LT)
      CBOOS = CLT*BOOS / ABO
      DO 15 LP = 1,NSH
      CA = CLT * COSIN(LP)
      BO = ARCOS(CA)
      EFU = EXP(-(BO/AB)**2)
   15 H(LT,LP) = CBOOS * EFU
C
      WRITE(6,1016) E(I),D,AO,TM
 1016 FORMAT(1X,'ENERGIE=',F4.2,'(MEV)',3X,'DICKE=',F5.2,'(MYCROM)',
     1 3X,'GAUSSBREITE=',F6.3,/,' MAXIMAL UEBERTRAGENE ENERGIE =',F7.2,
     2 '(EV)',/,' WINKEL(=0.1...GRAD)   GEMITTELTER WIRKUNGSQU.(BARN)')
      WRITE(7,1017) E(I)
 1017 FORMAT(F5.3)
C
      DO 11 II = 1,ITD
      FII = II
      TDS = TD + TDSW*FII
      CTD = SQRT(TDS/TM)
      IF(CTD.GT.1.0) GOTO 10
      WRITE(6,1019) TDS
 1019 FORMAT(1X,'SCHWELLE :',F6.2)
C
      DO 20 KP = 1,NS1
C
      B = 0.0
      DO 21 LT = 1,NSH
      CLT = COSIN(LT)
      CCKP = CLT * COSIB(KP)
      CSKP = CLT * SINUB(KP)
C
      DO 21 LP = 1,NSH
      CB = COSIN(LP)*CCKP + SINUS(LP)*CSKP
      IF(CB.LT.CTD) GOTO 21
      FCB = CB*1000. + 1.5
      ICB = FCB
C     IB = ARCOS(CB) / BOG + 1.5
C     B = B + Q(IB) *H(LT,LP)
      B = B + Q(ICB)*H(LT,LP)
   21 CONTINUE
   20 WQ(KP) = B
C
      WRITE(6,1020) (WQ(KP),KP=1,NS1)
C     AUSGABE IN SCHRITTEN VON SW (0,SW,2*SW,...)
      WRITE(7,1020) (WQ(KP),KP=1,NS1)
 1020 FORMAT(10(1X,F6.2))
   11 CONTINUE
   10 CONTINUE
      STOP
      END
```

# Appendix B

Computer program: Calculation of the defect production for a given threshold energy profile.

```
C
C     BERECHNUNG DER DEFEKT ERZEUGUNGSRATEN BEI VORGEGEBENEM SCHWELLEN
C     ENERGIEPROFIL
C
C     NE= ZAHL DER ENERGIEN(2) ,NW= ZAHL DER WINKEL (15) ,
C     ND = ZAHL DER SCHWELLEN
C
C     WINKEL DER MESSWERTE ( THETA , PHI )
C     110 ( 0. 0) , 100 ( 0.45) , 111 (35. 0)
C
C     SCHRITTWEITE FUENF GRAD
C
C
      DIMENSION EO(2),DM(2,15),
     1 DRECH(2,15),TH(15),PH(15),CKT(15),SKT(15),CKP(15),SKP(15),
     2 WO(2,35,90),NAL(15,36,72),F(36,72),
     3 SINUS(72),COSIN(72),COSTH(36)
C
C
      CALL MASKE
C
C     NZA=ANZAHL DER SCHWELLENENERGIEPROFILE
C
      READ(5,999) NZA
      READ(5,999) NE,NW,ND
  999 FORMAT(3I2)
      FND = ND+1
      ND1 = ND - 1
      NEW= NE * NW
      NEN = NE /2 + 1
C
      WRITE (6,1041)
 1041 FORMAT(1X,'PROGRAMM : T 2',/,1X,'EINGELESENE DATEN',/)
C
C
C     EINLESEN DER ELEMENTDATEN
C
      READ (5,1000) Z,A,TDMIN,DTD
 1000 FORMAT (4F7.3)
      CKE = 560.8/A
      TM0 = TDMIN - DTD
      TM1 = TDMIN - DTD
      TDMAX = TM1 + FND*DTD
      TTD = TM1/DTD
      WRITE (6,1042) Z,A,TDMIN,DTD,TDMAX
 1042 FORMAT(1X,'ELEMENT',3X,' Z = ',F3.0,3X,' A = ',F7.3,3X,
     1 'TD = ',F6.2,'(+',F3.1,')',3X,'TDMAX = ',F6.2,' (EV)',/)
C
C
C     EINLESEN DER MESSWINKEL
C
C
      READ(5,1011) (TH(I),PH(I), I = 1,NW)
 1011 FORMAT(15F4.1)
C
C
C     EINLESEN DER ENERGIEWERTE(EO)(MEV),MESSWERTE(DM)UND WIRKUNGS-
C      QUERSCHNITTE(BARN)
C
      DO 5 I = 1,NE
      READ (5,1005) EO(I)
 1005 FORMAT (F5.3)
C
C
      WRITE(6,1053)EO(I)
 1053 FORMAT(//,1X,'ENERGIEWERT = ',F5.3,'MEV',//)
C
C
    4 READ (5,1051) (DM(I,J), J = 1,NW)
 1051 FORMAT(5F8.3)
      ES = EO(I) / 0.511
```

```
      ESS= ES * (ES+2.0)
      TM = CKE * ESS
C
C
      WRITE(6,1054)TM
 1054 FORMAT(//,1X,'TM = ',F8.4,//)
C
C
      DO 5 II = 1,ND
      FII = II
      TDV = TMO + FII*DTD
      IF(TM.GT.TDV) GOTO 7
      DO 6 III = 1,90
    6 WO(I,II,III) = 0.0
      GOTO 5
    7 CONTINUE
      READ(5,1010) (WO(I,II,III) , III = 1,90)
 1010 FORMAT (10(1X,F6.2))
      WRITE(6,1006) TDV
 1006 FORMAT(1X,'SCHWELLE FUER WO :',F6.2)
      WRITE(6,1110) (WO(I,II,III) , III=1,90)
 1110 FORMAT(1X,20F6.2)
    5 CONTINUE
C
C
C     ****************************************************************
C
C     BERECHNUNG UND SPEICHERUNG VON COSINUS ALPHA
C     ALPHA = WINKEL ZWISCHEN MESSPUNKT UND AUFPUNKT
C
      PI    = 3.1416
      BOG   = PI / 180.
      BOF = 5. * BOG
      CO = 100./(BOF)**2
C
      RARG = -182.5
      DO 20 J = 1,72
      RARG = RARG + 5.
      ARG = RARG * BOG
      W = SIN(ARG)
      SINUS(J) = W
      W = COS(ARG)
   20 COSIN(J) = W
C
      DO 21 I = 1,NW
      TB = TH(I) * BOG
      PB = PH(I) * BOG
      CKT(I) = COS(TB)
      SKT(I) = SIN(TB)
      CKP(I) = COS(PB)
   21 SKP(I) = SIN(PB)
C
      DO 25 J = 1,NW
      IJ = 18
C
      DO 25 JJ = 1,36
      IJ = IJ + 1
      COSTH(JJ) = COSIN(IJ)
      CKGT = CKT(J) * COSIN(IJ)
      SKGT = SKT(J) * SINUS(IJ)
C
      DO 25 JJJ = 1,72
      CSP = CKP (J) * COSIN (JJJ) + SKP(J) * SINUS (JJJ)
      CA  = CKGT *CSP + SKGT
      IF(CA.LT.0.0) CA = 0.0
      ALPHA = ARCOS(CA)/BOG + 1.5
   25 NAL(J,JJ,JJJ) = ALPHA
C
C     ****************************************************************
C
C
C     EINLESEN DER AUSGANGSPARAMETER IM ORIENTIERUNGSDREIECK
      WRITE(6,1052)
```

```
 1052 FORMAT(//,1X,'SCHWELLENENERGIEPROFIL : ')
C
      DO 100 IZA = 1,NZA
C
      DO 49  I = 1,36
      DO 49 II = 1,72
   49 F(I,II) = TOMIN
C
      DO 40 J = 19,25
      IPHEND = 64 - J
      IF (J.EQ.24) IPHEND = 39
      IF (J.EQ.25) IPHEND = 38
      READ (5,1040) (F(J,JJ) , JJ = 37,IPHEND)
 1040 FORMAT (9F7.2)
      WRITE (6,1046) (F (J,JJ) , JJ = 37,IPHEND)
 1046 FORMAT(1X,9F7.2)
   40 CONTINUE
C
C     ***************************************************************
C
C     AUFFUELLEN DER 1/16 - KUGEL  (J = 19,36   1J = 37,45  )
C
C
      F(20,45) = 0.00*F(19,43)+0.50*F(19,44)+0.00*F(19,43)+0.50*F(19,44
      F(21,43) = 0.05*F(20,42)+0.07*F(20,43)+0.07*F(21,42)+0.81*F(21,43
      F(21,44) = 0.03*F(19,42)+0.04*F(19,43)+0.04*F(20,42)+0.90*F(20,43
      F(21,45) = 0.01*F(19,42)+0.49*F(19,43)+0.01*F(19,42)+0.49*F(19,43
      F(22,42) = 0.11*F(21,41)+0.16*F(21,42)+0.15*F(22,41)+0.58*F(22,42
      F(22,43) = 0.08*F(20,41)+0.11*F(20,42)+0.11*F(21,41)+0.70*F(21,42
      F(22,44) = 0.05*F(19,41)+0.07*F(19,42)+0.06*F(20,41)+0.82*F(20,42
      F(22,45) = 0.01*F(19,41)+0.49*F(19,42)+0.01*F(19,41)+0.49*F(19,42
      F(23,41) = 0.18*F(22,40)+0.24*F(22,41)+0.23*F(23,40)+0.35*F(23,41
      F(23,42) = 0.14*F(21,40)+0.21*F(21,41)+0.18*F(22,40)+0.47*F(22,41
      F(23,43) = 0.11*F(20,40)+0.16*F(20,41)+0.14*F(21,40)+0.60*F(21,41
      F(23,44) = 0.07*F(19,40)+0.10*F(19,41)+0.09*F(20,40)+0.74*F(20,41
      F(23,45) = 0.02*F(19,40)+0.48*F(19,41)+0.02*F(19,40)+0.48*F(19,41
      F(24,40) = 0.14*F(22,38)+0.19*F(22,39)+0.18*F(23,38)+0.49*F(23,39
      F(24,41) = 0.15*F(21,39)+0.16*F(21,40)+0.30*F(22,39)+0.39*F(22,40
      F(24,42) = 0.17*F(21,39)+0.27*F(21,40)+0.19*F(22,39)+0.37*F(22,40
      F(24,43) = 0.13*F(20,39)+0.21*F(20,40)+0.16*F(21,39)+0.49*F(21,40
      F(24,44) = 0.09*F(19,39)+0.14*F(19,40)+0.12*F(20,39)+0.65*F(20,40
      F(24,45) = 0.03*F(19,39)+0.47*F(19,40)+0.03*F(19,39)+0.47*F(19,40
C     F(25,38) = 0.16*F(24,37)+0.23*F(24,38)+0.20*F(25,37)+0.41*F(25,38
      F(25,38) = F(25,37)
      F(25,39) = 0.07*F(23,37)+0.11*F(23,38)+0.09*F(24,37)+0.73*F(24,38
      F(25,40) = 0.12*F(22,37)+0.18*F(22,38)+0.15*F(23,37)+0.55*F(23,38
      F(25,41) = 0.14*F(21,38)+0.15*F(21,39)+0.31*F(22,38)+0.40*F(22,39
      F(25,42) = 0.14*F(20,38)+0.15*F(20,39)+0.26*F(21,38)+0.45*F(21,39
      F(25,43) = 0.16*F(20,38)+0.27*F(20,39)+0.17*F(21,38)+0.40*F(21,39
      F(25,44) = 0.11*F(19,38)+0.18*F(19,39)+0.14*F(20,38)+0.57*F(20,39
      F(25,45) = 0.04*F(19,38)+0.46*F(19,39)+0.04*F(19,38)+0.46*F(19,39
      F(26,37) = 0.11*F(24,37)+0.11*F(24,37)+0.39*F(25,37)+0.39*F(25,37
      F(26,38) = 0.12*F(23,37)+0.12*F(23,37)+0.38*F(24,37)+0.38*F(24,37
      F(26,39) = 0.15*F(23,37)+0.32*F(23,37)+0.15*F(24,37)+0.38*F(24,37
      F(26,40) = 0.13*F(22,37)+0.23*F(22,37)+0.14*F(23,37)+0.50*F(23,37
      F(26,41) = 0.15*F(21,37)+0.15*F(21,38)+0.31*F(22,37)+0.39*F(22,38
      F(26,42) = 0.13*F(20,37)+0.14*F(20,38)+0.24*F(21,37)+0.50*F(21,38
      F(26,43) = 0.14*F(19,37)+0.16*F(19,38)+0.24*F(20,37)+0.47*F(20,38
      F(26,44) = 0.13*F(19,37)+0.22*F(19,38)+0.15*F(20,37)+0.49*F(20,38
      F(26,45) = 0.05*F(19,37)+0.45*F(19,38)+0.05*F(19,37)+0.45*F(19,38
      F(27,37) = 0.14*F(23,37)+0.16*F(23,38)+0.27*F(24,37)+0.43*F(24,38
      F(27,38) = 0.12*F(23,37)+0.21*F(23,37)+0.14*F(24,37)+0.52*F(24,37
      F(27,39) = 0.06*F(22,37)+0.06*F(22,37)+0.44*F(23,37)+0.44*F(23,37
      F(27,40) = 0.14*F(21,37)+0.14*F(21,37)+0.36*F(22,37)+0.36*F(22,37
      F(27,41) = 0.18*F(21,37)+0.18*F(21,37)+0.32*F(22,37)+0.32*F(22,37
      F(27,42) = 0.10*F(20,37)+0.10*F(20,37)+0.40*F(21,37)+0.40*F(21,37
      F(27,43) = 0.11*F(19,37)+0.11*F(19,37)+0.39*F(20,37)+0.39*F(20,37
      F(27,44) = 0.20*F(19,37)+0.20*F(19,37)+0.30*F(20,37)+0.30*F(20,37
      F(27,45) = 0.25*F(19,37)+0.25*F(19,37)+0.25*F(19,37)+0.25*F(19,37
      F(28,37) = 0.13*F(23,38)+0.16*F(23,39)+0.22*F(24,38)+0.49*F(24,39
      F(28,38) = 0.13*F(22,37)+0.17*F(22,38)+0.18*F(23,37)+0.52*F(23,38
      F(28,39) = 0.11*F(22,37)+0.18*F(22,38)+0.14*F(23,37)+0.56*F(23,38
```

```
F(28,40) = 0.13*F(21,37)+0.14*F(21,38)+0.24*F(22,37)+0.49*F(22,38
F(28,41) = 0.15*F(20,37)+0.20*F(20,37)+0.20*F(21,37)+0.46*F(21,37
F(28,42) = 0.11*F(20,37)+0.20*F(20,37)+0.14*F(21,37)+0.56*F(21,37
F(28,43) = 0.09*F(19,37)+0.13*F(19,37)+0.13*F(20,37)+0.65*F(20,37
F(28,44) = 0.15*F(19,37)+0.34*F(19,37)+0.15*F(20,37)+0.36*F(20,37
F(28,45) = 0.07*F(19,37)+0.43*F(19,37)+0.07*F(19,37)+0.43*F(19,37
F(29,37) = 0.14*F(22,39)+0.15*F(22,40)+0.31*F(23,39)+0.40*F(23,40
F(29,38) = 0.11*F(22,38)+0.18*F(22,39)+0.13*F(23,38)+0.58*F(23,39
F(29,39) = 0.11*F(21,38)+0.14*F(21,39)+0.19*F(22,38)+0.56*F(22,39
F(29,40) = 0.17*F(21,38)+0.20*F(21,39)+0.24*F(22,38)+0.40*F(22,39
F(29,41) = 0.13*F(20,37)+0.19*F(20,38)+0.17*F(21,37)+0.51*F(21,38
F(29,42) = 0.14*F(20,37)+0.30*F(20,38)+0.15*F(21,37)+0.42*F(21,38
F(29,43) = 0.07*F(19,37)+0.10*F(19,38)+0.09*F(20,37)+0.75*F(20,38
F(29,44) = 0.12*F(19,37)+0.15*F(19,38)+0.19*F(19,37)+0.53*F(19,38
F(29,45) = 0.08*F(19,37)+0.42*F(19,38)+0.08*F(19,37)+0.42*F(19,38
F(30,37) = 0.14*F(22,39)+0.26*F(22,40)+0.16*F(23,39)+0.44*F(23,40
F(30,38) = 0.11*F(21,39)+0.15*F(21,40)+0.17*F(22,39)+0.57*F(22,40
F(30,39) = 0.10*F(21,39)+0.14*F(21,40)+0.15*F(22,39)+0.61*F(22,40
F(30,40) = 0.14*F(20,39)+0.15*F(20,40)+0.30*F(21,39)+0.40*F(21,40
F(30,41) = 0.13*F(20,38)+0.22*F(20,39)+0.15*F(21,38)+0.50*F(21,39
F(30,42) = 0.13*F(19,38)+0.17*F(19,39)+0.18*F(20,38)+0.53*F(20,39
F(30,43) = 0.09*F(19,38)+0.16*F(19,39)+0.12*F(20,38)+0.64*F(20,39
F(30,44) = 0.11*F(19,38)+0.14*F(19,39)+0.17*F(19,38)+0.59*F(19,39
F(30,45) = 0.09*F(19,38)+0.41*F(19,39)+0.09*F(19,38)+0.41*F(19,39
F(31,37) = 0.11*F(21,40)+0.16*F(21,41)+0.15*F(22,40)+0.58*F(22,41
F(31,38) = 0.11*F(21,40)+0.18*F(21,41)+0.13*F(22,40)+0.58*F(22,41
F(31,39) = 0.13*F(20,40)+0.15*F(20,41)+0.25*F(21,40)+0.47*F(21,41
F(31,40) = 0.15*F(20,40)+0.16*F(20,41)+0.31*F(21,40)+0.37*F(21,41
F(31,41) = 0.15*F(20,39)+0.33*F(20,40)+0.15*F(21,39)+0.37*F(21,40
F(31,42) = 0.09*F(19,39)+0.14*F(19,40)+0.13*F(20,39)+0.64*F(20,40
F(31,43) = 0.13*F(19,39)+0.26*F(19,40)+0.15*F(20,39)+0.46*F(20,40
F(31,44) = 0.08*F(19,39)+0.11*F(19,40)+0.13*F(19,39)+0.68*F(19,40
F(31,45) = 0.10*F(19,39)+0.40*F(19,40)+0.10*F(19,39)+0.40*F(19,40
F(32,37) = 0.13*F(20,41)+0.17*F(20,42)+0.21*F(21,41)+0.49*F(21,42
F(32,38) = 0.10*F(20,41)+0.12*F(20,42)+0.17*F(21,41)+0.61*F(21,42
F(32,39) = 0.15*F(20,41)+0.17*F(20,42)+0.25*F(21,41)+0.43*F(21,42
F(32,40) = 0.15*F(20,40)+0.33*F(20,41)+0.15*F(21,40)+0.36*F(21,41
F(32,41) = 0.12*F(19,40)+0.17*F(19,41)+0.15*F(20,40)+0.56*F(20,41
F(32,42) = 0.11*F(19,40)+0.18*F(19,41)+0.13*F(20,40)+0.59*F(20,41
F(32,43) = 0.13*F(19,40)+0.16*F(19,41)+0.20*F(19,40)+0.51*F(19,41
F(32,44) = 0.04*F(19,40)+0.06*F(19,41)+0.06*F(19,40)+0.83*F(19,41
F(32,45) = 0.11*F(19,40)+0.39*F(19,41)+0.11*F(19,40)+0.39*F(19,41
F(33,37) = 0.10*F(20,42)+0.14*F(20,43)+0.14*F(21,42)+0.62*F(21,43
F(33,38) = 0.19*F(20,42)+0.25*F(20,43)+0.22*F(21,42)+0.35*F(21,43
F(33,39) = 0.15*F(19,42)+0.15*F(19,43)+0.34*F(20,42)+0.36*F(20,43
F(33,40) = 0.12*F(19,41)+0.18*F(19,42)+0.15*F(20,41)+0.54*F(20,42
F(33,41) = 0.11*F(19,41)+0.20*F(19,42)+0.13*F(20,41)+0.55*F(20,42
F(33,42) = 0.14*F(19,41)+0.33*F(19,42)+0.15*F(20,41)+0.38*F(20,42
F(33,43) = 0.10*F(19,41)+0.13*F(19,42)+0.15*F(19,41)+0.63*F(19,42
F(33,44) = 0.03*F(19,41)+0.47*F(19,42)+0.03*F(19,41)+0.47*F(19,42
F(33,45) = 0.12*F(19,41)+0.38*F(19,42)+0.12*F(19,41)+0.38*F(19,42
F(34,37) = 0.13*F(19,43)+0.15*F(19,44)+0.27*F(20,43)+0.45*F(20,44
F(34,38) = 0.15*F(19,43)+0.15*F(19,44)+0.34*F(20,43)+0.35*F(20,44
F(34,39) = 0.13*F(19,42)+0.23*F(19,43)+0.15*F(20,42)+0.50*F(20,43
F(34,40) = 0.14*F(19,42)+0.28*F(19,43)+0.15*F(20,42)+0.44*F(20,43
F(34,41) = 0.13*F(19,42)+0.17*F(19,43)+0.19*F(19,42)+0.51*F(19,43
F(34,42) = 0.10*F(19,42)+0.13*F(19,43)+0.15*F(19,42)+0.62*F(19,43
F(34,43) = 0.04*F(19,42)+0.06*F(19,43)+0.05*F(19,42)+0.85*F(19,43
F(34,44) = 0.07*F(19,42)+0.43*F(19,43)+0.07*F(19,42)+0.43*F(19,43
F(34,45) = 0.13*F(19,42)+0.37*F(19,43)+0.13*F(19,42)+0.37*F(19,43
F(35,37) = 0.15*F(19,43)+0.34*F(19,44)+0.15*F(20,43)+0.35*F(20,44
F(35,38) = 0.13*F(19,43)+0.18*F(19,44)+0.19*F(19,43)+0.50*F(19,44
F(35,39) = 0.12*F(19,43)+0.16*F(19,44)+0.17*F(19,43)+0.55*F(19,44
F(35,40) = 0.10*F(19,43)+0.13*F(19,44)+0.14*F(19,43)+0.63*F(19,44
F(35,41) = 0.07*F(19,43)+0.09*F(19,44)+0.09*F(19,43)+0.75*F(19,44
F(35,42) = 0.04*F(19,43)+0.46*F(19,44)+0.04*F(19,43)+0.46*F(19,44
F(35,43) = 0.07*F(19,43)+0.43*F(19,44)+0.07*F(19,43)+0.43*F(19,44
F(35,44) = 0.11*F(19,43)+0.39*F(19,44)+0.11*F(19,43)+0.39*F(19,44
F(35,45) = 0.14*F(19,43)+0.36*F(19,44)+0.14*F(19,43)+0.36*F(19,44
F(36,37) = 0.25*F(19,45)+0.25*F(19,45)+0.25*F(19,45)+0.25*F(19,45
F(36,38) = 0.25*F(19,45)+0.25*F(19,45)+0.25*F(19,45)+0.25*F(19,45
F(36,39) = 0.25*F(19,45)+0.25*F(19,45)+0.25*F(19,45)+0.25*F(19,45
```

```
      F(36,40) = 0.25*F(19,45)+0.25*F(19,45)+0.25*F(19,45)+0.25*F(19,45
      F(36,41) = 0.25*F(19,45)+0.25*F(19,45)+0.25*F(19,45)+0.25*F(19,45
      F(36,42) = 0.25*F(19,45)+0.25*F(19,45)+0.25*F(19,45)+0.25*F(19,45
      F(36,43) = 0.25*F(19,45)+0.25*F(19,45)+0.25*F(19,45)+0.25*F(19,45
      F(36,44) = 0.25*F(19,45)+0.25*F(19,45)+0.25*F(19,45)+0.25*F(19,45
      F(36,45) = 0.25*F(19,45)+0.25*F(19,45)+0.25*F(19,45)+0.25*F(19,45
C
C
C     AUFFUELLEN DER RESTLICHEN KUGEL DURCH SPIEGELUNG
C
      DO 60 J = 19,36
      DO 61 JJ = 46,54
   61 F(J,JJ) = F(J,91-JJ)
      DO 62 JJ = 55,72
   62 F(J,JJ) = F(J,109-JJ)
      DO 63 JJ = 1,36
   63 F(J,JJ) = F(J,73-JJ)
   60 CONTINUE
C
      DO 65 J = 1,18
      DO 65 JJ = 1,72
   65 F(J,JJ) = F(37-J,JJ)
C
C
C     ****************************************************************
C
C     BERECHNUNG DES ABWEICHUNGSQUADRATS
C
C
      DO 69 I = 1,NE
   69  DRECH(I,1) = 1.00
C
      DO 70 I = 1,NE
      DO 70 J = 1,NW
      B = 0.0
      DO 80 JJ = 1,36
      DO 80 JJJ = 1,72
      INAL = NAL(J,JJ,JJJ)
      IF(INAL.LT.1) INAL=1
      IF(INAL.GE.90) GOTO 80
      FNF = F(JJ,JJJ)/DTD - TTD
      IF(FNF.LT.1.) FNF=1.
      NF = FNF
      IF(NF.GT.ND1) GOTO 80
      FNFN = NF
      DFN = FNF-FNFN
      NF1 = NF + 1
   79  B =B + (WO(I,NF,INAL)*(1.-DFN) + WO(I,FN1,INAL)*DFN)*COSTH(JJ)
   80 CONTINUE
   70  DRECH(I,J) = B/DRECH(I,1)
C
      B = 0.0
      DO 85 I = 1,NE
      DO 85 J = 2,NW
      IF(I.EQ.1.AND.J.NE.11)GO TO 85
      B= B+(DRECH(I,J)/DM(I,J)-1.)**2
   85 CONTINUE
      FUN =10.*SQRT(B/(NEW-NW))
C
      WRITE (6,1092) FUN
 1092 FORMAT (/,
     1 /,1X,'MITTLERE ABWEICHUNG  = ',F9.4,5X,'(GUTER FIT : FUN< 1.)',
     2 /,1X,'E(MEV) THETA  PHI   BERECHNET',7X,'MESSWERT')
C
      DO 91 I = 1,NE
      DO 91 J = 1,NW
   91 WRITE (6,1091) EO(I),TH(J),PH(J),DRECH(I,J),DM(I,J)
 1091 FORMAT (1X,3F6.2,F10.4,8X,F7.3)
      WRITE (6,1100)
 1100 FORMAT(1X,//)
C
  100 CONTINUE
```

```
C
      STOP
      END
```

# REFERENCES

## REFERENCES

/1/ P. Jung, R.L. Chaplin, H.J. Fenzl, K. Reichelt and P. Wombacher, Phys. Rev. B8, 553 (1973)

/2/ C.H. Sherman, Parke Mathematical Laboratories Report No. 2, Contract No. AF 19 (628)-2419 (1963)

/3/ A.T. Nelms, NBS-Circular 577 (26.7.1956)

/4/ G. Molière, Z. f. Naturforschung, 2a,133 (1947) and 3a, 78 (1948)

/5/ H.A. Bethe, Phys. Rev. 89, 1256 (1953)

/6/ J.W. Corbett, in F. Seitz and D. Turnbull (Ed.) "Solid State Physics Suppl. 7", New York P 30 (1966)

/7/ A.O. Hanson, L.H. Lanzl, E.M. Lyman and M.B. Scott, Phys. Rev. 84, 634 (1951)

/8/ E.J. Williams, Rev. Mod. Phys. 17, 217 (1945)

/9/ O.S. Oen, in F.L. Vook (Ed.) "Radiation Effects in Semiconductors" (1968), Proc. Santa Fee Conf. on Rad. Effects in Semiconductors, p 264 (1967)

/10/ M.E. Rose, Phys. Rev., 58, 90 (1940)

/11/ C.N. Yang, Phys. Rev., 84, 599 (1951)

/12/ B. Rossi and K. Greisen, Rev. Mod. Phys. 13, 240 (1941)

/13/ E. Rutherford, Phil. Mag., 6, 21, 669 (1911)

/14/ C.G. Darwin, Phil. Mag., 6, 25, 201 (1913)

/15/ N.F. Mott, Proc. Roy. Soc. A124, 426 (1929) and A135, 429 (1932)

/16/ W.A. McKinley and H. Feshbach, Phys. Rev. 74, 1759 (1948)

/17/ O.S. Oen, Oak Ridge Nat. Lab. ORNL-3813 (1965)

/18/ J.B. Gibson, A.N. Goland, M. Milgram and G.H. Vineyard, Phys. Rev. 120, 1229 (1960)

/19/ C. Erginsoy, G.H. Vineyard and A. Engler, Phys. Rev., 133, A595 (1964)

/20/ J.R. Beeler, JR. and M.F. Beeler, "Atomic collisions in solids", S. Datz (Ed.), Plenum Press, New York, p 105, (1975)

/21/ R.H. Silsbee, J. Appl. Phys., 28, 1246 (1957)

/22/ A. Sosin, Phys. Rev., 126, 1698 (1962)

/23/ G. Leibfried, J. Appl. Phys., 30, 1388 (1959)

/24/ R.V. Jan and A. Seeger, Phys. Status Solidi, 3, 465 (1963)

/25/ P. Vajda, Rev. Mod. Phys., 49, 481 (1977)

/26/ P. Jung, "Atomic collision in solids", S. Datz (Ed.), Plenum press, New York, p 87 (1975)

/27/ P. Jung and T. Schober, "International conference on the fundamental aspects of radiation damage in metals", Gatlinburg,Tennessee (USA) p 418 (1975)

/28/ J.R. Beeler and M.F. Beeler, "International conference on the fundamental aspects of radiation damage in metals", Gatlinburg Tennessee (USA) p 21 (1975)

/29/ A. Tenenbaum, Phil. Mag. A, 37, 731 (1978)

/30/ T.E. Mitchell, G. Das and E.A. Kenik, Phil. Mag. 32, 815 (1975)

/31/ R. Drosd, J. Nucl. Mat. 69 & 70, 804 (1978)

/32/ G. Roth, H. Wollenberger, Ch. Zeckau and K. Lücke, Rad. Effects 26, 141 (1975)

/33/ J. Lauzier, C. Minier and A. Seeger, Phil. Mag. 35, 1617 (1977)

/34/ D.E. Becker, F. Dworschak and H. Wollenberger, Rad. Effects 17, 25 (1973)

/35/ D.G. Doran and J.O. Schiffgens, Proceedings of the workshop on "Correlation of neutron and charged particle damage" Oak Ridge National Laboratory, p 3 (1976)

/36/ H.J. Dibbert, K. Sonnenberg, W. Schilling and U. Dedek, Rad. Effects, 15, 115 (1972)

/37/ K. Sonnenberg, W. Schilling, H.J. Dibbert, K. Mika and K. Schröder, Rad. Effects, 15, 129 (1972)

/38/ W. Schilling, K. Sonnenberg and J. Dibbert, Rad. Effects, 16, 57 (1972)

/39/ K. Sonnenberg, W. Schilling, K. Mika and K. Dettmann, Rad. Effects, 16, 65 (1972)

/40/ W. Schilling, G. Burger, K. Isebeck and H. Wenzl "Vacancies and interstitials in metals" North-Holland, Amsterdam p 255 (1969)

/41/ G. Antesberger, H. Schröder, K. Sonnenberg and U. Dedek" "International conference on the fundamental aspects of radiation damage in metals", Gatlinburg Tennessee (USA) P 575 (1975)

/42/ K. Reichelt, T. Schober and J. Viehweg, J. Crystal Growth 18, 312 (1973)

/43/ J. Hemmerich, KFA Jülich, Rep.-Jül-579-FN (1969)

/44/ P. Jung, KFA Jülich, Rep.-Jül-729-FF (1971)

/45/ D.E. Becker, F. Dworschak and H. Wollenberger, Phys. Stat. Sol. (b) 54, 455 (1972)

/46/ R.R. Coltman, Jr., C.E. Klabunde, J.K. Redman and A.L. Southern, Phys. Rev. Lett. 26, 131 (1971)

/47/ R.R. Coltman, Jr., C.E. Klabunde and J.K. Redman, J. Nuc. Mat. 69 & 70, 720 (1978)

/48/ J.J. Jackson, Rad. Effects 11, 201 (1971)

/49/ A. Tenenbaum, Rad. Effects 39, 119 (1978)

/50/ K. Schroeder, KFA Jülich, Rep-Jül-1083-FF (1974)

/51/ C.G. Roberts, W.P. Rickey and P.E. Shearin, J. Appl. Phys. 37, 4517 (1966)

/52/ K. Urban, Frühjahrstagung der Deutschen Physikalischen Gesellschaft, Münster 1979

/53/ R.N. Stuart, M.W. Guinan and R.J. Borg, Rad. Effects 30, 129 (1976)